AN EXPERIMENTAL STUDY OF NONLINEAR PHENOMENA IN A RESONANTLY SUSTAINED MICROWAVE PLASMA

Thesis for the Degree of Ph. D.

MICHIGAN STATE UNIVERSITY

QUONG HON LEE

1970

This is to certify that the

thesis entitled

AN EXPERIMENTAL STUDY OF NONLINEAR
PHENOMENA IN A RESONANTLY
SUSTAINED MICROWAVE PLASMA

presented by

QUONG HON LEE

has been accepted towards fulfillment
of the requirements for

Ph. D. degree in Electrical Engineering
And System Science

Major professor

Date May 20, 1970

O-169

ABSTRACT

AN EXPERIMENTAL STUDY OF NONLINEAR PHENOMENA IN A RESONANTLY SUSTAINED [illegible] PLASMA

[illegible]

The nonlinear resonance phenomena exhibited in a resonantly sustained high frequency discharge and in a mercury vapor discharge irradiated by high microwave power were experimentally studied. Two experimental systems were employed, a coaxial system and a ridge waveguide system. The transition between the linear resonances of a bounded plasma and the resonantly sustained plasma was experimentally investigated. The linear resonances were found to become distorted as the incident [illegible] was increased. Stable and unstable rf operating regions [illegible] in the resonance curve. By approximating the plasma [illegible] equivalent transmission circuit, these phenomena were [illegible] interpreted by applying transmission line theory. [illegible] for coupling microwave power into the plasma [illegible] the equivalent plasma impedance [illegible].

When the incident power [illegible] sustained plasma was above a certain [illegible]

ABSTRACT

AN EXPERIMENTAL STUDY OF NONLINEAR

PHENOMENA IN A RESONANTLY

SUSTAINED MICROWAVE PLASMA

By

Quong Hon Lee

The nonlinear resonance phenomena exhibited in a resonantly sustained high frequency discharge and a dc mercury vapor discharge irradiated by high microwave power were experimentally studied. Two experimental systems were employed; a coaxial system and a ridge waveguide system. The transition between the linear resonances of a bounded plasma and the resonantly sustained plasma was experimentally investigated. The linear resonances were found to become distorted as the incident microwave power was increased. Stable and unstable rf operating regions appeared in the resonance curve. By approximating the plasma system with an equivalent transmission circuit, these phenomena were qualitatively interpreted by applying transmission line theory. That is, criteria for coupling microwave power into the plasma was developed by plotting the equivalent plasma impedance on a Smith chart.

When the incident pump power (f_o) of a resonantly sustained plasma was above a certain threshold level, high frequency ($f_o \pm f_i$)

and low frequency (f_i) oscillations were excited in the plasma. The low frequency oscillation appears to be caused by a standing ion-acoustic wave. By reducing the incident power to just below the threshold, a separately applied cw signal was able to be amplified when the signal frequency is in the vicinity of $f_o \pm f_i$. Since amplification existed above and below f_o, the instability observed is a four frequency parametric interaction.

At the occurrence of the parametric instability, the low frequency, f_i, was observed to shift as the incident power, or the plasma size or a dc biased voltage across the discharge was varied. The sheath effects for a bounded plasma appear to account for this phenomenon.

Also, when the plasma system is resonant simultaneously at f_o, $3f_o$ and f_i, the coupling between the low frequency oscillation, f_i, and the third harmonic resonance was studied. The low frequency resonance causes the zeroth-order density profile to vary at f_i, which in turn causes the third harmonic output to be frequency modulated.

AN EXPERIMENTAL STUDY OF NONLINEAR PHENOMENA IN A RESONANTLY SUSTAINED MICROWAVE PLASMA

By

Quong Hon Lee

A THESIS

Submitted to
Michigan State University
in partial fulfillment of the requirements
for the degree of

DOCTOR OF PHILOSOPHY

Department of Electrical Engineering and Systems Science

1970

To my parents

Mr. & Mrs. S. M. Lee

ACKNOWLEDGMENTS

The author wish to express his deep gratitude to his major professor, Dr. J. Asmussen, for providing continuous guidance and encouragement throughout the course of this research. Sincere appreciation is also due to the other members of the guidance committee, Dr. K. M. Chen, Dr. B. Ho, Dr. N. Hills and Dr. H. Hedges for their time and interests in this work; and to P. Colestock for providing the experimental curve shown in figure 4.6. Finally, it is gratefully acknowledged that this research was supported in part by the National Science Foundation under grant GK-2952.

TABLE OF CONTENTS

LIST OF FIGURES

Figure		Page
3.6	Graphical solution of the high frequency capacitor impedance for different sheath thickness, s, ($L = 1.6$ mm, $\omega/U_e = 2 \times 10^4$, $s = .2$ mm and .6 mm).	50
3.7	Graphical solution of the high frequency capacitor impedance for different electron temperature, T_e, ($L = 1.6$ mm, $s = .6$ mm, $\omega/U_e = 2 \times 10^4$ and $e \times 10^4$)	51
3.8	Normalized amplitude of the low frequency electric fields, $\lvert LE_o/V \rvert$ and $\lvert LE_p/V \rvert$, vs. ω_{p+}/ω ($L = 1.6$ mm, $s = .6$ mm, $\omega/U_e = 25$, $x = 0$, $\nu_-/\omega = .1$, $\nu_+/\omega = .001$).	57
3.9	Real part of the normalized low frequency plasma field, LE_p/V, vs. position, x, at resonance ($L = 1.6$ mm, $s = .6$ mm, $\omega/U_e = 25$, $\nu_-/\omega = .1$, $\nu_+/\omega = .001$)	60
3.10	Graphical solution of low frequency capacitor impedance ($L = 1.6$ mm, $s = .6$ mm, $\omega/U_e = 25$)	65
4.1	Experimental system: (a) overall view of the coaxial system; (b) close view of the coaxial discharge structure	67
4.2	Experimental apparatus block diagram for the coaxial system.	69
4.3	Cross section of the coaxial discharge structure	72
4.4	Voltage standing wave pattern for breakdown by high E field	74

Figure | Page

Figure		Page

CHAPTER 1
INTRODUCTION

In this thesis, emphasis is placed on the nonlinear resonance effects of a resonance-sustained high frequency discharge or "plasmoid" in the absence of a static magnetic field. This resonantly sustained discharge exhibits unusual phenomena at low pressure. The discharge has been observed to concentrate in sharply defined stable, luminous balls, spindles and pear-shaped bodies floating in a surrounding dark sheath. Moreover, only a comparatively low voltage is needed to sustain this luminous discharge. Ever since its first observation by Wood[1] in approximately 1930, many experimental and theoretical works have been devoted to studying its physical behavior.

The discharge that has been studied is generated and maintained by microwave power. The gas, usually dry air, is ionized by a high frequency electric field of 3.03 GHz at a pressure of about one to five torr. Breakdown occurs when electron-neutral collision frequency is approximately equal to the driving frequency.

Once the plasma is created, the pressure in the system is reduced to a very small value in the order of 400 microns or less.

In order to maintain such a plasma at low pressure, the plasma adjusts itself to a resonance state.

In such a low pressure region, the ions are lost to the wall not by an ordinary diffusion process involving collisions with the neutral particles, but by a direct fall to the wall. That is, the mean-free-path of the elastic ion-neutral collision is larger than the dimension of the confining vessel.

In order to provide background for explanations developed in later chapters, a review of pertinent literature is made in Chapter 2. The problem of the coupling between electroacoustic and electromagnetic waves is briefly discussed. The theory of linear electroacoustic resonances is presented and relevant literature on nonlinear plasma phenomenon is reviewed.

The linear theory of the plasma capacitor is presented in Chapter 3. The theoretical results of this model can easily be applied to the experimental results presented in later chapters. Both high microwave frequency and low (MHz) frequency effects are studied. At high frequency, the cold, uniform plasma predicts only one resonance at a frequency ω_r less than the plasma frequency ω_p. However, if one assumes a warm plasma, a series of secondary resonances, corresponding to standing electron acoustic waves, occur for $\omega_r > \omega_p$. In the low frequency regime, the model again indicates the presence of standing longitudinal waves; namely, the presence of ion-acoustic wave. A transmission equivalent circuit for both high and low frequencies is developed. The effects of the plasma sheath are clearly indicated in this model and plots of the E field for cold plasma, temperature and ion-acoustic resonances are made.

The nonlinear resonance effects arising from nonlinear microwave-plasma interactions are experimentally studied with a ridge waveguide system and with a coaxial type of microwave-vacuum system. Both of these structures can be approximated as a plasma-filled capacitor. A detailed description of the experimental apparatus is given in Chapter 4.

Experimental results are presented in Chapter 5. The transition between the linear resonance of a plasma column and a completely resonantly sustained plasma is presented. A qualitative description of this transition is developed using a Smith Chart representation of the plasma capacitor impedance. Stable and unstable regions are clearly indicated.

A plasma instability in a resonantly sutained plasma is also investigated. Experimental results indicate that a four frequency parametric interaction is responsible for the instability. It is believed that a nonlinear coupling between microwave frequency resonances and low frequency ion resonances is involved. In fact, the plasma capacitor theory for the ion-acoustic wave with the proper sheath, electron temperature, etc., is able to explain certain experimentally observed low frequency variations.

Nonlinear coupling between low frequency and high frequency resonances is also studied. Experimental and theoretical results indicate that low frequency oscillations (due to standing ion-acoustic waves) cause the zeroth-order density profile to oscillate at the low frequency. This variation of the density profile causes the third-harmonic resonance to vary resulting a frequency modulated third harmonic output.

Experimental results describing the operation of a completely resonantly sustained plasma are also presented.

Chapter 6 summarizes the work presented in this thesis. Also, certain problem areas which need additional attention in future research are pointed out.

CHAPTER 2

GENERAL REVIEW OF MICROWAVE-PLASMA INTERACTION

This chapter is devoted to the general review of literature pertaining to the nonlinear resonance effects in a resonantly sustained high-frequency discharge. The physical interpretation of these non-linear resonance phenomena can be perceived through the study of the coupling between electromagnetic and electroacoustic waves and the nature of linear resonances in a bounded plasma.

As a start, the coupling of electromagnetic and electroacoustic waves in an infinite, non-uniform plasma is demonstrated by deriving a fourth-order differential equation for plasma potential. Then, the experimental and theoretical interpretation of the linear Tonks-Dattner resonances exhibited in plasma scattering and plasma capacitor are reviewed. Finally, the physical mechanism of a resonantly sustained discharge is described. Nonlinear resonance effects which bear direct relationship to the experimental investigation here are emphasized.

2.1 Coupling of electromagnetic and electroacoustic waves

A warm plasma can support propagation of transverse electromagnetic (EM) and longitudinal electroacoustic (EA) waves if the signal frequency ω is greater than the plasma frequency ω_p. These EM and EA waves are uncoupled in an isotropic, homogeneous plasma of infinite extent. Field[6] formulated the coupling problem quantitatively for an infinite plasma on the basis of a hydrodynamic model of the plasma. He concluded that coupling exists under any one of these three conditions: (1) plasma inhomogeneities, (2) static magnetic field and (3) density discontinuity, such as that at a vacuum-plasma boundary (really this is a special case of (1)). Since the investigation to be reported involves no static magnetic field, only the coupling introduced by a non-uniform plasma will be considered below. The basic equations used are the first two linearized, hydrodynamic equations and the Maxwell's equations.

In this analysis, the heavy ion and neutral molecule distributions are assumed unperturbed. A linearized theory for small perturbation of electrons is followed in deriving the coupling equations. The plasma variable $\vec{E}$, n and p are written as the sum of a dc term (subscript zero) with no time variation and a perturbation term (subscript 1) with a time dependence of $e^{j\omega t}$, while $\vec{H}$ and $\vec{v}$ are perturbed quantities.

If the perturbation of the waves causes adiabatic changes in the plasma, the steady state and perturbed pressures are directly proportional to their corresponding densities

$$p_{eo} = KTn_{eo}(r)$$

$$p_{e1} = \gamma KTn_{e1}$$

where γ is a constant depending on the number of degrees of freedom of compression involved. Since the plasma density varies with position, $n_{eo}(r)$ (denoted by n_{eo} from here on) is a function of $\vec{r}$. From the linearized hydrodynamic equations, two first-order and one zeroth-order equations are obtained.[7] The zeroth-order equation is of the form

$$\vec{E}_o = -\frac{mU_e^2}{\gamma e}\frac{\nabla n_{eo}}{n_{eo}} \tag{2.1}$$

The first-order equations are

$$j\omega n_{e1} = -\nabla\cdot(n_{eo}\vec{v}_{e1}) \tag{2.2}$$

$$j\omega\vec{v}_{e1} = \frac{-en_{eo}}{m_e n_{e1}}\vec{E}_o - \frac{e}{m_e}\vec{E}_1 - \frac{U_e^2}{n_{eo}}\nabla n_{e1} \tag{2.3}$$

where

$$U_e^2 = \frac{\gamma KT_e}{m_e}$$

Equation (2.1) shows that the static electric field, $\vec{E}_o$, created by the gradient of the steady state density, n_{eo}, is in the direction opposite to the maximum change of density.

From the Maxwell's equations, the following first-order equations are obtained

$$\nabla \cdot \vec{E}_1 = \frac{-e}{\epsilon_o} n_{e1} \qquad (2.4)$$

$$\nabla \times H_1 = j\omega \epsilon_o E_1 - n_{eo} e \vec{v}_{e1} \qquad (2.5)$$

$$\nabla \times \nabla \times \vec{E}_1 = -j\omega\mu_o \nabla \times \vec{H}_1 \qquad (2.6)$$

Equations (2.1) to (2.6) can be combined to yield

$$\nabla \times \nabla \times \vec{E}_1 + \frac{U_e^2}{\gamma c^2} \frac{\nabla n_{eo}}{n_{eo}} (\nabla \cdot \vec{E}_1) - k_e^2 \vec{E}_1 - \frac{U_e^2}{c^2} \nabla(\nabla \cdot \vec{E}_1) = 0 \qquad (2.7)$$

where

$$k_e^2 = \frac{\omega^2}{c^2} \left(1 - \frac{\omega_{p-}^2(r)}{\omega^2} \right)$$

$$c^2 = \frac{1}{\mu_o \epsilon_o}$$

$$\omega_{p-}^2(r) = \frac{n_{eo} e^2}{m_e \epsilon_o}$$

According to the vector theory[8], a vector can be decomposed into the sum of an irrotational part and a solenoidal part. The former has a vanishing curl, while the latter has a zero divergence

$$\vec{E}_1 = \vec{E}_s + \vec{E}_{irr}$$

where $\nabla \cdot \vec{E}_s = 0$

$$\nabla \times \vec{E}_{irr} = 0$$

In terms of $\vec{E}_s$ and $\vec{E}_{irr}$, equation (2.7) can be written as

$$(\nabla \times k_e^2) \vec{E}_s + \left(\frac{U_e^2}{c^2} \nabla^2 + k_e^2 - \frac{U_e^2}{c^2} \frac{\nabla n_{eo}}{\gamma n_{eo}} \nabla \cdot \right) \vec{E}_{irr} = 0 \qquad (2.8)$$

It is convenient to define the electron density, n_{eo}, as the maximum magnitude, N_o, times a dimensionless spatial varying function, $f(r)$, which describes the inhomogeneities in the plasma; i.e., $n_{eo} = N_o f(r)$. Then, the curl of equation (2.8) can be written as

$$(\nabla^2 + k_e^2)\nabla \times \vec{E}_s - \frac{\omega_{p-}^2}{c^2} \nabla f \times (\vec{E}_s + \vec{E}_{irr}) - \frac{U_e^2}{\gamma c^2} \left(\nabla \times \frac{\nabla f}{f} - \frac{\nabla f}{f} \times \nabla\right)(\nabla \cdot \vec{E}_{irr}) = 0 \tag{2.9}$$

where $\omega_{p-}^2(r) = \omega_{p-}^2 f(r)$

$$\omega_{p-}^2 = \frac{N_o e^2}{m_e \epsilon_o}$$

$$f = f(r)$$

Similarly, the divergence of equation (2.8) becomes

$$\left[\frac{U_e^2}{c^2}\left(\nabla^2 - \frac{1}{\gamma}\nabla \cdot \frac{\nabla f}{f} - \frac{1}{\gamma}\frac{\nabla f}{f} \cdot \nabla\right) + k_e^2\right](\nabla \cdot \vec{E}_{irr}) - \frac{\omega_{p-}^2}{c^2}\nabla f \cdot \vec{E}_{irr}$$

$$= \frac{\omega_{p-}^2}{c^2}\nabla f \cdot \vec{E}_s \tag{2.10}$$

If the effects due to the static electric fields are excluded equations (2.9) - (2.10) are the coupled equations derived by Field. The fields $\vec{E}_{irr}$ and $\vec{E}_s$ are coupled through $\nabla f(r)$; i.e., the non-vanishing plasma non-uniformity. Thus, no coupling exists in a homogeneous plasma where f is unity. Furthermore, equation (2.10) shows that $\vec{E}_s$ must have a component in the direction of $\nabla f(r)$ in order for coupling to take place. This is important to consider when experimentally exciting EA waves by EM waves.

In consideration of only plane wave propagation in an infinite plasma, the operator ∇ can be replaced by $j\vec{k}$. The zero divergence of the solenoidal part implies that $\vec{E}_s$ corresponds to the transverse electromagnetic part of the field, while the vanishing curl implies that $\vec{E}_{irr}$ corresponds to the longitudinal electroacoustic part of the field.

Since $\nabla \times E_{irr} = 0$, the electroacoustic part of the field, $\vec{E}_{irr}$, can be expressed in terms of the scalar, plasma potential ϕ_p; i.e.,

$$\vec{E}_{irr} = - \nabla\phi_p \tag{2.11}$$

Similarly, the electromagnetic part of the field, $\vec{E}_s$, is related to the vector potential, $\vec{A}$, and the scalar electric potential, ϕ_e, through

$$\vec{E}_s = -j\omega\mu_o A - \nabla\phi_e \tag{2.12}$$

$$\vec{H}_1 = \nabla \times \vec{A} \tag{2.13}$$

The electric field in the plasma then has the form

$$\vec{E}_1 = j\omega\mu_o\vec{A} - \nabla\phi_e - \nabla\phi_p \tag{2.14}$$

From the zero divergence of $\vec{E}_s$, the vector potential $\vec{A}$ can be directly related to the electric potential ϕ_e

$$\nabla \cdot \vec{A} = \frac{-\nabla^2\phi_e}{j\omega\mu_o} \tag{2.15}$$

Also, equation (2.3) to (2.5) can be combined to yield a single coupled equation of potentials.

$$\nabla^2\vec{A} + k_e^2\vec{A} = \frac{j}{\omega\mu_o}\left[\frac{\omega_{p-}^2}{c^2}\phi_e\nabla f + \frac{U_e^2}{\gamma c^2}(\nabla\cdot\frac{\nabla f}{f})\nabla^2\phi_p + k_e^2\nabla\phi_p\right] \qquad (2.16)$$

Equation (2.16) is obtained under the assumption of the Lorentz condition which relates the vector potential $\vec{A}$ to the electric potential ϕ_e

$$\nabla\cdot\vec{A} = \frac{k_e^2}{j\omega\mu_o}\phi_e \qquad (2.17)$$

The divergence of equation (2.16) is identical to equation (2.10) when expressed in potential form; that is

$$\nabla^2\nabla\phi_p + \frac{1}{\gamma}\left[\frac{1}{\lambda_D^2}\left(\frac{\omega^2}{\omega_{p-}^2} - f\right) - \nabla\cdot\frac{\nabla f}{f} - \frac{\nabla f}{f}\cdot\nabla\right]\nabla^2\phi_p - \frac{1}{\gamma\lambda_D^2}\nabla f\cdot\nabla\phi_p$$

$$= \frac{-1}{\gamma\lambda^2}\nabla f\cdot(j\omega\mu_o A + \nabla\phi_e) \qquad (2.18)$$

where

$$\lambda_D^2 = \frac{KT}{m\omega_{p-}^2} \text{ is the Debye's wavelength}$$

Obviously, the electromagnetic potentials, $\vec{A}$ and ϕ_e, are coupled to the plasma potential, ϕ_p, through inhomogeneities in the plasma. By applying the quasi-static approximation to the last equation, one arrives at the very well known equation for the Tonks-Dattner resonances in a bounded plasma[17] (the coupling of the electromagnetic part of the field is also included; i.e., $E = -\nabla\phi_p - \nabla\phi_e$)

$$\nabla^2\nabla^2\phi_p - \frac{1}{\gamma}\left[(\frac{\nabla f}{f}\cdot\nabla)\nabla^2\phi_p + \frac{1}{\gamma}\;\frac{1}{\lambda_D^2}(\frac{\omega^2}{\omega_{p-}^2} - f) - \nabla\cdot\frac{\nabla f}{f}\right]\nabla^2\phi_p - \frac{1}{r\lambda_D^2}$$

$$\nabla f\cdot\nabla\phi_p = \frac{-1}{\gamma\lambda_D^2}\,\nabla f\cdot\nabla\phi_e \qquad (2.19)$$

2.2 Resonances in bounded plasmas

As early as 1931, Tonks[9] observed the phenomenon of resonance oscillation in a bounded uniform plasma at a frequency ω less than the plasma frequency ω_p. His observation was explained with an equivalent permittivity, $\epsilon = \epsilon_o\,(1 - \frac{\omega_p^2}{\omega^2})$, in a uniform, external field. This is now called the cold plasma approximation. About twenty years later, when performing some microwave scattering experiments, Romell[10] observed the main resonance of Tonks and an additional series of weaker resonances. These weaker resonance were not predicted with the uniform, cold plasma model of Tonks. Through extensive experimental investigations, Dattner[11] concluded that the observed resonances are dipolar in nature arising from oscillations of separated charges. These additional dipolar resonances have often been referred to as "Tonks-Dattner" or "T-D" resonances. Attempts were first made to explain these multiple resonances with a non-uniform, cold plasma.

Treating the plasma as a dielectric cylinder with an abrupt change in density at the edge, Herlofson[12] found that the resonance was damped by the density gradient. Apprximating a non-uniform plasma cylinder with a discrete number of uniform, cylindrical dielectric shells, Kaiser and Closs[13] showed that there exists a new resonance for each discontinuity in density. Although a continuous spectrum of resonances were able to be obtained from such a non-uniform dielectric model, the theoretical predictions failed to compare satisfactorily with experimental results.

Including the thermal motion of electron in a uniform plasma, Gould[14] observed a main resonance similar to that predicted by the cold plasma approximation and a spectrum of temperature resonances at higher frequencies, ω_N, which clustered near the plasma frequency, i.e.,

$$\omega_N^2 = \omega_{p-}^2 (1 - 3\lambda_D^2 k_N^2) \qquad N = 1, 2, 3, \ldots$$

where k_N is an eigenvalue of the bounded plasma problem. These temperature resonances were derived from a hydrodynamic description of the electron motions under adiabatic changes in a collisionless plasma similar to the one discussed in 2.1. The distribution of the temperature resonance was, however, too closely spaced to account for the correct experimental results. Better quantitative agreement with the experiments was possible when a non-uniform warm plasma was considered.

Physically, as the electron plasma waves propagate up the density gradient, the wave becomes cut-off, and is reflected when it reaches a point where the applied frequency, ω, equals the local plasma frequency ω_{p-}. Consequently, only evanescent waves exist in the high density plasma core at a radius r_c where $\omega_{p-}(r_c) = \omega$, while standing longitudinal electron plasma waves of the type described by Bohm and Gross[15] are trapped in the low density region bounded by the plasma core and the glass wall. In this model, both the electron temperature and the electron density profile contribute to the resonance conditions. Using a perturbed tensorial pressure and a parabolic electron density profile, Vandenplas and Gould[16] obtained a sixth-order linear differential equation for a non-uniform, warm plasma cylinder. However, the solution proved to be too difficult to obtain.

In 1964, Parker, Nickel and Gould[17] simplified the problem by postulating a scalar perturbed pressure, $p_{el} = \gamma K T n_{el}$. They obtained a fourth-order linear differential equation for plasma potential on the basis of linearized analysis for a small perturbation of electrons similar to that outlined in 2.1. The differential equation they derived for the longitudinal electron plasma wave is similar to equation (2.19) that is

$$\nabla^2\nabla^2\phi_p - \frac{1}{\gamma}\left(\frac{\nabla f}{f}\cdot\nabla\right)\nabla^2\phi_p + \frac{1}{\gamma}\left[\frac{1}{\lambda_D^2}\left(\frac{\omega^2}{\omega_{p-}^2} - f\right) - \nabla\frac{\nabla f}{f}\right]\nabla^2\phi_p - \frac{1}{\gamma\lambda_p^2}$$

$$\nabla f\cdot\nabla\phi_p = 0$$

Numerical solutions, through numerical integration of the above equation, were obtained with a density profile corresponding to the Tonks-Langmuir[18] model. The calculated resonances showed excellent quantitative agreement with experiments for the main and the first two temperature resonances. In this theory the electron temperature, T_e had to be chosen for the best fit to the experimental data.[17] Recently, while experimenting with rare gases, Hart and Oleson[19] observed that the temperature resonances are fewer and broader than those for a mercury vapor discharge.

Gould's hydrodynamic model of a collisionless plasma did not include Landau damping which occurs in the low density region near the tube wall. Furthermore, the use of the boundary condition that the electron velocity vanishes at the wall was without good theoretical justification. Recently, W. M. Leavens[20] and D. E. Baldwin have developed a kinetic model for the temperature resonances. In both cases the Landau damping that is present near the tube wall is included in the analysis. Experimental confirmation of these theories has been made without choosing the electron temperature for the "best fit."

The resonance phenomena exhibited in microwave scattering from a plasma column appear also in the circuit characteristics of a plasma-filled capacitor system shown in Figure 2-1. The hydrodynamic theory for the resonance behavior of a one-dimensional plasma slab-condenser system was examined theoretically by Vandenplas and Gould.[22] The plasma resonator which consists of two infinite parallel plates separated by a distance L is excited by an externally applied rf voltage source V(t). A uniform plasma slab of thickness L-s is placed symmetrically within the plates between

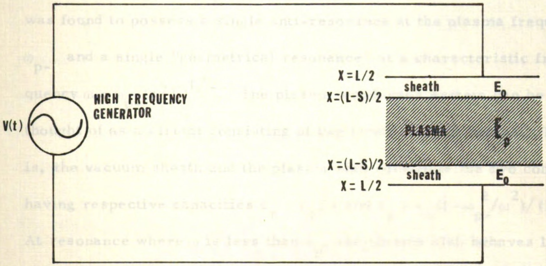

Figure 2.1 Parallel-plate plasma capacitor

two vacuum sheaths of total thickness s. In the analysis, the capcitor impedance was determined by applying a quasi-static approximation and the following boundary conditions (1) the continuity of total current, (2) the perfect relfection of electrons (i.e., $\vec{v}_e = 0$) at the plasma-vacuum boundary, and (3) the voltage across the plates $V(t) = \int Edx$. For the case of cold plasma (T=0), the plasma condenser system was found to possess a single anti-resonance at the plasma frequency ω_{p-}, and a single "geometrical resonance" at a characteristic frequency $\omega = \omega_{p-}(s/L)^{1/2}$. The plasma-condenser system can be thought of as a circuit consisting of two condensers in series. That is, the vacuum sheath and the plasma slab constitute the two condensers having respective capacities $c_r = \epsilon_o/s$ and $c_p = \epsilon_o(1-\omega_{p-}^2/\omega^2)/(L-s)$. At resonance where ω is less than ω_p, the plasma slab behaves like an inductive medium since $[1 - (\omega_{p-}^2/\omega)] < 0$. Thus, the resonance can be interpreted as a series resonance between the capacitance of the sheath region and the inductance of the over dense plasma.

In the warm plasma case ($T_e \neq 0$), the main resonance was found to occur at $\omega \sim \omega_{p-}(s/L)^{1/2}$ for $\lambda_D << s$. In addition, a discrete temperature resonance spectrum appears at higher frequency $\omega_N > \omega_{p-}$ where

$$\omega_N^2 = \omega_{p-}^2[1 + (2N+1)^2 \gamma \pi^2 \lambda_D^2/s^2] \quad N = 1, 2, 3, \ldots$$

The temporal effect also introduced a discrete anti-resonance spectrum adjacent to ω_N. The collisions in the plasma were found to have relatively small influence on the main resonance, but significant damping on the temperature resonances. For the case considered by Vandenplas, the temperature resonances were completely obscured by the collisional damping for $\nu_e/\omega = .1$. An experimental investigation by Messian and Vandenplas[23] showed that the main anti-resonance and the main resonance agree remarkably well with theory.

In addition to providing a physical insight into the nature of resonances in a bounded plasma, this simple plasma capacitor system may also predict the physical behavior of a resonantly sustained high-frequency plasma. An equivalent circuit of this warm plasma will be developed and discussed in Chapter 3.

2.3 Resonantly sustained high frequency discharge

The peculiar phenomena exhibited by a resonantly sustained high frequency discharge or high frequency "plasmoid" was first described by Wood[1] in approximately 1930. The rf discharge was created in glass vacuum vessels by applying an electric field of 10 to 100 MHz to some external metal electrodes. Wood observed that the discharge was concentrated in sharply defined, stable, luminous balls, spindles and pear-shaped bodies. That is, instead of appearing as a diffuse glow completely filling the tube, the plasma appeared to "float" and was surrounded entirely by a dark sheath region. Also, the discharge could be sustained with a low exciting voltage. Wood suggested that some electron oscillation similar to those described by Tonks and Langmuir[24] could be sustained with a low exciting voltage. Wood suggested that some electron oscillation similar to those described by Tonks and Langmuir[24] could explain this phenomenon.

There was no further progress on the resonantly sustained plasma until 1942. At that time, theoretical studies of the high frequency discharge by W. O. Shumann[25]; and Allis, Brown and Everhard[26] showed that when a high frequency field is applied to a discharge, the field tends to concentrate in the resonance region of the discharge where the ionization rate is maximum. Years later (1958-61), E. R. Harrison[27] and A. J. Hatch[28, 29] independently performed extensive experimental studies with rf discharges. They obtained conclusive evidence which supported Wood's hypothesis of an oscillatory phenomenon in the plasmoid.

From probe measurements of rf potential in high frequency plasmas at low pressures, Hatch[29] observed that the rf field in the plasma is 180° out of phase with respect to the sheath field. This is contrary to what occurs in a diffusion controlled plasma. The phase reversal indicates the existence of electron oscillation in the plasmoid. Also, the dark sheath around the plasmoid can be associated with the points of zero high frequency fields where phase reversals occur.

In spite of all these experimental and theoretical efforts, no good physical explanation of the plasmoid phenomenon had been found until a few years ago ($\sim$ 1963). At that time, J. Taillet[30] combined experimental observation of the electric field in the plasma and the role of the negative ions together with a straightforward application of the linear theory of bounded plasma resonance to produce a qualitative explanation of the plasmoid phenomenon.

Taillet's physical interpretation of the resonantly sustained radio frequency discharge was based on the linear theory of Vandenplas and Gould[22] for a plasma-filled capacitor shown in Figure 2.1 and the balance of rf power in the plasma. To explain the resonances in the rf discharge, he formulated the plasma capacitor problem by calculating the rf electric fields in the vacuum sheath as well as in the uniform plasma slab. The electric fields of this cold, collisionless model predict Hatch's observation of a phase reversal and oscillation phenomena in a rf plasmoid. Taillet also verified these theoretical results experimentally with a slab discharge which was excited by applying a rf electric field of 15-50 MHz between two parallel and horizontal metallic discs. The rf electric field in the discharge was estimated from the vertical deviations of sharply focused electron beams which traverse the discharge horizontally in the absence of a field.

Physically, a resonantly sustained rf discharge differs from the well-known diffusion-controlled plasma in many respects. A resonantly sustained rf discharge is a discharge which is always in a resonant state. It occurs in a pressure regime lower than that of a diffusion plasma. Furthermore, it is characterized by a low rf sustaining voltage. Due to the nature of resonance in the plasma, the rf field inside the plasma is 180° out of phase with respect to the sheath field. Also, this resonance effect allows the E field inside the plasma and the sheath to be much greater than the field when there is no plasma present.

In a resonantly sustained rf plasma, the ions are lost to the wall not by an ordinary diffusion process involving collisions against the neutral particles, but by direct fall. That is, in such a low pressure regime, the mean-free-path of the elastic ion-neutral collision is larger than the dimension of the confining vessel.

The electron plasma frequency of a resonantly sustained discharge is of the order of magnitude or greater than the driving frequency. Whenever the generator frequency or the pressure is varied, the plasma reacts to such a change by adjusting its parameter (i.e., electron density, sheath thickness, etc.), so that an eigenfrequency of the bounded plasma system remains approximately equal to the generator frequency or a harmonic of the generator frequency.

A typical resonance-sustained high frequency discharge is pictured in Figure 2.1. Note that the plasma is completely surrounded by sheaths, and thus makes no contact with the capacitor plates. The plasma is created and maintained at low pressure by a high frequency power.

Although much progress has been made toward a better understanding of the radio frequency plasmoid, but the physical process of the nonlinear phenomena associated with such a plasma is still poorly known. This is particular true in a microwave (GHz) discharge since most experiments in the past were performed in the MHz frequency range. In this investigation, the nonlinear phenomena of a resonantly sustained plasma were studied at frequencies of 3.03 and 9.09 GHz.

2.4 Nonlinear effects in a resonantly sustained high frequency plasma

In the forgoing discussion of resonance behavior in plasma, only linear effects have been considered, and a linearized theory has been adopted to explain experimental results. However, as the incident microwave power increased, nonlinear effects become important and the plasma will finally become resonantly sustained by the microwave power. These nonlinear properties have been the subject of experimental and theoretical research for a number of years. In the following, the research on harmonic and sub-harminic generation, parametric interaction and the nonlinear behavior of temperature resonances at high power is briefly reviewed.

The harmonic generation in a plasma has been investigated by numerous researchers in the past. Recently, Asmussen and Beyer[33] extended this investigation, both experimentally and theoretically, in a coaxial discharge structure. Their experimental results showed that maximum third harmonic power was generated when the plasma is resonant at the third harmonic as well as the fundamental frequency. Their results were qualitatively interpreted with a nonlinear plasma-filled capacitor. In this kind of harmonic generation, the dominant nonlinear microwave source of harmonic power comes from the spatial and time varying electromagnetic field as well as inhomogeneities in a bounded plasma.[34]

In a recent experimental investigation employing a cylindrical ionized column of mercury, vapor inserted across a waveguide, enhanced radiation at 1/3 the applied signal was observed by Demokan, Hsuan and Lonngren.[35] The proper resonance condition was for the bounded plasma to be resonant at the fundamental and the subharmonic frequency. The strong coupling between the incident microwave signal and the fundamental longitudinal plasma wave at resonance generates a longitudinal field of large amplitude which acts as a driving term for the sub-harmonic.

The resonance phenomena exhibited in microwave scattering by a plasma column are linear at low power. However, as the incident microwave power is increased Hsuan, Ajmera and Longren[2] observed that the temperature resonances exhibit a strong nonlinear behavior. They interpreted these nonlinear resonance effects at high power as due to the alteration of the zeroth-order density distribution of a plasma with an external electromagnetic field. On the basis of this assumption, they derived a nonlinear differential equation that includes the spatial inhomogeneity and temperature effect of the macroscoptic electric field. The solution predicts the following nonlinear phenomena: a hysteresis behavior of the resonance, a shift in the resonance frequency and an abrupt jump in the magnitude of the reflected and transmitted signal. These nonlinear resonance effects were believed to result from one of the three physical mechanisms: (1) heating, (2) ionization and (3) spatial inhomogeneith of the electric field. Similar nonlinear resonance effects were noted by Hsuan, who formulated the problem of interaction between a plasma and radiation in a self-consistent manner. Concurrently, Massiaen and Vandenplas[4] investigated the nonlinear resonance effects at high power with a plasma tube-waveguide system. A photo-electric device was installed to measure the plasma luminosity, and hence the average plasma density. In addition to the observation of hysteresis and deformation of resonance peaks, the plasma was seen to show preferential absorption of high-frequency power at resonance and a tendency to remain in a resonance state. In Chapter 5 this is discussed further. For sufficiently high incident microwave power, the plasma can be self-sustained by the high-frequency energy in a discrete set of resonance states. These resonances correspond to the linear temperature and cold plasma resonances at lower power. Then the plasma is resonance-sustained, the absorbed power and the corresponding plasma density varies only slightly with incident power.

The parametric excitation of the modes of an infinite plasma has been studied theoretically by several investigators[36-39]. Experimentally, the parametric coupling between electron plasma and ion-acoustic oscillations was investigated by Stern and Tzoar[40]. In the experiment, a microwave signal of frequency ω_o was incident transversely on a cylindrical dc plasma column. The signal frequency is approximately equal to a temperature or cold plasma resonance of the column. When the incident "pump" power was increased above a certain power threshold, radiation at two additional frequencies, $\omega_o \pm \omega_i$, was observed. This observation was interpreted as being produced by a four-frequency parametric interaction. That is, an interaction of a low frequency resonance at ω_i with high frequency resonances at $\omega_o \pm \omega_i$ and ω_o. Above the threhold, the frequency, ω_i, compares closely to the value of the ion-acoustic oscillation which had a wavelength of the same order of magnitude as the inside diameter of the tube. The excitation of the ion oscillation at ω_i was detected above the threshold by probe measurements. According to their experimental results, the pump field "threshold" is considerably lower than that predicted by DuBois and Goldman[41], who formulated the problem on the basis of a Green's function perturbation analysis for an infinite plasma. DuBois and Goldman suggested that the unresolved discrepancy might be expected to result from an effect other than the pure parametric excitation in a plasma. Namely, they postulated that the low frequency f_i was excited by another type of instability (such as two stream instability) and the high frequency spectrum resulted from a simple frequency mixing.

In an attempt to explain the discrepancy between the theoretical and experimental threshold condition, Amano and Okamoto[42] pointed out that the density gradient of a plasma, which always exists in laboratory experimental condition, may reduce the power threshold somewhat for the experimental conditions of Stern and Tzoar. Taking higher-order mode coupling into account, R. Goldman[43] suggested that a full treatment of the experimental phenomena would require an analysis of the neturals, fluctuation effects, heating effects and finite geometry effects. To this date, the theoretical interpretation of this experiment is unresolved.

In Chapter 5, experimental results for a similar radiation induced instability in a resonantly sustained plasma are presented. It is shown experimentally that the instability is caused by a four frequency parametric interaction.

CHAPTER 3

THE PLASMA CAPACITOR SYSTEM

3.1 Theory

In this chapter, a unified formulation is made for the resonance behavior of a warm plasma capacitor which approximates the experimental system used here. Such an analysis will provide physical insight into the experimental results to be presented later.

As shown in Figure 2.1, the one-dimensional plasma capacitor consists of two infinite parallel, metallic plates separated by a distance L. The separation of the plates is much smaller than the electromagnetic wavelength. Thus, one can apply the quasi-static approximation. A slab of uniform, warm plasma is located symmetrically around the $x = 0$ axis between two vacuum sheaths of thickness $s/2$ between the plasma and the plate. The plasma capacitor system is excited externally with a rf voltage $V(t)$.

The formulation of the resonance problem is based on the small signal perturbation of a hydrodynamic plasma. The fundamental equations used are Maxwell's equations and the linearized hydrodynamic equations for an interpenetrating electron gas and ion gas. For time-harmonic variation, these equations are

$$j\omega m_e \vec{v}_{el} = -eE - \frac{KT_e}{N_o} \nabla n_{el} - \nu_e m_e \vec{v}_{el} \tag{3.1}$$

$$j\omega m_i \vec{v}_{il} = eE - \frac{KT_i}{N_o} \nabla n_{il} - \nu_i m_i \vec{v}_{il} \tag{3.2}$$

$$N_o \nabla \cdot \vec{v}_{el} + j\omega n_{el} = 0 \tag{3.3}$$

$$N_o \nabla \cdot \vec{v}_{il} + j\omega n_{il} = 0 \tag{3.4}$$

$$\nabla \cdot \vec{E} = \frac{e}{\epsilon_o} (n_{il} - n_{el}) \tag{3.5}$$

$$\nabla \times \vec{E} = -j\omega\mu_o \vec{H} \tag{3.6}$$

$$\nabla \times \vec{H} = N_o e(\vec{v}_{il} - \vec{v}_{el}) + j\omega\epsilon_o \vec{E} \tag{3.7}$$

where the subscript, e, denotes electron and, i, ion; n and v are the perturbed macroscopic particle density and velocity.

Since hydrodynamic equations are used, Landau damping is not included. Consequently, the result becomes erroneous in a certain low density region. Also, by assuming a uniform plasma, the steady state plasma density thus does not vary with position. Such an assumption introduce inaccuracy to the resonant frequency. Since the intention of this analysis is to study the general nature of resonance in a bounded plasma, and not to produce exact theoretical verification of experimental results, the non-uniformity of the plasma is neglected. However, it is understood that the exact resonance positions of a non-uniform plasma differ from the results obtained here.

Maxwell's equations are used to derive the differential equation for the electric field in a plasma medium. From equation (3.6) and (3.7), it can be shown that

$$\nabla \times \nabla \times \vec{E} - \omega^2 \mu_o \epsilon_o \vec{E} = -j\omega\mu_o N_o e(\vec{v}_{il} - \vec{v}_{el}) \tag{3.8}$$

using equations (3.1) and (3.2), equation (3.8) is reduced to

$$\nabla \times \nabla \times \vec{E} - \Omega \vec{E} = \omega^2 \mu_o e \left(\frac{U_i^2}{\omega^2 - j\omega\nu_i} \nabla n_{il} - \frac{U_e^2}{\omega^2 - j\omega\nu_e} \nabla n_{el} \right) \tag{3.9}$$

where

$$\Omega = \frac{\omega^2}{c^2} \left(1 - \frac{\omega_{p-}^2}{\omega^2 + j\omega\nu_e} - \frac{\omega_{p+}^2}{\omega^2 + j\omega\nu_i} \right) \tag{3.10}$$

$$\omega_{p-}^2 = \frac{N_o e^2}{\epsilon_o m_e} \quad ; \quad \omega_{p+}^2 = \frac{N_o e^2}{\epsilon_o m_i}$$

$$U_e^2 = \frac{KT_e}{m_e} \quad ; \quad U_i^2 = \frac{KT_i}{m_i}$$

Equation (3.1), (3.3) and (3.5) can be combined to produce

$$(\omega^2 - \omega_{p-}^2 - j\omega\nu_e + U_e^2 \nabla^2) n_{el} + \omega_{p-}^2 n_{il} = 0 \tag{3.11}$$

In the case of plane wave propagation, $\nabla = j\vec{k}$, equation (3.11) becomes

$$(\omega^2 - \omega_{p-}^2 - j\omega\nu_e - U_e^2 k^2) n_{el} + \omega_{p-}^2 n_{il} = 0 \tag{3.12}$$

Equation (3.12) and the divergence of equation (3.5) are then combined to give

$$- \vec{k}(\vec{k} \cdot \vec{E}) = \frac{-e}{\epsilon_o} \frac{(\omega^2 - j\omega\nu_e - U_e^2 k^2)}{\omega_{p-}^2} (j k n_{el}) \qquad (3.13)$$

From equation (3.9), (3.12) and (3.13), a differential equation for the electric field in plasma is obtained

$$-\vec{k} \times \vec{k} \times \vec{E} + \beta \vec{k}(\vec{k} \cdot \vec{E}) - \Omega \vec{E} = 0 \qquad (3.14)$$

where

$$\beta = \frac{\omega^2}{c^2(\omega^2 - j\omega\nu_e - U_e^2 k^2)} \left[\frac{U_i^2(\omega^2 - \omega_{p-}^2 - j\omega\nu_e - U_e^2 k^2)}{\omega^2 - j\omega\nu_e} + \frac{U_e^2 \omega_{p-}^2}{\omega^2 - j\omega\nu_e} \right] \qquad (3.15)$$

In general, the electric field, $\vec{E}$, can be broken into two linearly independent parts: a solenoidal part, $\vec{E}_s$, corresponding to the transverse electromagnetic part of the field, and an irrotational part corresponding to the longitudinal electroacoustic part of the field[8], that is

$$\vec{E} = \vec{E}_s + \vec{E}_{irr} \qquad (3.16)$$

where

$$\nabla \times \vec{E}_{irr} = 0 \quad ; \quad \vec{k} \times \vec{E}_{irr} = 0 \qquad (3.17)$$

$$\nabla \cdot \vec{E}_s = 0 \qquad (3.18)$$

From equation (3.14), the longitudinal electroacoustic part of the field obeys the following equations:

$$\vec{k}\,\vec{k}\cdot\vec{E}_{irr} - \frac{\Omega}{\beta}\,\vec{E}_{irr} = 0$$

or

$$(k^2 - \frac{\Omega}{\beta})\,\vec{E}_{irr} = 0 \qquad (3.19)$$

Solving for k yields

$$k^2 = \frac{\Omega}{\beta} \qquad (3.20)$$

Equation (3.10), (3.15) and (3.20) can now be combined to yield the dispersion relation for the electroacoustic wave

$$\frac{\omega_{p-}^2}{\omega^2 - j\omega\nu_e - U_e^2 k^2} + \frac{\omega_{p+}^2}{\omega^2 - j\omega\nu_i - U_i^2 k^2} = 1 \qquad (3.21)$$

In the plasma system, the physical lengths are small in comparison with the electromagnetic wavelength. Thus, one can approximate the electromagnetic field by quasi-static approximation; i.e., $E_s = -\nabla\phi_e$. The equation for E_s is simply equation (3.18). Then,

$$\vec{E}_s = \vec{A}_o$$

where A_o is a constant vector. Since E_y and E_z are tangent to the metallic plates, they must vanish at the plat at $x = \pm(L-s)/2$. Therefore they are zero everywhere between the plates.

Due to this quasi-static approximation, one would not expect to have any electromagnetic wave phenomenon inside the plasma-filled capacitor.

In the case of a one-dimensional plasma capacitor, the charge density, and hence the electric field, varies only with x. Equation

(3.17) indicates that $\vec{E}_{irr}$ is parallel to $\vec{k}$. Therefore for waves propagating in the x direction, E_{irr} is in the x direction. Furthermore, $\vec{E}_{irr}$ can be written as the gradient of a plasma potential (i.e., $\vec{E}_{irr} = -\nabla\phi_p$). By assuming standing wave solutions, the electro-acoustic part of the field is of the form

$$E_{irr} = A_1 \cos k_1 x + A_2 \sin k_1 x + A_3 \cos k_2 x + A_4 \sin k_2 x \qquad (3.24)$$

where $A_1 \ldots A_4$ are arbitrary constants determined from boundary conditions, while k_1 and k_2 are the two positive roots of the fourth-order dispersion equation (3.21).

From equations (3.23) - (3.24), the total electric field in the plasma is given by

$$E = A_1 \cos k_1 x + A_2 \sin k_1 x + A_3 \cos k_2 x + A_4 \sin k_2 x + A_o \qquad (3.25)$$

The complexity of the problem can be simplified with a cold ion approximation ($T_i = 0$). Such an approximation is justified here, because $T_e >> T_i$ in the experimental plasma.

At high frequency ($\omega \gtrsim \omega_{p-}$), the phase velocity of the ion-acoustic wave is equal to the ion thermal speed (i.e., $v_{ph} = KT_i/m_i$). The cold ion approximation assumes that the ion-acoustic wave does not exist at high frequency. This is a good assumption since a more accurate analysis using particle distribution function, f, shows that the ion acoustic mode is heavily Landau damped for $\omega >> \omega_{p-}$; $T_e >> T_i$. Thus, physically, it can not exist as a wave at these high frequencies. As a result, in the model developed here, the ions form a stationary background in the plasma when $\omega \gtrsim \omega_{p-}$.

At low frequency ($\omega \lesssim \omega_{p+}$), a look at the ion-acoustic mode shows that the cold ion approximation is not good for $\omega \gtrsim \omega_{p+}$, but it is valid for $\omega < \omega_{p+}$ [44].

This cold ion approximation reduces the dispersion relation (3.21) to a quadratic equation in k. That is

$$\frac{\omega_{p-}^2}{\omega^2 - j\omega\nu_e - U_e^2 k^2} + \frac{\omega_{p+}^2}{\omega^2 - j\omega\nu_i} = 1$$

or

$$k = \left[\frac{(\omega^2 - j\omega\nu_e)(\omega^2 - \omega_{p+}^2 - j\omega\nu_i) - \omega_{p-}^2(\omega^2 - j\omega\nu_i)}{U_e^2(\omega^2 - \omega_{p+}^2 - j\omega\nu_i)} \right]^{1/2} \tag{3.26}$$

From equation (3.25), the electric field in the plasma becomes

$$E = A_1 \cos kx + A_2 \sin kx + A_o \tag{3.27}$$

If collisions in the plasma are neglected ($\nu_e = \nu_i = 0$), the phase velocity obtained from equation (3.26) is

$$v_{ph} = U_e \left(\frac{1 - \omega_{p+}^2/\omega^2}{1 - \omega_{p+}^2/\omega^2 - \omega_{p-}^2/\omega^2} \right)^{1/2} \tag{3.28}$$

The high and low frequency modes of the cold ion approximation are shown in the plot of phase velocity versus frequency below.

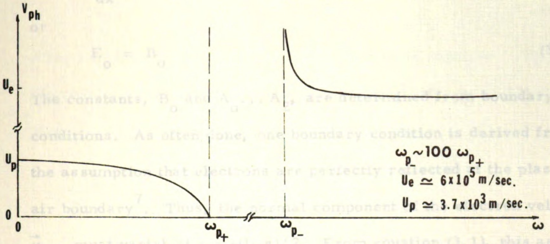

In the investigation below, a discussion for the high and low frequency modes of the plasma capacitor are given.

3.2 Resonance at high frequency ($\omega \gtrsim \omega_{p-} >> \omega_{p+}$)

At high frequency, the ions are assumed fixed (i.e., $U_i = 0$, $\nu_i = 0$, $\vec{v}_{il} = 0$ and $n_{il} = 0$). The disperson equation (3.26) can then be written as

$$k = \frac{\omega}{U_e}\left(1 - \frac{\omega_{p-}^2}{\omega^2} - j\frac{\nu_e}{\omega}\right)^{1/2} \tag{3.29}$$

The electric field in the plasma slab, E_p, is given by equation (3.27)

$$E_p = A_1 \cos k\ x + A_2 \sin kx + A_o \tag{3.30}$$

In the vacuum sheath, the quasi-static electric field, E_o, satisfies Laplace's equation. Consequently

$$\frac{dE_o}{dx} = 0$$

or

$$E_o = B_o \tag{3.31}$$

The constants, B_o and $A_o \ldots A_2$, are determined from boundary conditions. As often done, one boundary condition is derived from the assumption that electrons are perfectly reflected at the plasma-air boundary[7]. Thus, the normal component of the electron velocity, $\vec{v}_{el}$, must vanish at $x = \pm(L-s)/2$. From equation (3.1), this assumption implies that there exists an electric field, $\vec{E} = -(KT_e/N_o e)\nabla n_{el}$, at the plasma-sheath interface physically, the electrons are not allowed to build up a charge layer at the interface when $T_e \neq 0$.

Other boundary conditions are the continuity of total current and $V(t) = \int \vec{E} \cdot d\vec{r}$. The latter is obtained from the quasi-static approximation which relates the externally applied rf voltage, V(t), to the electric fields in the plasma capacitor. To summarize, the boundary condition used are:

(i) $\vec{x} \cdot \vec{v}_{el} = 0 \qquad$ at $\quad x = \pm(L-s)/2$

(ii) $j\omega\epsilon_o \vec{E}_o = j\omega\epsilon_o \vec{E}_p(x) + \vec{J}_p(x)$ for any x in the plasma

(iii) $V(t) = \int_{-L/2}^{-(L-s)/2} E_o dx + \int_{-(L-s)/2}^{(L-s)/2} E_p dx + \int_{(L-s)/2}^{L/2} E_o dx$

Form the continuity of total current(ii), the boundary condition (i) and equations (3.30) - (3.31) the following relations hold at $x = \pm(L-s)/2$

$$B_o = A_o + A_1 \cos k(L-s)/2 \tag{3.32}$$

$$A_2 = 0 \tag{3.33}$$

After applying the first boundary condition (i) to equation (3.1), the result is combined with equations (3.5), (3.30) and (3.33) to give

$$A_o = -\left(1 + \frac{U_e^2 k^2}{\omega_{p-}^2}\right) A_1 \cos k(L-s)/2 \tag{3.34}$$

Using equations (3.32) to (3.34), the electric fields can be simplified to the following forms

$$E_o = -\frac{U_e^2 k^2}{\omega_{p-}^2} A_1 \cos \frac{k(L-s)}{2} \tag{3.35}$$

$$E_p = A_1 \left[\cos kx - \left(1 + \frac{U_e^2 k^2}{\omega_{p-}^2}\right)\cos \frac{k(L-s)}{2}\right] \tag{3.36}$$

Because of the symmetrical geometry, the electric field is an even function of position. The third boundary condition (iii) along with equation (3.35) to (3.36) yields

$$A_1 = \frac{-V(t)}{\left[L\left(1 + \frac{U_e^2 k^2}{\omega_{p-}^2}\right) - s\right]\cos\frac{k(L-s)}{2} - \frac{2}{k}\sin\frac{k(L-s)}{2}}$$

From equation (3.29), the last equation becomes

$$A_1 = \frac{V(t)}{\left[s - \frac{L(\omega^2 - j\omega\nu_e)}{\omega_{p-}^2} \right] \cos\frac{k(L-s)}{2} + \frac{2}{k} \sin\frac{k(L-s)}{2}} \tag{3.37}$$

Substituting equation (3.37) into equation (3.35) - (3.36), the electric fields then have the following forms

$$E_o = \frac{V(t)(\omega_{p-}^2 - \omega^2 + j\omega\nu_e)}{[s\omega_{p-}^2 - (\omega^2 - j\omega\nu_e)L] + \frac{2\omega_{p-}^2}{k} \tan\frac{k(L-s)}{2}} \tag{3.38}$$

$$E_p = \frac{-V(t)\left[(\omega^2 - j\omega\nu_e) - \omega_{p-}^2 \frac{\cos kx}{\cos k(L-s)/2}\right]}{[s\omega_{p-}^2 - (\omega^2 - j\omega\nu_e)L] + \frac{2\omega_{p-}^2}{k} \tan\frac{k(L-s)}{2}} \tag{3.39}$$

(A) The variation of electric field as a function of plasma density. The normalized amplitudes of the electric fields of equations (3.38) - (3.39) are plotted as a function of ω_{p-}/ω in Figure 3.1 for the following parameters: L = 1.6 mm, s = .6 mm, x = 0, ω/U_e = 2×10^4 and $\nu_e/\omega = .001$. These parameters are so chosen because of the later experimental conditions. In addition, the phases of E_o and E_p versus ω_{p-}/ω are shown in Figure 3.2. The following results are obtained:

(1) The main and temperature resonances of the plasma capacitor are cl oearly demonstrated in the variation of the electric fields. At resonance, both E_o and E_p are much larger than the electric field of an air capacitor of plate separation L(i.e., E = V(t)/L). For each temperature resonance, there is an anti-resonance

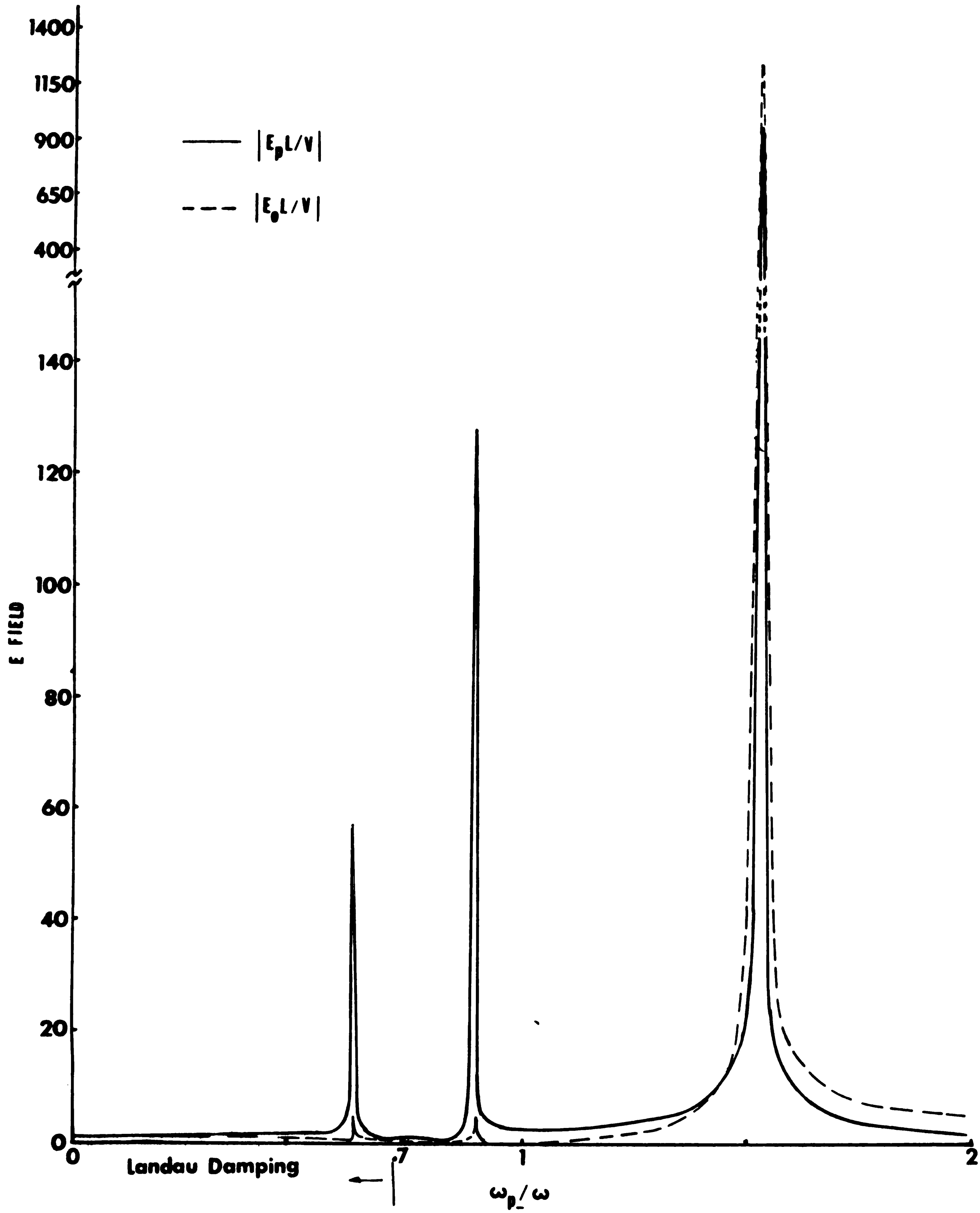

Figure 3.1 Normalized amplitude of the high frequency electric fields, $|LE_o/V|$ and $|LE_p/V|$, vs. ω_{p-}/ω ($L = 1.6$ mm, $s = .6$ mm, $\omega/U_e = 2 \times 10^4$, $\nu_e/\omega = .001$, $x = 0$)

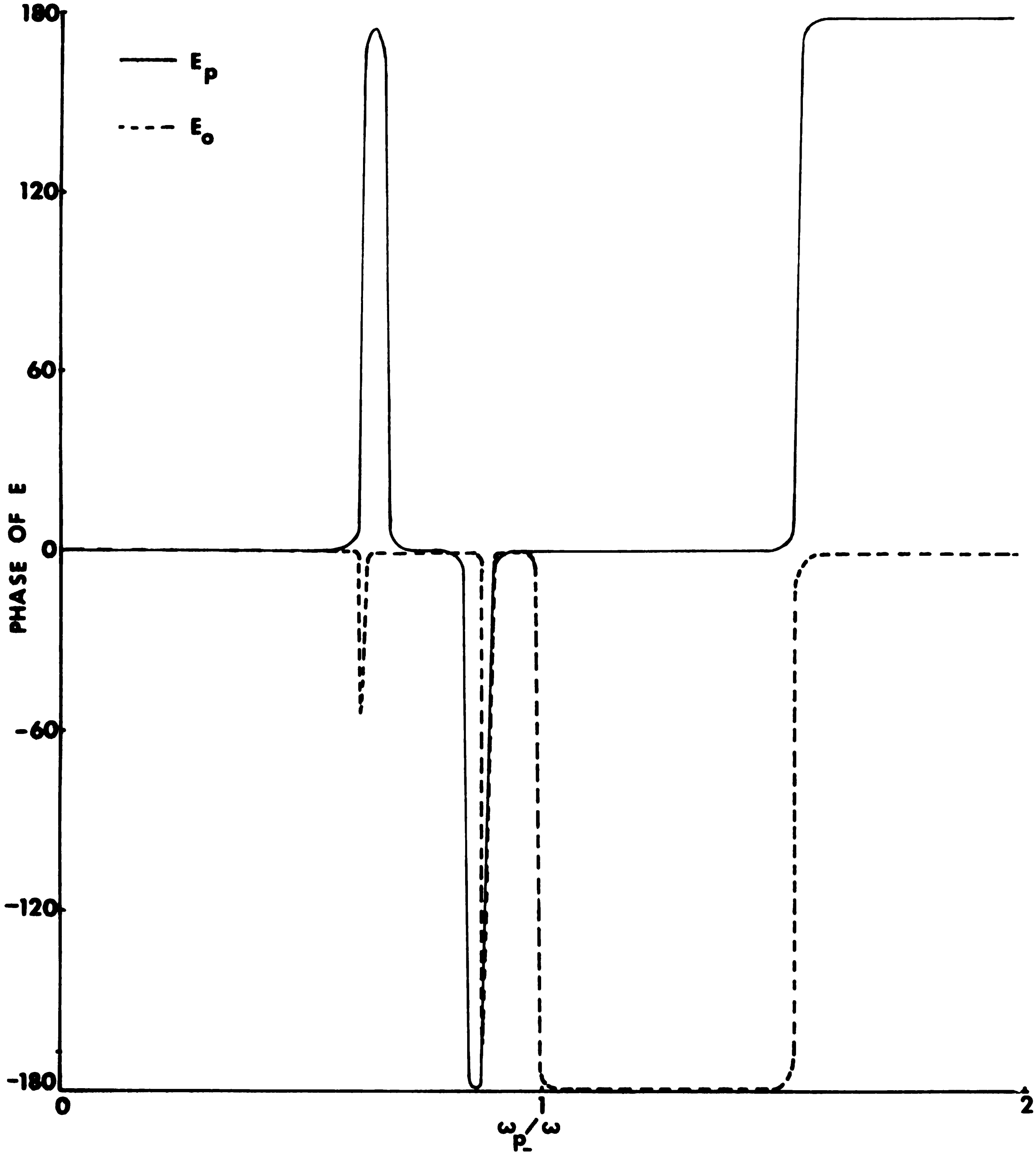

Figure 3.2 Phase of the high frequency electric fields, E_o and E_p, vs. ω_{p-}/ω (L = 1.6 mm, s = .6 mm, $\omega/U_e = 2 \times 10^4$, $\nu_e/\omega = .001$, x = 0).

($E_o = 0$) at almost the same plasma density. There is always an anti-resonance at $\omega \sim \omega_{p-}$.

(2) As shown in Figure 3.2, E_o and E_p are 180^o out of phase at the main resonance. This is consistent with Hatch's experimental observation[29]. Physically, the vacuum sheath is capacitive, while the plasma slab is inductive at resonance.

(3) The collisions in the plasma cause damping of the resonances. It is shown in Table 3.1 that by increasing the collision frequency from $\nu_e/\omega = 10^{-3}$ to 10^{-2}, the resonances are damped by approximately 9 to 10 times; whereas the resonant frequency is shifted only slightly

	$\nu_e/\omega = .001$			$\nu_e/\omega = .01$		
	ω_e/ω	$\lvert E_oL/V\rvert$ (sheath)	$\lvert E_pL/V\rvert$ (pasma)	ω_e/ω	$\lvert E_oL/V\rvert$ (sheath)	$\lvert E_pL/V\rvert$ (plasma)
main res.	1.526	1240	937	1.526	139	105
1st temp.	.890	4.24	128	.890	.571	12.8
2nd temp.	.624	4.03	57.4	.622(.63)	(.953)	6.68

Table 3.1 The effect of collisions on the normalized amplitudes of the electric fields at resonance

(4) In addition to the main resonance predicted by the cold plasma theory, the electron temperature, T_e, introduces a discrete number of temperature resonances and anti-resonances in a warm plasma. The number of temperature resonances increases with a

decrease in electron temperature. By keeping ω constant, and increasing ω/U_e (i.e., decreasing T_e) from 2×10^4 to 3×10^4, the number of temperature resonances increases from two to four respectively as shown in Figure 3.3. The physical explanation of this phenomenon can be seen from the dispersion relation (3.29). At high frequency ($\omega >> \omega_{p-}$, ν_e), the phase velocity of the electron plasma wave approaches the electron thermal velocity U_e; i.e., $\omega/k \sim U_e$. Consequently, $\lambda = U_e/f$. A decrease in electron temperature decreases the wavelength λ and thus allows more resonant states to exist in the plasma capacitor. (Note that the curves in Figure 3.1 to 3.5 are plotted for a constant ω/U_e ratio. Thus, λ is limited at high frequency.) Collisionless Landau damping becomes important when $k\lambda_D > 1$.[45] From equation (3.29), this corresponds to $(\omega^2/\omega_{p-}^2 - 1)^{1/2} > \gamma^{1/2}$. Thus, the Landau damping of the resonances is important when $\omega_{p-}/\omega \lesssim .7$. The Landau damped region has been indicated in the figures. The temperature effect has relatively small influence on the resonance frequency of the main resonance, while drastically changes the resonant frequencies of the temperature resonances. The resonant frequency for the main resonance of a warm plasma is slightly lower than $\omega_{p-}(s/L)^{1/2}$ which is the resonant frequency obtained from cold plasma theory.

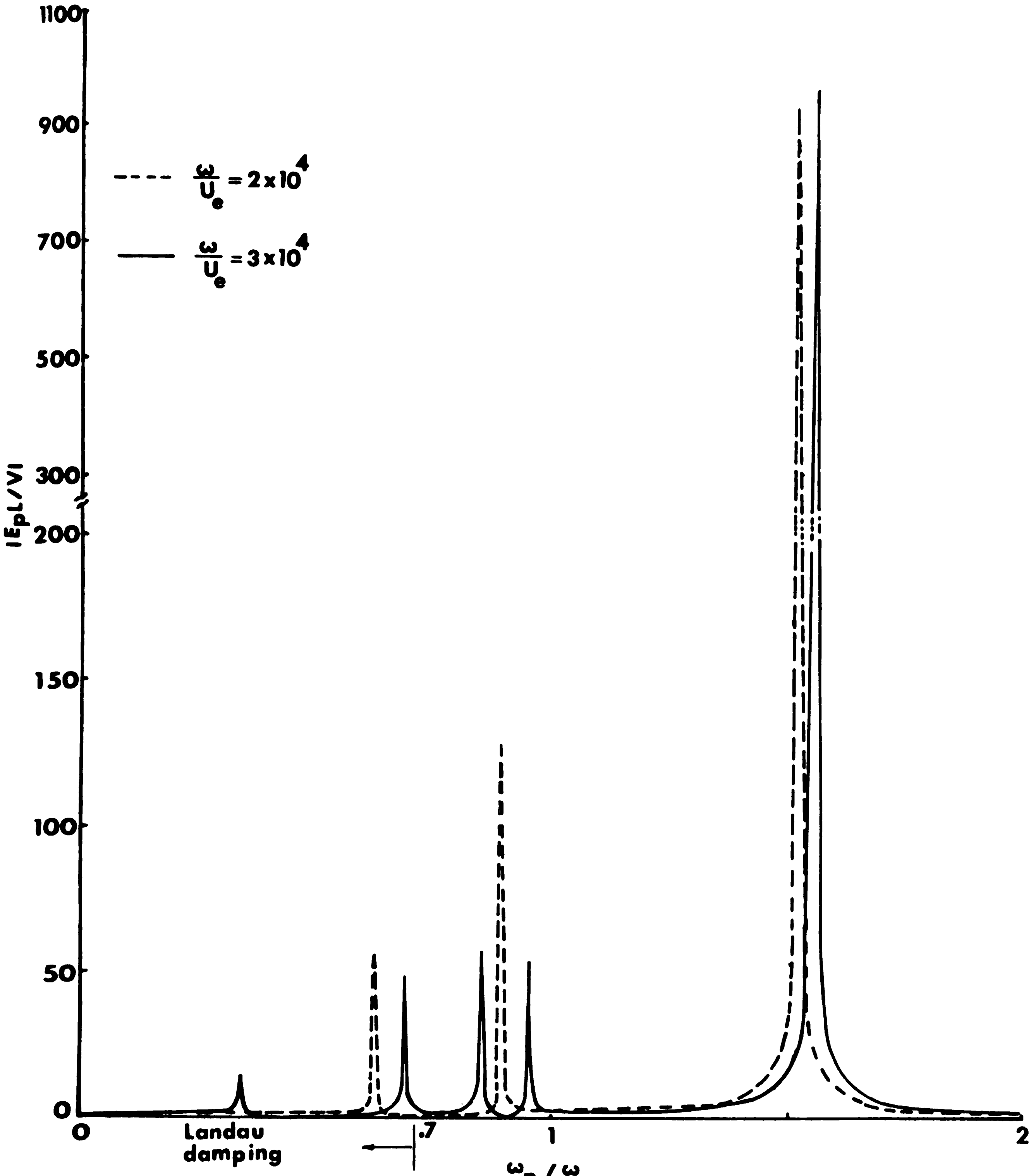

Figure 3.3 Normalized amplitudes of the high frequency plasma field, $|LE_p/V|$, vs. ω_{p-}/ω for different electron temperature, T_e, ($L = 1.6$ mm, $s = .6$ mm, $\nu_e/\omega = .001$, $x = 0$, $\omega/U_e = 2\times10^4$, 3×10^4)

(5) The influence of the sheath on the resonances of a collisional, warm plasma is shown in Figure 3.4. As the sheath, s, is increased, the temperature resonances are found to occur at lower plasma densities. In the case of the main resonance, increasing the sheath from .2 mm to .6 mm results in a change of ω_{p-}/ω from 2.57 to 1.53 respectively. The cold plasma theory ($T_e = 0$) explains this resonance quite well.[46]

(B) The variation of electric field as a function of position.
The spatial variation of the real part of electric field is shown in Figure 3.5(a) for the main resonance, and in Figure 3.5 (b)-(c) for the temperature resonance. These resonances correspond to the case of Figure 3.1. Each resonance is shown at a time when the electric field has reached its maximum value.

As shown in Figure 3.5(a), there is no wave phenomenon associated with the main resonance ($\omega_{p-}/\omega = 1.526$). It is clear that the physical origin of this resonance comes from a resonance between the inductive effect of the plasma and the capacitive effect of the sheath. For the temperature resonances, standing waves exist in the uniform plasma region. The occurrence of the temperature resonance requires that $(L-s) \sim (N + \frac{1}{2})\lambda$, where $N = 1, 2, 3 \ldots$. These results can be also obtained from the impedance approach as done by Vandenplas.[46]

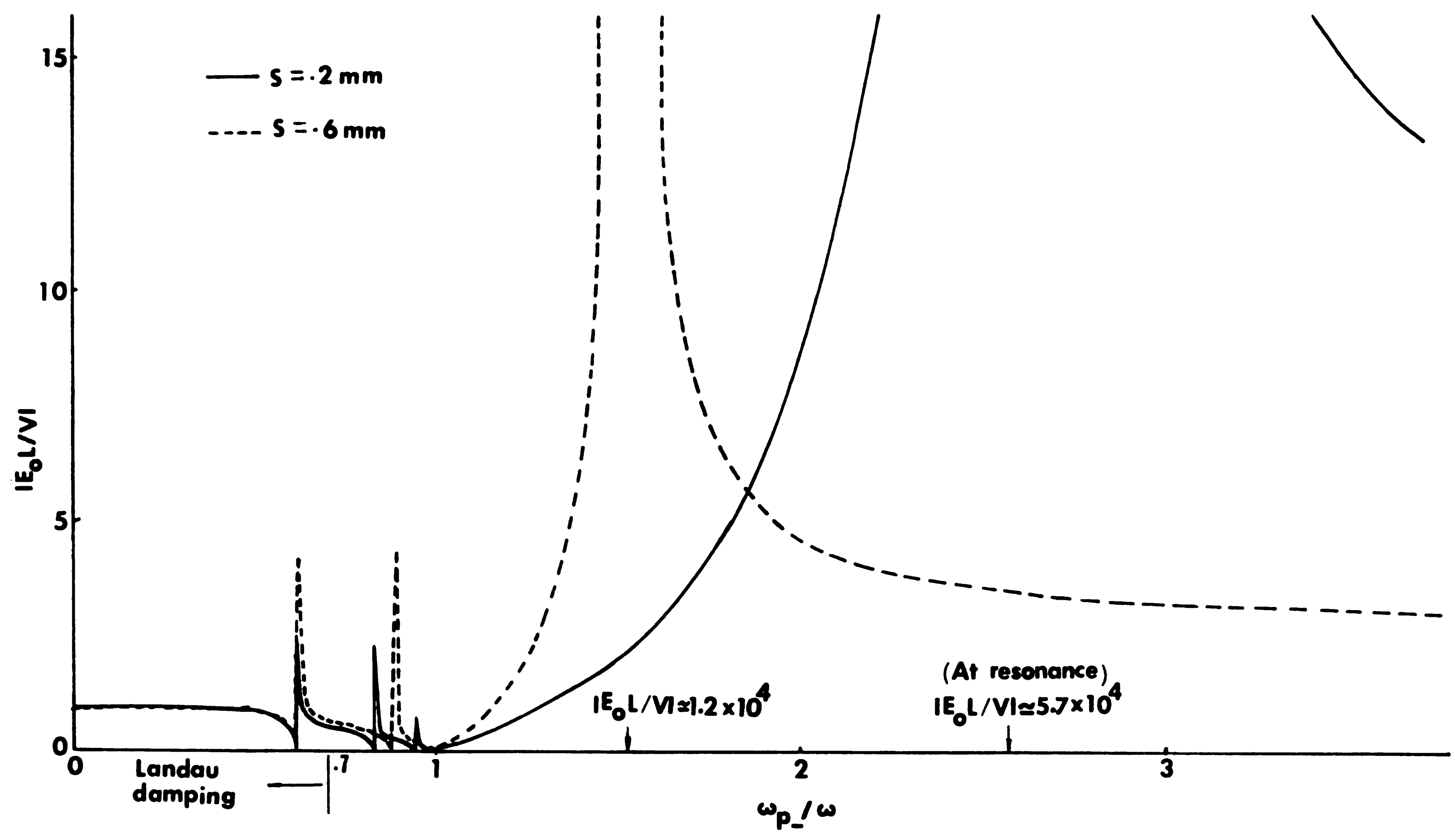

Figure 3.4 Normalized amplitude of the high frequency sheath field $|LE_o/V|$ vs. ω_{p-}/ω for different sheath thickness, s, (L = 1.6 mm, ν_e/ω = .001, ω/U_e = 2 x 10^4, x = 0, s = .2 mm and .6 mm)

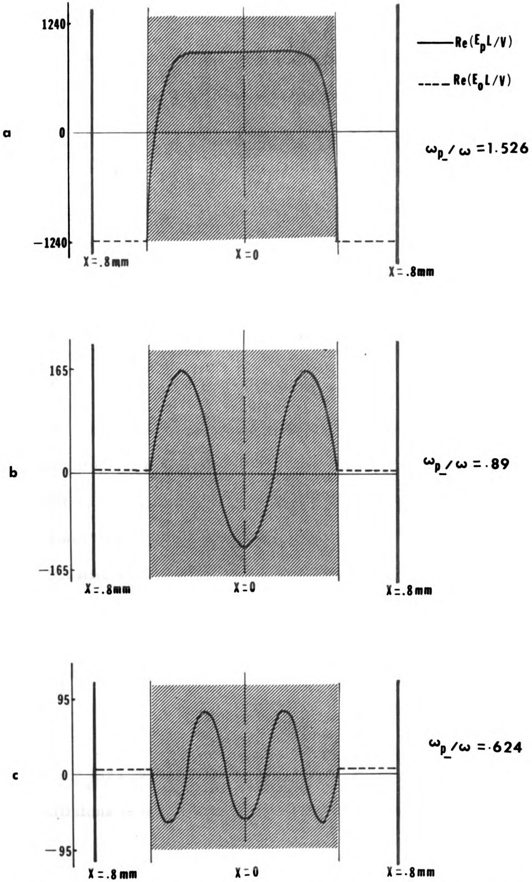

Figure 3.5 Real part of the normalized high frequency plasma field LE_p/V vs. position x at resonance (L = 1.6 mm, ω/U_e = 2 x 10 , s = .8 mm, ν_e/ω = .001)

(C) Impedance and equivalent circuit

The impedance of the plasma capacitor system is defined as

$$Z = V(t)/I$$

where

$$I = j\omega\epsilon_o S E_o$$

S is the surface area of the capacitor plate. In terms of E_o, the impedance, Z, is of the form

$$Z = V(t)/j\omega\epsilon_o S E_o \tag{3.41}$$

Similarly, the admittance, Y, can be written as

$$Y = j\omega\epsilon_o S E_o/V(t)$$

Hence, the amplitude of the admittance, Y, is directly proportional to the amplitude of the electric field in the vacuum sheath; i.e., the admittance variation differs only by a constant from figures 3.1, 3.3 and 3.4.

Substitution equation (3.39) in equation (3.41) yields

$$Z = -\frac{1}{j\omega C}\ \frac{\left[\frac{\omega_{p-}^2}{\omega^2} - \frac{L}{s}\left(1 - j\frac{\nu_e}{\omega}\right)\right] + \frac{2}{ks}\ \frac{\omega_{p-}^2}{\omega^2}\tan k(L-s)/2}{\left(1 - \frac{\omega_{p-}^2}{\omega^2} - j\frac{\nu_e}{\omega}\right)} \tag{3.42}$$

where $C = \epsilon_o S/s$ is the total capacitance of the two vacuum sheaths. If the collisions in the plasma is negelected, equation (3.42) becomes

$$Z = \frac{1}{j\omega C}\left[1 + \frac{1 - L/s}{\omega_{p-}^2/\omega^2 - 1} + \frac{2}{ks}\,\frac{\omega_{p-}^2}{\omega^2}\,\frac{\tan k(L-s)/2}{\omega_{p-}^2/\omega^2 - 1}\right] \quad (3.43)$$

where

$$k = \frac{\omega}{U_e}\left(1 - \frac{\omega_{p-}^2}{\omega^2}\right)^{1/2}$$

Equation (3.43) can be represented by an equivalent circuit which consists of a lossless transmission line terminated in a short

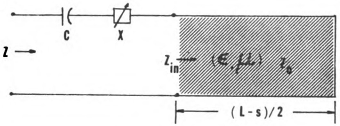

where

$$C_p = \frac{C(1 - \omega_{p-}^2/\omega^2)}{(L/s - 1)} \qquad (\omega > \omega_{p-})$$

$$L_p = \frac{(L/s - 1)}{C(\omega_{p-}^2 - \omega^2)} \qquad (\omega < \omega_{p-})$$

X is C_p or L_p depending on whether ω is greater or less than ω_{p-}.

$$Z_{in} = j\, Z_o \tan\frac{k(L-s)}{2} \quad (3.44)$$

From equation (3.43), the input impedance to the shorted transmission line is also given by

$$Z_{in} = j\,\frac{2}{C^s}\,\frac{\omega_{p-}^2}{\omega^3}\,\frac{\tan k\,(L-s)/2}{k(1 - \omega_{p-}^2/\omega^2)} \quad (3.45)$$

According to the transmission line theory,

$$Z_o = (Z'/Y')^{1/2} \tag{3.46}$$

$$j\,k = (Z'\,Y')^{1/2} \tag{3.47}$$

By defining the series impedance per unit length of the line, Z', and the shunt admittance, Y', as follows:

$$Z' = j\omega$$

$$Y' = j\omega\epsilon + \omega_{p-}^{2}\,\epsilon/j\omega$$

Equations (3.46) - (3.47) can be reduced to the following forms

$$k = \omega[\mu\epsilon\,(1 - \omega_{p-}^{2}/\omega^{2})]^{1/2} \tag{3.48}$$

$$Z_o = \frac{1}{[\,(\epsilon/\mu)(1 - \omega_{p-}^{2}/\omega^{2})]^{1/2}} \tag{3.49}$$

Clearly, $\omega = \omega_{p-}$ represents the cut-off condition for wave propagation in the transmission line. Equations (3.44), (3.45), (3.48) and (3.49) are combined to produce the following results

$$\mu\epsilon = 1/U_e^{2}$$

$$\epsilon = \frac{\epsilon_o S}{2}\;\frac{\omega^{2}}{U_e^{2}}\;(\omega^{2}/\omega_{p-}^{2} - 1)$$

$$\mu = \frac{2}{\epsilon_o S}\;\frac{1}{\omega^{2}(\omega^{2}/\omega_{p-}^{2} - 1)}$$

The equivalent circuit for shorted transmission line is shown below.

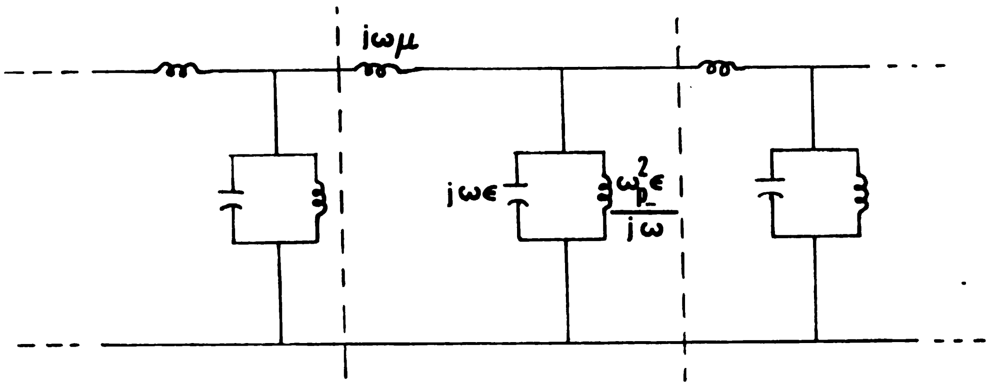

At resonance (Z=0), equation (3.43) can be written as

$$\frac{k(L-s)}{2} + \frac{L}{2}\,\frac{k^2}{\mu^2/U_e^2 - k^2} = \tan\frac{k(L-s)}{2} \qquad (3.50)$$

(D) Magnitude of the admittance for the main and temperature resonances.

An important phenomena arises when the temperature or sheath size varies in a plasma; namely, the admittance varies. The physical interpretation of this phenomena is considered here. Figures 3.3 and 3.4 show that the main resonance admittance increases with either an increase in electron temperature, T_e, or a decrease in sheath thickness, s. Since the plasma is a pure conductance near the resonance peak, the height of the resonance depends directly on the conductivity of the plasma. From cold plasma theory, the conductivity is directly proportional to the plasma density, ω_{p-}; i.e., $\sigma \simeq \frac{\epsilon_o \omega_{p-}^2 \nu_e}{\omega^2}$ for $\omega^2 >> \nu_e^2$. Thus the increase in height of the main resonance results from a shift of resonance position to a higher density.

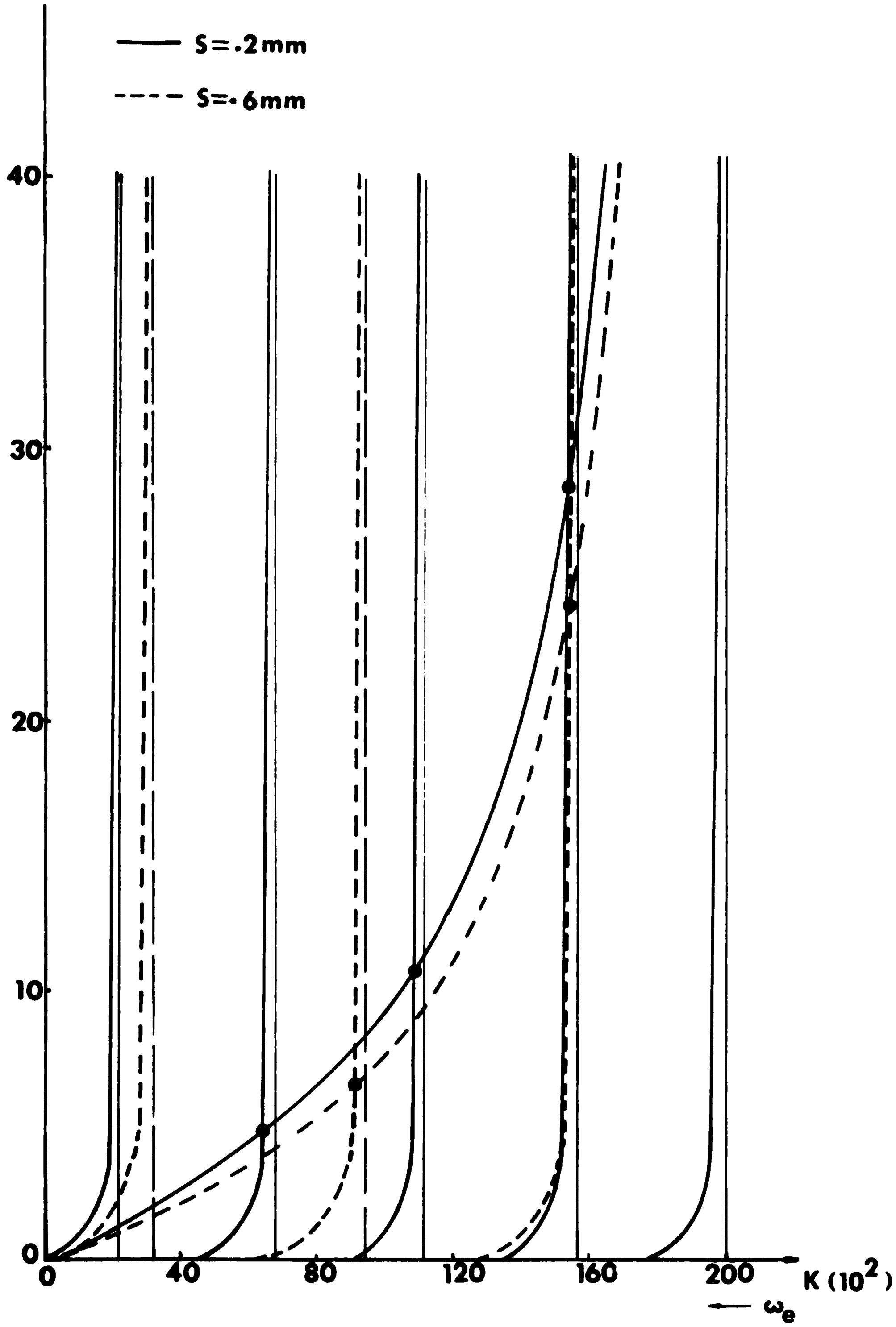

Figure 3.6 Graphical solution of the high frequency capacitor impedance for different sheath thickness, s, (L = 1.6 mm, $\omega/U_e = 2 \times 10^4$, s = .2 mm and .6 mm)

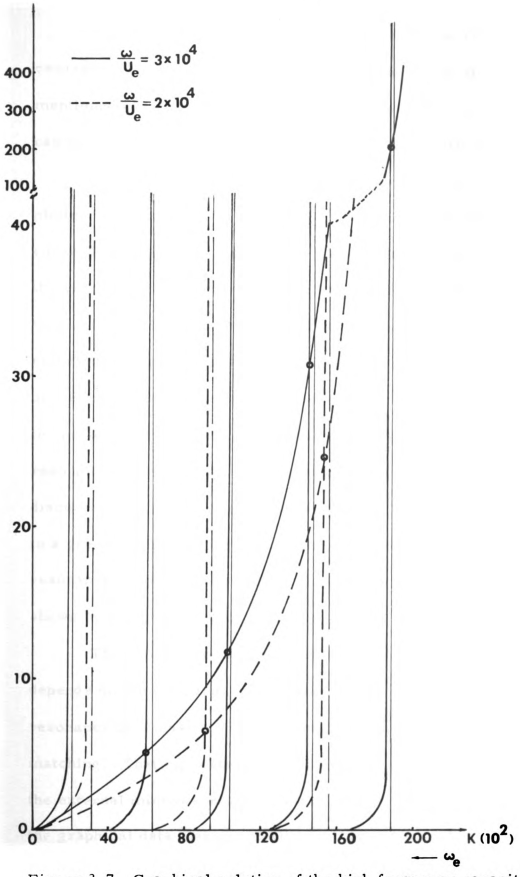

Figure 3.7 Graphical solution of the high frequency capacitor impedance for different electron temperature, T_e, (L = 1.6 mm, s = .6 mm, ω/U_e = 2 x 10^4 and 3 x 10^4)

Unlike the main resonance, the temperature resonance decrease in height (i.e., the admittance decrease) for the above mentioned changes of T_e and s. Physical insight into this phenomenon can be obtained from the graphical solution of equation (3.50).

In Figures 3.6 and 3.7, the two sides of equation (3.50) are plotted as a function of k for $\omega > \omega_{p-}$. The points of intersection correspond to the electroacoustic (or temperature) resonances, while the asymptotic lines of the tangent function locate the anti-resonances (i.e., $Z = \infty$). The resonance and anti-resonance are spaced very close to each other. The spacing decreases with increasing order of electroacoustic resonance. One important effect of varying the temperature or sheath in a plasma is manifested in a shift of resonance position and a change in the number of resonances as discussed earlier. An increase in T_e or a decrease in s results in a greater separation of the electroacoustic resonance and anti-resonance, and a subsequent increase of the resonance peak as shown by the graphical solutions.

The experimental observation of electroacoustic resonance depends on the coupling of the external circuit to the electroacoustic resonance in a plasma. This of course is a matter of impedance matching. That is, matching the plasma capacitor impedance to the external microwave system impedance. One can observe from the graphical data that an impedance match between a resonance plasma and a given microwave system usually does not occur. This is particularly true for the temperature resonances. In fact, it has been pointed out that the microwave coupling to the temperature resonances is poor[46]. The large impedance mismatch, of course, explains this.

An analogy between the coupling of a metal cavity to a microwave system and the coupling of a resonant plasma to a microwave system can be made. In a metal cavity, one must adjust the coupling loop position, size, etc., or aperture-size, etc., for maximum coupling (i.e., to a critical coupled condition). With a plasma resonator, there are no such metallic loops available. In order to improve coupling, one must adjust (in the case discussed here) L, s and T_e for maximum coupling. This is not always experimentally possible; thus many of the resonances are not observed at all, or are observed as very weak interactions. This is particularly true for the higher order temperature resonances of a plasma column.

The coupling to the plasma resonances can be improved by building metal impedance transforming networks (i.e., slide screw tuners, microwave cavity, sliding short, etc.) around the plasma. This has been done by those working with harmonic generation[32, 33].

3.3 Resonance at low frequency ($\omega < \omega_{p+}$)

At low frequency, the thermal motions of the ions are neglected ($U_i = 0$). The electric field in the plasma is given by equation (3.27).

$$E_p = C_1 \cos kx + C_2 \sin kx + C_o \tag{3.51}$$

where k is given by the dispersion relation (3.26). The electric field in the vacuum sheath is obtained again from Laplace's equation.

$$E_o = G_o = \text{constant} \tag{3.52}$$

Since the ions are assumed cold ($T_i = 0$), equation (3.2) is then reduced to

$$\vec{v}_{i1} = \frac{e\vec{E}_p}{(j\omega + \nu_i)m_i} \tag{3.53}$$

The ion acoustic wave at the sheath has been seen to possess both reflective and absorptive characteristics depending on the nature of the sheath. The reflection of the ion-acoustic wave occurs at an electron rich sheath (positive bias on reflecting surface) or an ion rich sheath (negative bias on reflecting surface) of a "perturbed" plasma[47], while the absorption of the ion-acoustic wave is resulted from an ion rich sheath[48]. Thus, no definite boundary condition for the ion-acoustic wave at the sheath has been established. As a result, the same boundary conditions for the high frequency electro-acoustic wave are applied to the low frequency ion wave here. These boundary conditions are used for lack of better boundary conditions.

(i) $\vec{x} \cdot \vec{v}_{el} = 0 \quad \text{at } x = \pm (L-s)/2$

(ii) $j\omega \epsilon_o \vec{E}_o = j\omega \epsilon_o \vec{E}_p + J_p$

(iii) $V(t) = \int_{-L/2}^{-(L-s)/2} E_o dx + \int_{-(L-s)/2}^{(L-s)/2} E_p dx + \int_{(L-s)/2}^{L/2} E_o dx$

In the absence of the ion pressure (i.e., $KT_i \nabla n_{el}/N_o e = 0$), the ions may form a rf charge layer at the plasma-sheath interface. The continuity of total current (ii) is then of the form

$$j\omega\epsilon_o \vec{E}_o = N_o e \vec{v}_{il} + j\omega\epsilon_o \vec{E}_p \tag{3.54}$$

Equations (3.51) to (3.54) are combined to produce the following results at $x = \pm(L-s)/2$.

$$G_o = \left(1 - \frac{\omega_{p+}^2}{\omega^2 - j\omega\nu_i}\right)\left(C_o + C_1 \cos\frac{k(L-s)}{2}\right) \tag{3.55}$$

$$C_2 = 0 \tag{3.56}$$

From equations (3.2), (3.4) and (3.5), the following equation is obtained.

$$n_{il} = \frac{\omega_{p+}^2}{\omega^2 - \omega_{p+}^2 - j\omega\nu_i}\, n_{el} \tag{3.57}$$

Applying the boundary condition (i) to equation(3.1) yields

$$E_p = -\frac{KT_e}{N_o e}(jkn_{el}) \tag{3.58}$$

By combining equations (3.13), (3.57) and (3.58) with the dispersion relation (3.26), the following result is obtained at $x = \pm(L-s)/2$.

$$C_o = \frac{(\omega_{p+}^2 - \omega^2 + j\omega\nu_i)(\omega - j\nu_e)}{\omega_{p-}^2(\omega - j\nu_i)}\, C_1 \cos\frac{k(L-s)}{2} \tag{3.59}$$

From the boundary condition (iii) and equations (3.51) - (3.52), it can be shown that

$$V(t) = s\,G_o + (L-s)\,C_o - \frac{2C_1}{k}\sin\frac{k(L-s)}{2} \tag{3.60}$$

Now, the constants are solved from equation (3.55), (3.59) and (3.60) in terms of V(t). After substituting the known constants into equations (3.51) and (3.52), the electric fields in the plasma and in the sheath have the following form

$$E_p = \frac{-V(t)\left[\omega - j\nu_e + \dfrac{\omega_{p-}^2(\omega + j\nu_i)}{\omega_{p+}^2 - \omega^2 - j\omega\nu_i}\;\dfrac{\cos kx}{\cos k(L-s)/2}\right]}{\dfrac{s\omega_{p-}^2(\omega - j\nu_i) + [s\omega_{p+}^2 - [\omega(\omega - j\nu_i)]\,(\omega - j\nu_e)}{\omega(\omega - j\nu_i)} - \dfrac{2}{k}\,\dfrac{(\omega - j\nu_i)\omega_{p-}^2}{(\omega_{p+}^2 - \omega^2 + j\omega\nu_i)}\tan\dfrac{k(L-s)}{2}} \tag{3.61}$$

$$E_o = \frac{-\left[(\omega - j\nu_e)(\omega^2 - \omega_{p+}^2 - j\omega\nu_i) - \omega_{p-}^2(\omega - j\nu_i)\right]V(t)}{s\omega_{p-}^2[\omega - j\nu_i) + [s\omega_{p+}^2 - L\omega(\omega - j\nu_i)]\,(\omega - j\nu_e) - \dfrac{2}{k}\,\dfrac{(\omega - j\nu_i)^2\omega_{p-}^2\omega}{(\omega_{p+}^2 - \omega^2 + j\omega\nu_i)}\tan\dfrac{k(L-s)}{2}} \tag{3.62}$$

(A) The variation of electric field as a function of plasma density.

The electric fields at the center (x=0) of the plasma capacitor are calculated as a function of ω_{p+}/ω for the following fixed parameters: $L = 1.6$ mm, $s = .6$ mm, $\omega/U_e = 25$, $\nu_e/\omega = .1$ and $\nu_i/\omega = 0.001$. Figure 3.8 shows the variation of the normalized electric fields versus ω_{p+}/ω. The results obtained from this study are discussed below.

(1) At low frequency, there exists a series of discrete resonances for $\omega < \omega_{p+}$. The spacing between these resonances increase

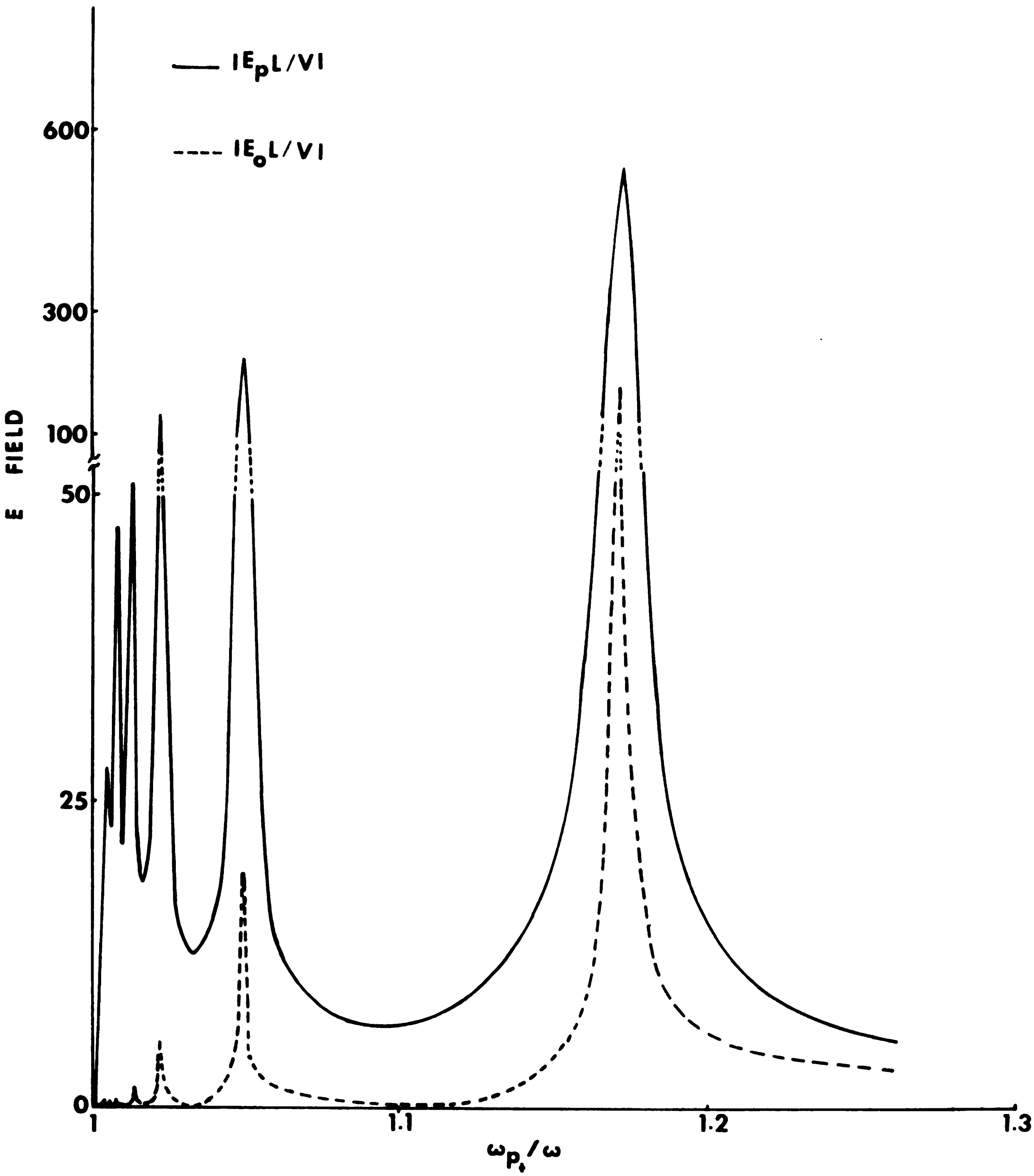

Figure 3.8 Normalized amplitude of the low frequency electric fields, $|LE_o/V|$ and $|LE_o/V|$, vs. ω_{p+}/ω ($L = 1.6$ mm, $s = .6$ mm, $\omega/U_e = 25$, $x = 0$, $\nu_-/\omega = .1$, $\nu_+/\omega = .001$)

with the increase of ω_{p+}/ω. As a result, a higher concentration of closely spaced resonances are found near $\omega_{p+}/\omega = 1$. The explanation to this phenomenon is provided by the v_{ph} vs. ω diagram. At a frequency near the ion plasma frequency, a cluster of resonances is resulted since a small change in density causes a big change in wavelength. However, at low frequency, there is only a small change in wavelength, or no change at all, for a big change in density. Thus, the separation between adjacent resonances becomes larger.

(2) At resonance the electric field in the sheath, E_o, and the electric field in the plasma, E_p, are much larger than the electric field in an empty capacitor.

(3) The number of discrete resonances at low frequency also depends strongly on the electron temperature, T_e. Resonances can occur at higher densities for a smaller electron temperature. Thus, decreasing the electron temperature increases the number of resonances in a collisional, warm plasma.

To illustrate, by keeping ω constant while increasing ω/U_e from 25 to 50, the number of plasma resonances increases from six to ten. The temperature effects can be explained with the dispersion relation (3.26). If the ion collisions are neglected at low frequency ($\omega << \omega_{p+} << \omega_{p-}$), equation (3.26) reduces to

$$k = \frac{\omega \omega_{p-}}{U_e \omega_{p+}}$$

The phase velocity of the plasma wave at low-frequency is then directly proportional to the electron temperature. That is

$$\frac{\omega}{k} = \frac{K T_e}{m_i}$$

For a constant ω, decreasing the electron temperature, T_e, results in a corresponding decrease in the wavelength. Thus, higher resonance states are allowed to exist in the plasma.

(B) The variation of electric field as a function of position .

The spatial variation of the real parts of the electric fields for the first three resonances are shown in Figure 3.9. The real part of the field is calculated with a time phase which maximizes the amplitudes. Clearly, all the resonances result from standing acoustic wave propagations for $\omega < \omega_{p+}$. The electric field in the sheath and in the plasma are discontinuous at the plasma-sheath interface as a result of charge accumulation. This change layer can be determined from the boundary condition

$$\vec{n} \cdot (\vec{D}_o - \vec{D}_p) = \rho_s$$

or

$$\epsilon_o (E_o - E_p) = \rho_s$$

Using equation (3.53) and (3.54), the surface charge induced on the surface of the plasma-sheath interface is of the form

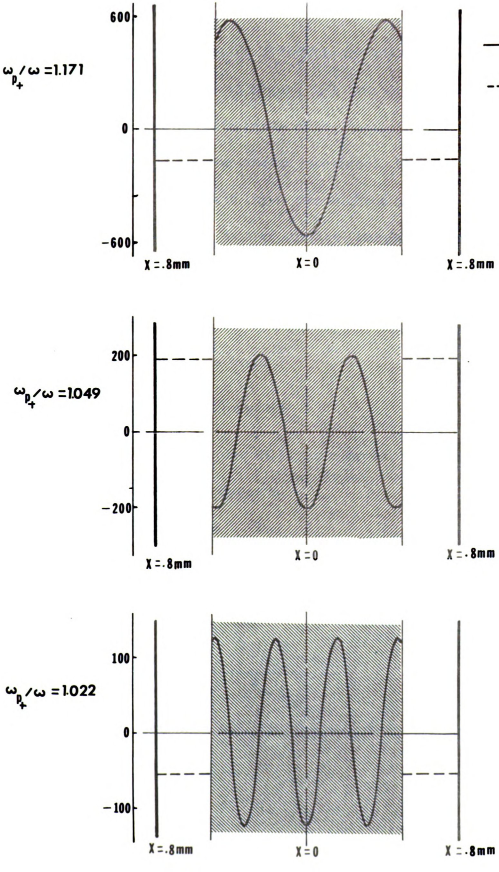

Figure 3.9 Real part of the normalized low frequency plasma field, LE_p/V, vs. position, x, at resonance (L = 1.6 mm, s = .6 mm, $\omega/U_e = 25$, $\nu_-/\omega = .1$, $\nu_+/\omega = .001$)

$$\rho_s = -\frac{\omega_{p+}^2 \epsilon_o E_p}{\omega^2 - j\omega\nu_i} \quad \text{at } x = \pm(L-s)/2$$

where E_p is the electric field in the plasma given by equation (3.61). As shown in Figure 3.9, the surface charge, ρ_s, is proportional to the difference of the normalized electric field amplitudes at the plasma-sheath interface. Note that since the electric field is a function of time, the surface charge is also a function of time. That is ρ_s is a rf surface charge density.

(C) Impedance and equivalent circuit ($\omega < \omega_{p+}$)

According to equation (3.41), the impedance of the plasma capacitor is of the form

$$Z = V(t)/j\omega\epsilon_o S E_o$$

If a collisionless plasma is considered, the electric field, E_o, of equation (3.62) reduces to

$$E_o = \frac{-(\omega^2 - \omega_{p+}^2 - \omega_{p-}^2)(\omega_{p+}^2 - \omega^2)V(t)}{[s(\omega_{p-}^2 + \omega_{p+}^2) - L\omega^2](\omega_{p+}^2 - \omega^2) - \frac{2}{k}\omega^2\omega_{p-}^2 \tan\frac{k(L-s)}{2}} \tag{3.63}$$

where

$$k = \frac{\omega}{U_e}\left(\frac{\omega^2 - \omega_{p+}^2 - \omega_{p-}^2}{\omega^2 - \omega_{p+}^2}\right)^{1/2}$$

From equation (3.63), the impedance, Z, becomes

$$Z = -\frac{1}{j\omega C}\;\frac{(\omega_{p-}^2+\omega_{p+}^2-\frac{L}{s}\,\omega^2)(\omega_{p+}^2-\omega^2)-\frac{2}{ks}\,\omega_{p-}^2\omega^2\tan\frac{k(L-s)}{2}}{(\omega^2-\omega_{p+}^2-\omega_{p-}^2)(\omega_{p+}^2-\omega^2)} \tag{3.64}$$

At low frequency, the ion plasma frequency ω_{p+}, and hence ω, are generally much smaller than the electron plasma frequency ω_{p-}. Therefore, equation (3.64) can be written as

$$Z = \frac{1}{j\omega C}\left(1-\frac{m_e}{m_i}\,\frac{(L/s-1)\omega^2}{\omega_{p+}^2}-\frac{2}{ks}\,\frac{\tan k(L-s)/2}{\omega_{p+}^2/\omega^2-1}\right) \tag{3.65}$$

where

$$k = \frac{\omega}{U_e}\left(\frac{m_i}{m_e}\right)^{1/2}\left(1-\frac{\omega^2}{\omega_{p+}^2}\right)^{-1/2} \tag{3.66}$$

Similar to the high-frequency case, equation (3.65) can be represented by the following equivalent circuit

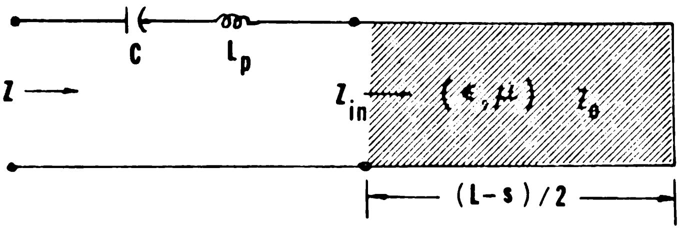

where

$$L_p = \frac{m_e}{m_i}\,\frac{(L/s-1)}{C\,\omega_{p+}^2}$$

In view of equation (3.65), the input impedance to the transmission line is of the form

$$Z_{in} = j\,\frac{2}{Cs}\,\frac{U_e}{\omega_{p+}^2}\left(\frac{m_e}{m_i}\right)^{1/2}\frac{\tan k(L-s)/2}{(1-\omega^2/\omega_{p+}^2)^{1/2}} \tag{3.67}$$

Also, from the transmission line theory,

$$Z_{in} = j Z_o \tan \frac{k(L-s)}{2}$$

where the characteristic impedance, Z_o, and the propagation constant, k, are given by

$$Z_o = (Z'/Y')^{1/2}$$

$$jk = (Z'Y')^{1/2}$$

If the series impedance per unit length of the line, Z', and the shunt admittance are chosen as

$$Z' = j\omega\mu$$

$$Y' = \left(\frac{j\omega}{\epsilon} + \frac{\omega_{p+}^2}{j\omega\epsilon} \right)^{-1}$$

The characteristic impedance, Z_o, and the propagation constant, k, then have the form

$$k = \frac{\omega}{\omega_{p+}} (\mu\epsilon)^{1/2} \left(1 - \frac{\omega^2}{\omega_{p+}^2}\right)^{-1/2} \tag{3.68}$$

$$Z_o = \omega_{p+} \left(\frac{\mu}{\epsilon}\right)^{1/2} \left(1 - \frac{\omega^2}{\omega_{p+}^2}\right)^{1/2} \tag{3.69}$$

Consequently, it follows from equations (3.66) to (3.69) that

$$\mu\epsilon = \left(\frac{\omega_{p+}}{U_e}\right)^2 \frac{m_i}{m_e}$$

$$\epsilon = \frac{\omega_{p+}^2}{U_e^2} \frac{sC}{2} \frac{m_i}{m_e} (\omega_{p+}^2 - \omega^2)$$

$$\mu = \frac{2}{sC}\left(\omega_{p+}^2 - \omega^2\right)^{-1}$$

On the basis of the above information, the following equivalent circuit can be drawn for the shorted transmission line.

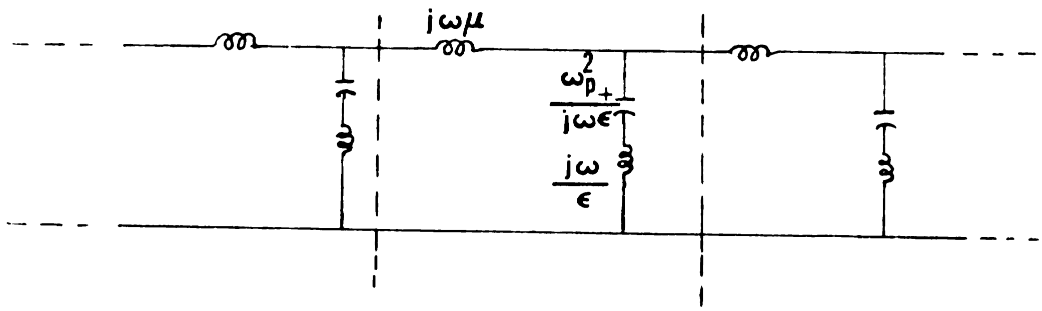

Since $\omega < \omega_{p+}$ is assumed, the propagation constant, k, is always positive real. At resonance (Z=0), equation (3.65) is simplified to

$$\frac{sk}{2\left(k^2 \frac{m_e}{m_i} \frac{U_e^2}{\omega^2} - 1\right)} - \frac{\omega^2}{U_e^2} \frac{(L-s)}{2k} = \tan \frac{k(L-s)}{2} \qquad (3.70)$$

The resonance condition can be obtained from graphical solution of equation (3.70). Figure 3.10 shows the graphical solution of the first three resonances in the high plasma density region corresponding to the case plotted in Figure 3.8. Note that the first resonance can be a half wavelength or a whole wavelength depending on the value of ω/U_e ratio. For a large ω/U_e ratio, only the high order of resonance can be excited.

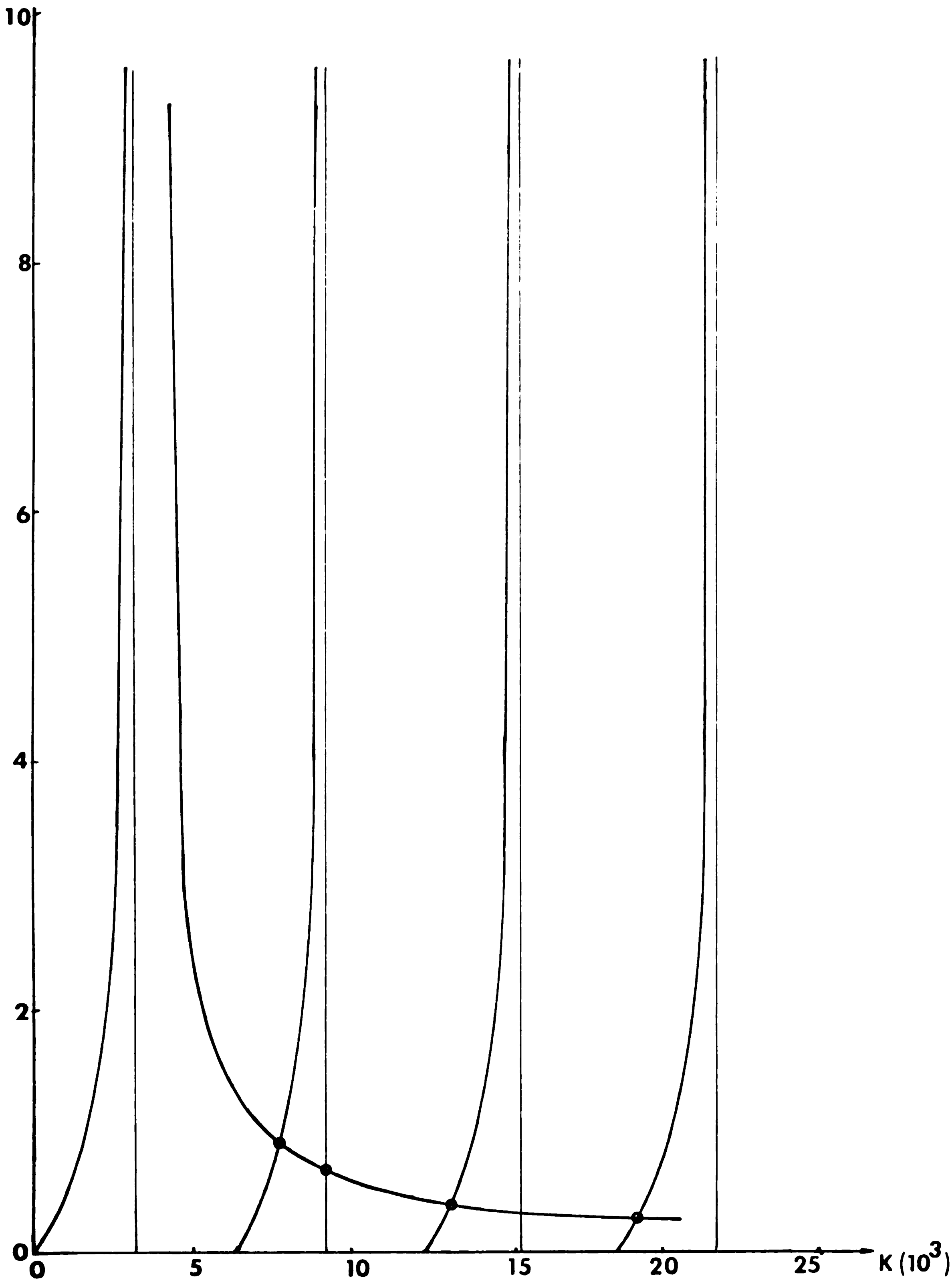

Figure 3.10 Graphical solution of low frequency capacitor impedance ($L = 1.6$ mm, $s = .6$ mm, $\omega/U_e = 25$)

CHAPTER 4

EXPERIMENTAL SYSTEMS

4.1 Introduction

Nonlinear resonance effects at higher power have been investigated with two different experimental systems: namely, the coaxial type system and the ridge waveguide system. In the coaxial type system, the plasma is created in a small break (> 1.6 mm) in the inner conductor by a high-frequency electric field of 3.036 Hz. The nonlinear resonance effect at both the fundamental and the third harmonic frequencies have been analyzed. One unique feature of this system is its ability to vary the plasma parameters: The input power, the gap length and the pressure in the system can be adjusted independently for various resonance states. Furthermore, a small microwave signal or a dc bias can be externally applied to the system to study the sheath and parametric amplification effects. Although only dry air was used, different gases, such as A, K_r and X_e, can be introduced into the system. A picture of this system is shown in Figure 4.1.

The structurally simpler ridge waveguide system is similar to an experimental system that has been used by other investigators.

(a)

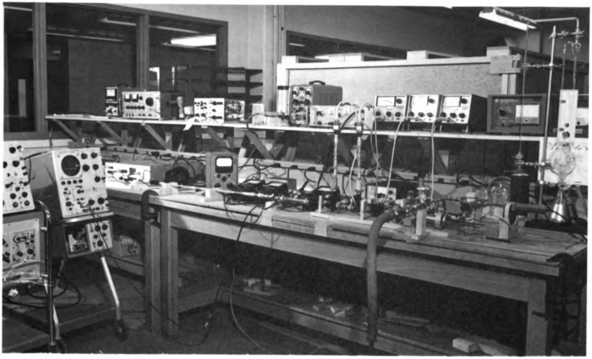

(b)

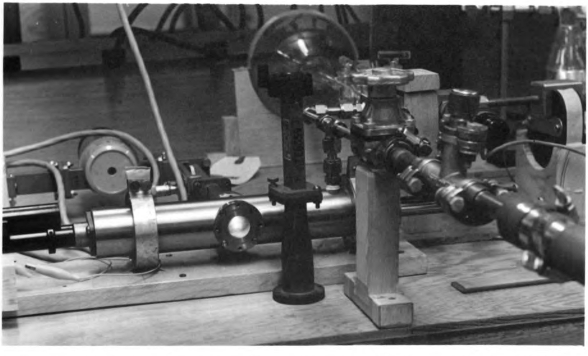

Figure 4.1 Experimental system: (a) overall view of the coaxial system; (b) close view of the coaxial discharge structure.

This system consists of a positive column of a mercury vapor discharge which is inserted across a rectangular ridge waveguide perpendicular to an externally applied electric field. Either a dc or a resonantly sustained high-frequency discharge can be created. In fact a combination of the two types of discharges can occur simultaneously producing a dense plasma in the ridge waveguide system.

In the following, the structural design and the assembly of microwave equipment pertaining to the two plasma systems described above will be discussed.

4.2 Coaxial type system

A block diagram of experimental apparatus for the coaxial type system is shown in Figure 4.2. The system can be considered as a combination of three sub-system; namely, the microwave system, the plasma-vacuum system and the detecting system. Each of these sub-systems is discussed separately below.

(A) The microwave system.

The microwave signal of frequency 3.03 GHz is provided by an external cavity klystron oscillator (2K28) which is connected to a HP 2650A oscillator synchronizer to form a phase-lock loop. The synchronizer phase locks the klystron oscillator to a harmonic of an internal spectrally pure crystal oscillator to produce a frequency stable, microwave souce. A frequency stable source is important here, because the plasma medium is generally dispersive in nature, and the microwave circuits used are frequency sensitive.

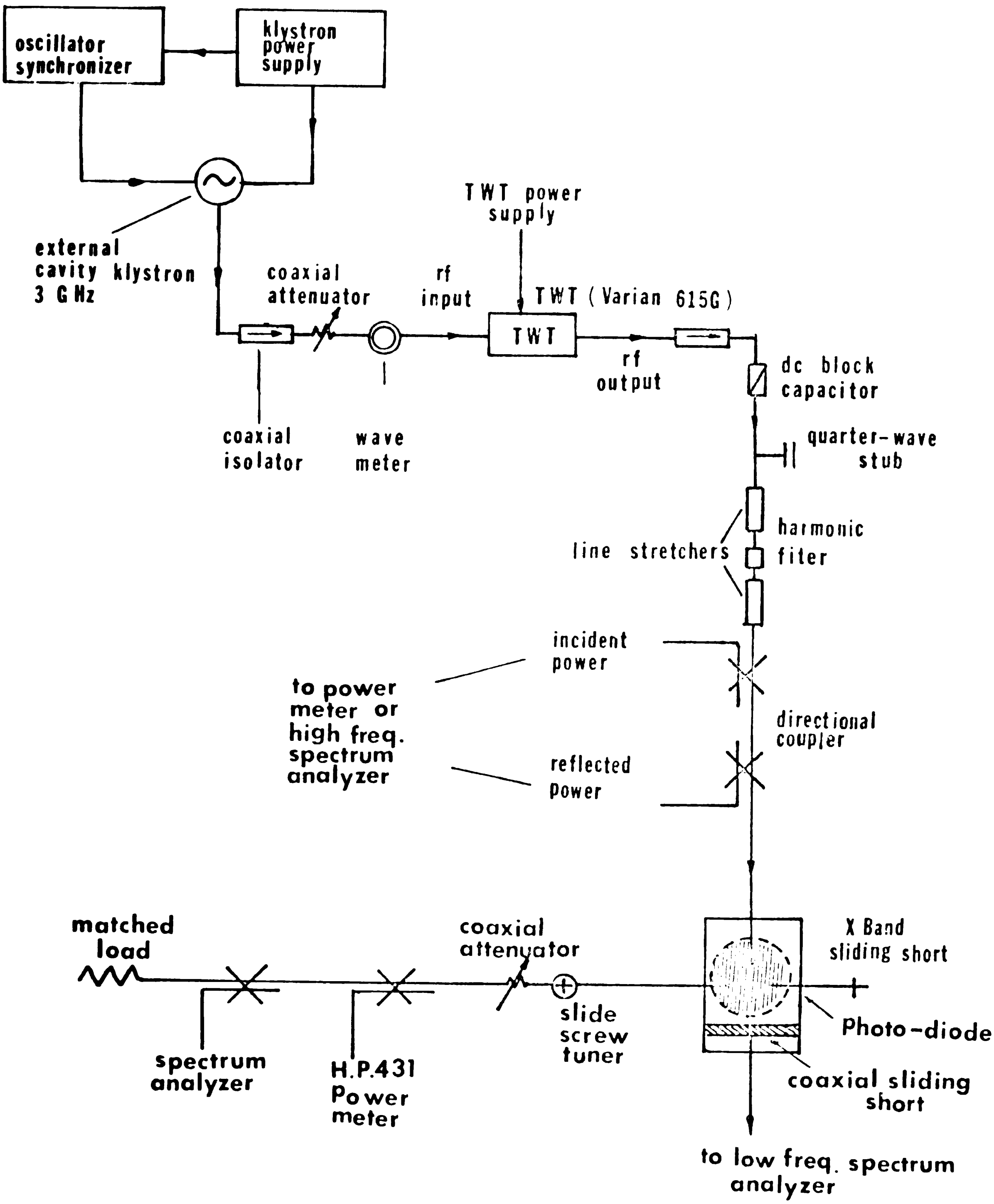

Figure 4.2 Experimental apparatus block diagram for the coaxial system.

As shown in Figure 4.2, the frequency stable microwave power is fed into an isolator. The principle function of the isolator is to block the reflected microwave power from returning to the stabilized klystron source. A short tuning stub may be inserted to match the system for maximum power transfer. Under matched conditions, the maximum attainable power from the klystron source is approximately 6 mw. This stabilized microwave power is then delivered to a variable attenuator which regulates the input power to a Varian 615 G traveling wave tube amplifier (TWT). By adjusting the variable attenuator, the amplified output power from the TWT can vary from 0 to 25 watts. The output helix of the TWT is protected from being damaged by the reflected microwave power with another isolator.

Harmonic power can be generated by the klystron source as well as the TWT whenever they are over-driven. When analyzing the output spectrum of nonlinear plasma-microwave interactions, the harmonics generated by other than the plasma are generally undesirable. To minimize the transfer of the source harmonic power to the plasma-vacuum system, a low-pass Microlab LA-40N filter is placed between two line stretchers which provide translational freedom for the low-pass filter without alterating the length of the coaxial line. A proper adjustment of the line stretchers resonates the third harmonic power in the coaxial line, as well as reducing the third harmonic power entering the plasma-vacuum system.

In general, only part of the microwave power delivered to the plasma-vacuum system is absorbed by the plasma, while the rest is reflected back to the microwave source. Directional couplers were used to sense the incident and reflected power in the system. Also, in the study of parametric amplification in a resonantly sustained plasma, a directional coupler was used to couple an externally applied signal to the high-frequency discharge.

As shown in Figure 4.2, the third harmonic power generated by plasma nonlinearities was coupled out from the coaxial discharge structure with a x-band waveguide system. By adjusting the x-band sliding short and the slide screw tuner for best match, a significant amount of the third harmonic power can be coupled to the x-band load.

(B) The plasma-vacuum system

The cross section of the coaxial device used in this experiment is shown in Figure 4.3. The discharge structure is made of non-magnetic stainless steel which has a relatively low vapor pressure. A teflon insert which provides structural supports for the anode electrode is designed as a quarter-wave matching transformer. Thus, the input characteristic impedance of the coaxial system is matched to the plasma-vacuum system. In order to hold a high vacuum inside the discharge structure, 0-rings lightly coated with thin vacuum grease are placed around the teflon insert. Transparent mylar sheets are used to seal the waveguide windows. The use of

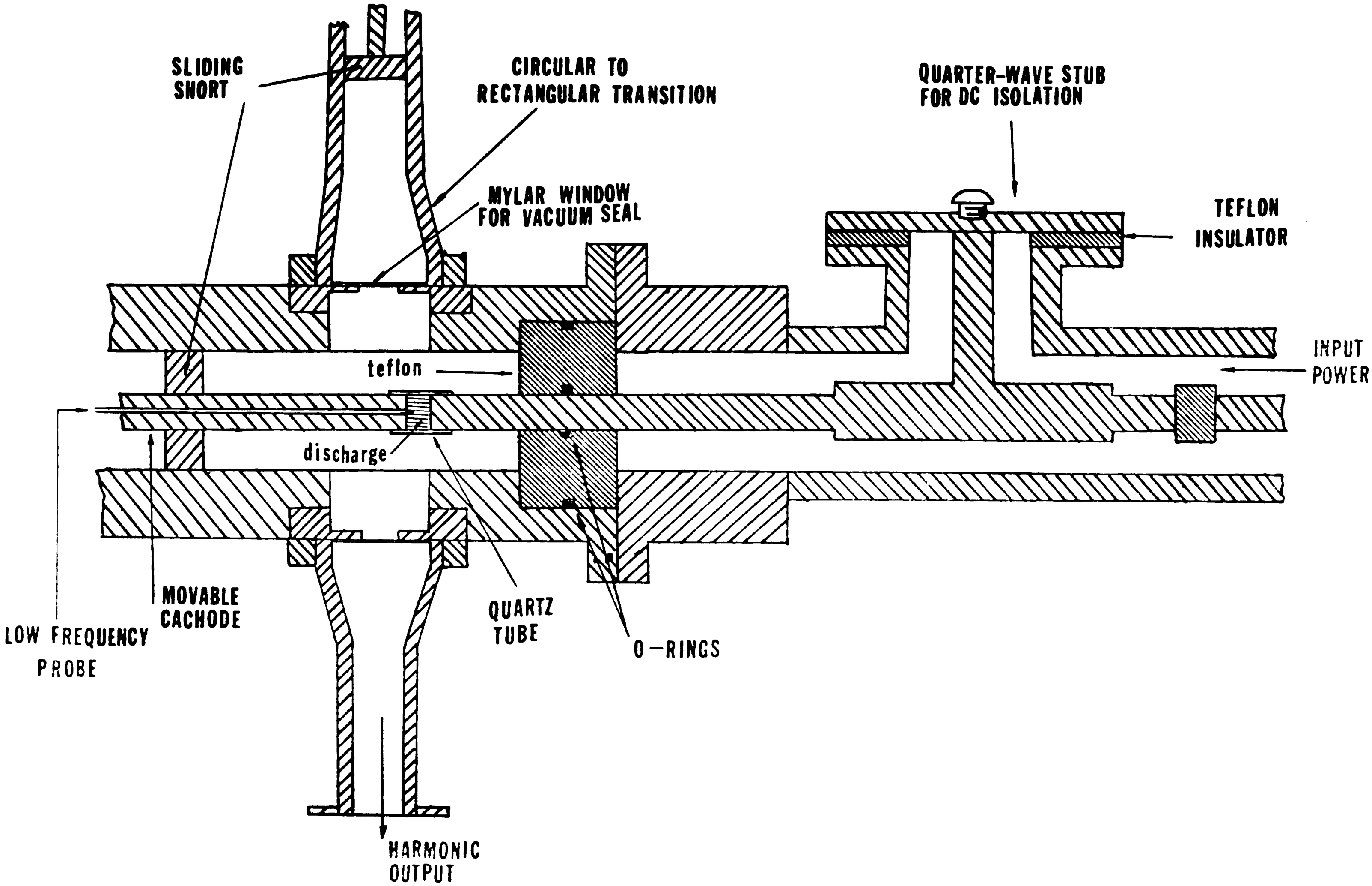

Figure 4.3 Cross section of the coaxial discharge structure.

mylar sheets not only permits the coupling of the third harmonic power to the x-band system, but also allows one to observe the discharge from outside.

The cylindrical interior of the coaxial vacuum device can be held at a reduced, variable pressure by means of high vacuum valves and a rotary mechanical pump. With the mechanical pump alone, the lowest attainable pressure in the system is about 10 microns. Further decrease in pressure requires the use of a Vac-Ion pump which operates efficiently only with a low, initial pressure. When using the Vac-Ion pump, the pressure in the system can be reduced to the order of 10^{-5} torr (mm Hg). A thermocouple vacuum gauge and a calibrated Mcloed gauge are used to read the pressure in the system. Pressure readings are taken after the system reaches an equilibrium state. The accuracy of the experimental results depends strongly on how well the system can hold its vacuum. This is particularly true when experimenting with pure gas.

As shown in Figure 4.4, the reflection of the high-frequency input power at the coaxial sliding short sets up a standing wave inside the coaxial discharge structure. Any variation of the position of the coaxial sliding short will cause a corresponding translation of the standing wave. To produce a breakdown, a microwave power of about 20 watts at 3.03 GHz is applied to the system. The pressure in the system is adjusted to approximately the breakdown value which depends on the gas. In the case of air, the breakdown pressure

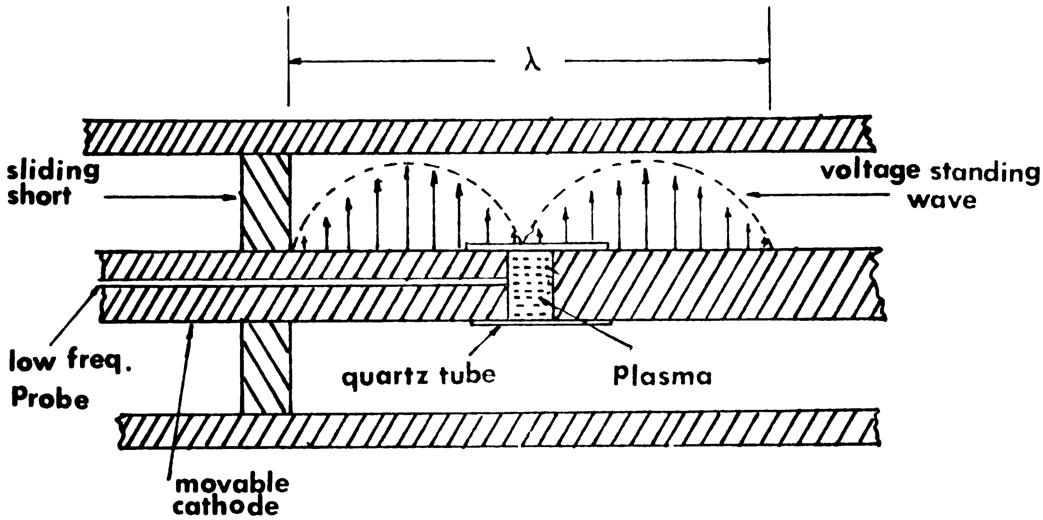

Figure 4.4 Voltage standing wave pattern for breakdown by high E field.

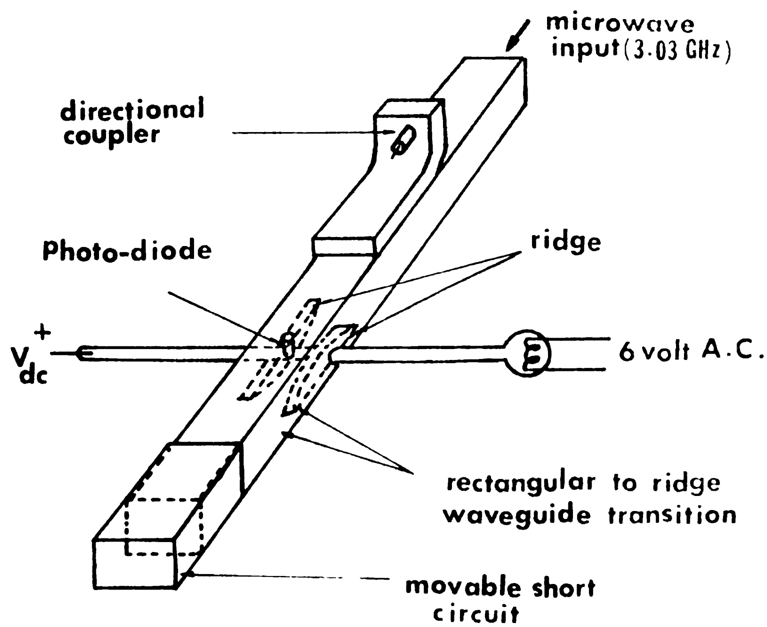

Figure 4.5 Ridge waveguide system.

varies from 2-4 mm Hg. With the inner conductors shorted together, the current maximum is located at the conductor break. Then, the movable electrode is pulled out slowly to form a gap of length 1.5 mm. The high electric field in the gap breaks down the gas in creating a plasma. The physical mechanisms involved in the high-frequency breakdown are well known.[49] Clearly, the high-frequency breakdown depends not only on the input power, gas type and pressure in the system, but also on the gap length and the position of the sliding short.

The gap length can be varied by adjusting the movable electrode which is connected to the grounded, external shell of the coaxial discharge structure. A dial micrometer indicator which is fastened to the movable electrode provides precise, continuous measurements of the gap lengths. Since the gap length is much smaller than the electromagnetic wavelength, the coaxial structure can be approximated as a plasma-filled capacitor.

In the low pressure, high field regime, the plasma originally located inside the coaxial conductor gap is ejected to a position between the inner and outer conductors. In order to keep the plasma confined to the gap at all pressures, a quartz tube is placed around the center conductor at the gap as shown in Figure 4-3. The size of the tube has an important effect on the output of the third harmonic power.[34] To detect the low-frequency ion oscillations in the plasma, a thin wire probe is inserted into the plasma through the hollow cathode electrode as shown in Figure 4-3. Whenever a parametric instability occurs in the plasma, strong low-frequency ion oscillation at f_i and $2f_i$ have been detected through a low-pass filter with a Tektronix 3L10 spectrum a analyzer.

As shown in Figure 4.3, a dc bias can be applied externally across the conductor gap through a quarter-wave stub. To provide dc isolation of the coaxial center conductor, the end plate of the quarter-wave stub is isolated from the grounded, outer conductor by a ring of teflon. The width of the teflon ring is chosen according to the radial waveguide theory, so that at the inner radius, the teflon surface behaves electrically like a short circuit. To prevent the plasma from being shorted out, a dc belocking capacitor is inserted between the quarter-wave stub and the line stretchers. With no dc bias applied to the system, the dc voltage induced across the conductor gap by the resonantly sustained discharge can be measured by connecting a digital voltmeter to the quarter-wave stub. Also, the low-frequency ion oscillations can be sensed through the quarter-wave stub with a Tektronix oscilloscope.

(C) The detecting system.

The Tektronix 1L40 spectrum analyzer and the HP 431C power meter were used to sense the incident and reflected microwave power through directional couplers at 3.03 GHz as well as the third harmonic power at 9.09 GHz. The display of the relative power as a function of frequency on the spectrum analyzer leads to the observations of parametric amplification, frequency shift and frequency modulation in the resonantly sustained high-frequency plasma. Care must be taken not to over-drive the spectrum analyzer. Otherwise, spurious response generated within the spectrum analyzer may produce an erroneous display of signal.

The average luminosity emitted from the plasma has been shown by others[4] to be proportional to the relative average plasma density $\langle N \rangle$. In this experiment, the average luminosity from the plasma was measured by recording the luminosity current in a simple dc photo-diode circuit. The photo-diode which was placed adjacent to the mylar window of the discharge structure senses the luminosity and the plasma volume changes.

Experimentally, a X-Y plotter was used to record the incident power, P_{in}, the absorbed power, P_{abs}, the third harmonic power, P_{srd}, and the rectified dc voltage across the gap versus the relative average plasma density $\langle N \rangle$. The voltage input to the X-Y plotter was taken directly from the dc calibration jack of the power meter. These recordings display the hysteresis phenomena in plasma.

4.3 The ridge waveguide system.

A block diagram of the ridge waveguide system is shown in Figure 4.5. Clearly, the basic difference between the coaxial type system and the ridge-waveguide system lies in the geometry of the discharge structure and how the plasma is created. In the former case, the plasma is created and maintained solely by the microwave power in a small conductor gap; whereas in the latter case, the plasma is created and maintained by either dc or microwave power in a cylindrical plasma column. This column is inserted across a ridge waveguide perpendicular to an applied high-frequency field. A similar system, without the ridge in the waveguide, has been commonly used by others to investigate the linear T-D resonances exhibited in the microwave scattering at low power[17], and recently the nonlinear resonance effects of a resonantly sustained plasma at higher power[2,4].

After the plasma is created with a dc voltage, a high-frequency electric field can be applied to the s-band ridge waveguide system. For sufficiently high microwave power, the plasma can be sustained by microwave energy even if the dc voltage is removed. The same microwave system (klystron, TWT, etc.) described above provides the necessary microwave power.

Structurally, rectangular ridges are fastened along the center of the top and bottom waveguide walls. In order to produce a gradual discontinuity at the joint between the ridge and the waveguide wall, the ridge are tapered. The perturbation of the ridge lowers the cutoff frequency of the dominant mode, but raises the cutoff frequency of the next higher mode. As a result, the introduction of the ridge into the waveguide causes a greater separation between single-mode operation[50]. Furthermore, the ridge are used here to concentrate a strong high-frequency electric field across the narrow gap where the plasma column is located. Hence, a more efficient use of microwave power is possible.

Since the ridge waveguide is terminated in a movable short circuit, the standing wave inside the waveguide can be translated to a position where the maximum electric field strength falls directly on the plasma column.

As shown in Figure 4.5, a photo-diode is inserted into a small hole (diameter = 2mm) through the ridge on the top waveguide wall in order to measure the average luminosity emitted from the plasma. Unlike the coaxial case where the diode is placed relatively far away from the small plasma gap, this diode is embedded in a tiny hold measuring only the density of a small fraction of the plasma. That is, it sees only a small portion of the plasma, and thus does not sense plasma volume changes. With this experimental set-up, the luminosity of a resonantly sustained plasma which is proportional to the luminosity current, I_ℓ, can be directly related to the average plasma density. This was done by measuring the luminosity current, I_ℓ, and the corresponding electron plasma density, n_e, in a dc discharge. The electron plasma density was determined by the cavity perturbation method with a cylindrical cavity placed adjacent to the ridge waveguide. By varying the dc discharge current, a curve of n_e versus I_ℓ was drawn. As shown in Figure 4-6, the electron plasma density, n_e, increases with the increase of luminosity current. The

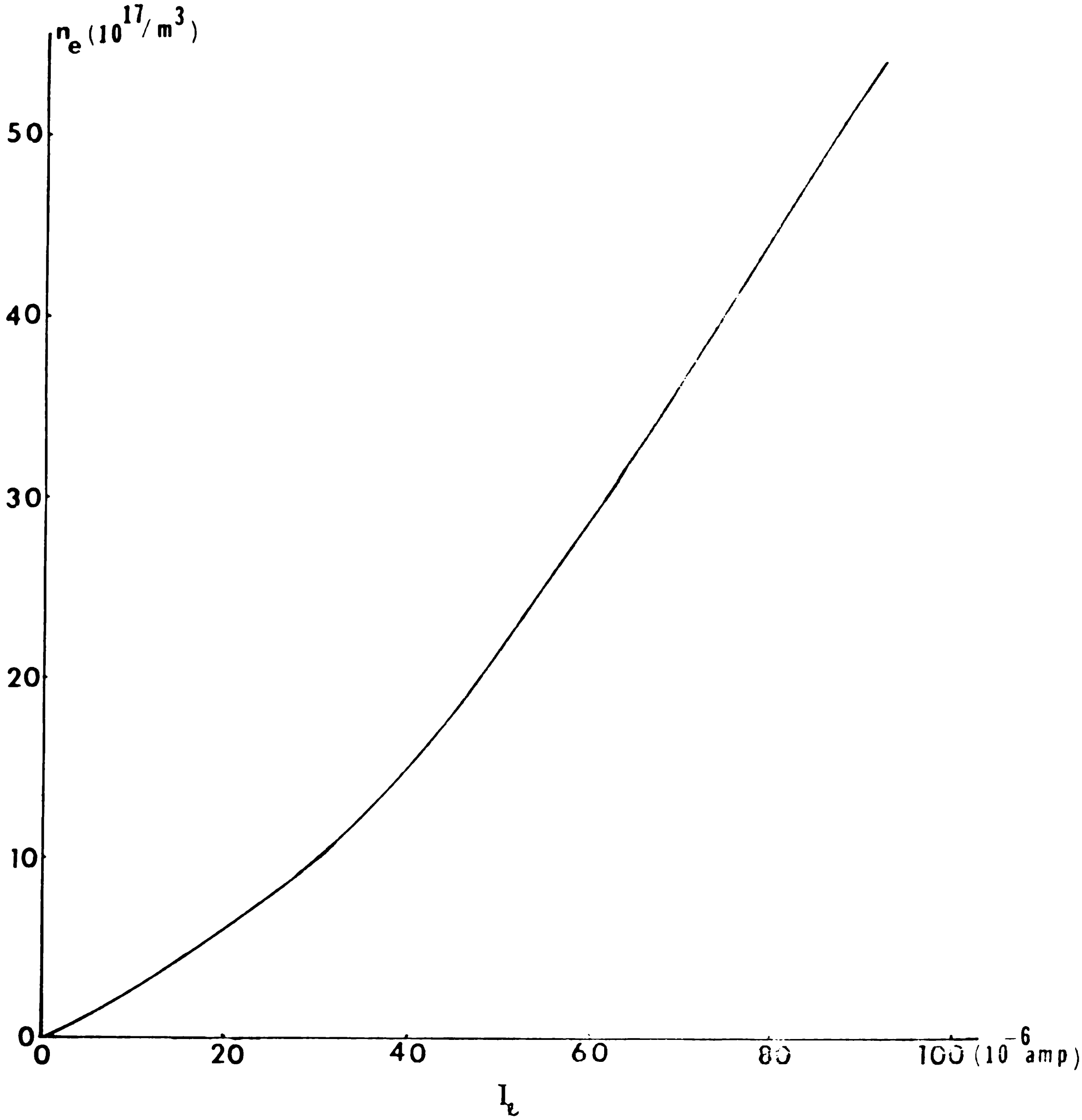

Figure 4.6 Luminosity vs. plasma density.

nonlinear characteristics of the photo-diode attribute to the nonlinear relation between n_e and I_ℓ. A Tektronix 1L40 spectrum analyzer was used to display the reflected power through a directional coupler. Also, by sweeping the dc discharge current, the temperature and cold plasma resonances at high and low powers were observed with a Tektronix oscilloscope through a crystal detector.

CHAPTER 5

EXPERIMENTAL RESULTS

The nonlinear resonance effects to be reported here arise from two different types of discharge: a dc discharge and a resonance-sustained high frequency discharge. The nonlinear phenomena for the temperature and cold plasma resonances were observed in the microwave scattering from a dc plasma column which was irradiated by a high power microwave signal. Such a study leads to the physical understanding of the more complex non-linear phenomena of a resonance-sustained high frequency plasma which is created and maintained entirely by microwave power. In the following discussion, the nonlinear resonance effects of the high frequency discharge, including parametric amplification, frequency shift, frequency modulation, rectification and hysteresis phenomenon, are described separately. The physical interpretation of the experimental results are also considered.

5.1 Nonlinear effects of the temperature resonances at high power: the transition from a dc sustained to a rf resonantly sustained plasma

When a low power microwave signal (< 50 mw) is incident on a bounded plasma, a series of linear temperature (Tonks-Dattner) resonances can be observed as the plasma density is varied. If the incident microwave power is increased, the linear resonances become "distorted," and finally when the rf power is sufficiently high, the plasma becomes completely sustained by the rf power; i.e., it becomes what is commonly called a resonantly sustained plasma. The experimental observation of the transition from low rf power, linear resonances to the completely resonantly sustained plasma is presented here. Using these observations, a qualitative theory is developed which explains the behavior of the plasma microwave system.

These nonlinear resonance effects were studied experimentally with the ridge waveguide system which is discussed in Chapter 4 and shown in Figure 4.4. Instead of the usual matched load termination, this waveguide system is terminated in a sliding short. The position of the sliding short is adjusted so that the waveguide impedance at the plasma is zero (i.e., open circuit). Thus, maximum electric field strength impinges upon the dc discharge column located between the ridges. The incident microwave power in the waveguide system is partly absorbed by the dc plasma, while the rest is reflected. The power absorbed by the plasma is then equal to the difference of the incident and reflected power; that is

$$p_{abs} = p_{in} - p_{ref}$$

In this microwave system p_{in} = constant for each experimental observation. Thus the resonances are observed as "dip" in reflected power as the dc discharge current is varied[17]. Typical experimental results are shown in the oscilloscope pictures of Figures 5.1(a) to (e) in which the plasma luminosity (top curve) and the relative reflected power (bottom curve) correspond to the ordinate, and the dc discharge current corresponds to the abscissa. The horizontal center line is the zero reference with the luminosity increasing upward and the reflected power increasing downward. As mentioned in Chapter 4, the luminosity is proportional to the relative plasma density.

At low microwave power, the usual linear temperature resonances are observed. These are displayed in Figure 5.1(a). The dip in the trace indicates that the microwave power is absorbed at resonance. Note that at this low incident power, the resonance is critically coupled to the waveguide system. As the incident power is increased, Figures 5.1(b) to (e) show that the temperature resonances, which appear in the reflected power, are distorted. The luminosity levels off and decreases slightly when the plasma is in resonance. This indicates that when the microwave power is absorbed by the plasma, this energy ionizes the plasma and tends

$p_{in} \cong$ 25 mw

scale cal.

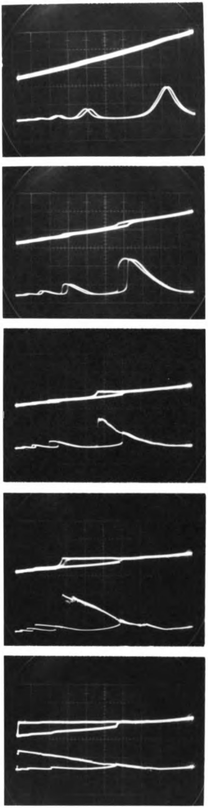

(a) (.05v/cm) (.05v/cm)

(b) (.1v/cm) (.1v/cm)

(c) (.1v/cm) (.2v/cm)

(d) (.1v/cm) (.2v/cm)

(e) (.1v/cm) (.5v/cm)

$p_{in} \cong$ 5 watts

Figure 5.1 Nonlinear effects of the Tonks-Dattner resonances: (i) luminosity vs. dc discharge current, and (ii) reflected power vs. dc discharge current.

to keep the plasma density approximately constant. In Figure 5.1(e), the luminosity levels for a large variation in dc discharge current. In fact, $I_{dc} = 0$ when the plasma drops out of the resonant state. In this case, the incident power level is almost sufficient to sustain the plasma completely in a resonant state. Another important fact is that the coupling of microwave power into the plasma depends on the incident microwave power. At high microwave power, the main resonance is no longer critically coupled to the waveguide system. In order to understand the nonlinear behavior of the plasma, the physical behavior of the ridge waveguide system can be approximated by the plasma capacitor system of Figure 2.1. The equivalence of these two systems is illustrated in the diagrams below.

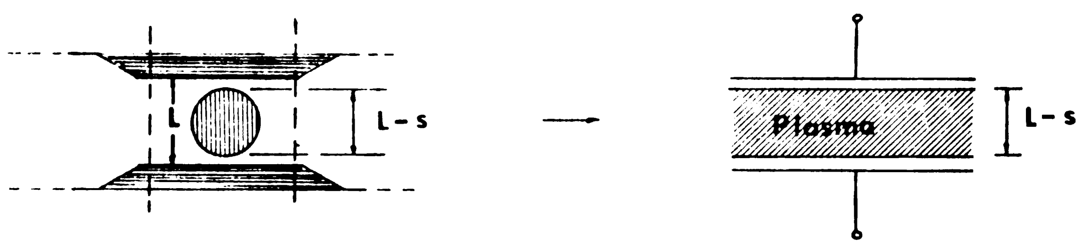

The waveguide system can be replaced by its equivalent transmission system; thus, the plasma capacitor is the load in such a waveguide transmission system as shown below.

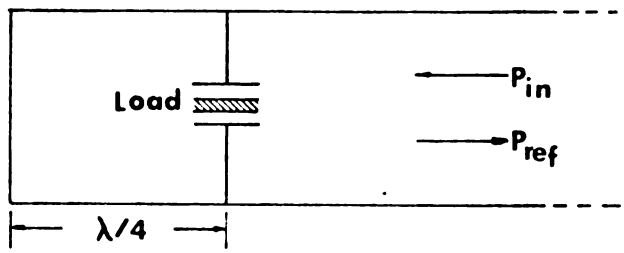

The load impedance of the plasma capacitor varies with the plasma density. Such a variation can be plotted on the Smith Chart. For illustration, the behavior of the main or cold plasma resonance (the largest resonance in Figure 5.1) is discussed. However, this concept applies to the temperature resonances as well. The capacitor admittance can be obtained from the boundary conditions given in Chapter 3. That is,

$$E_o = \epsilon_r E_p$$

$$V(t) = (s\epsilon_r - s + L)E_p$$

For the cold collisional plasma model, the relative equivalent permittivity, ϵ_r, is of the form

$$\epsilon_r = \left(1 - \frac{\omega_{p-}^2}{\omega^2 - \nu_-^2}\right) - j\frac{\nu_-}{\omega}\,\frac{\omega_{p-}^2}{\omega^2 - \nu_-^2}$$

Solving the above equation, the capacitor admittance can be written as

$$Y \quad j\omega C \; \frac{\omega^2 - \nu_-^2 - \omega_{p-}^2(1 + j\nu_-/\omega)}{L/s(\omega^2 - \nu_-^2) - \omega_{p-}^2(1 + j\nu_-/\omega)}$$

where C is the total capacitance of the vacuum sheath as indicated in Chapter 3.

The amplitude and phase of Y versus (ω_{p-}/ω) are plotted in Figure 5.2 for $s/L = .1$ and $\nu_-/\omega = .1$. Figure 5.3 shows the plot of the impedance Z, the reciprocal of Y, for different plasma densities on a Smith Chart. Note that the impedance curve is asymmetrical about the real axis because of collisional damping in plasma. For the convenience of illustration, a typical plot of the impedance Z for a constant sheath thickness, and various ω_{p-} is sketched below for $\nu_- \ll \omega$ (i.e, for small collisional loss).

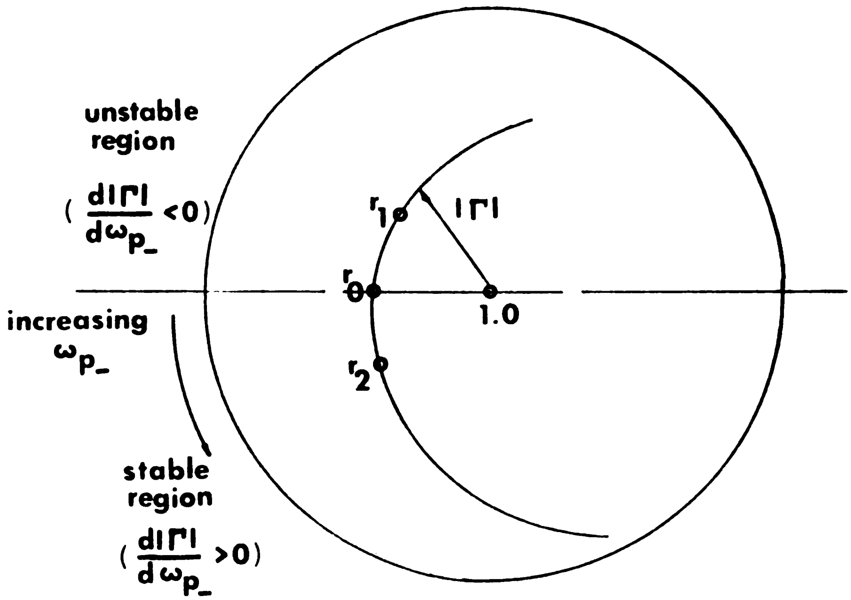

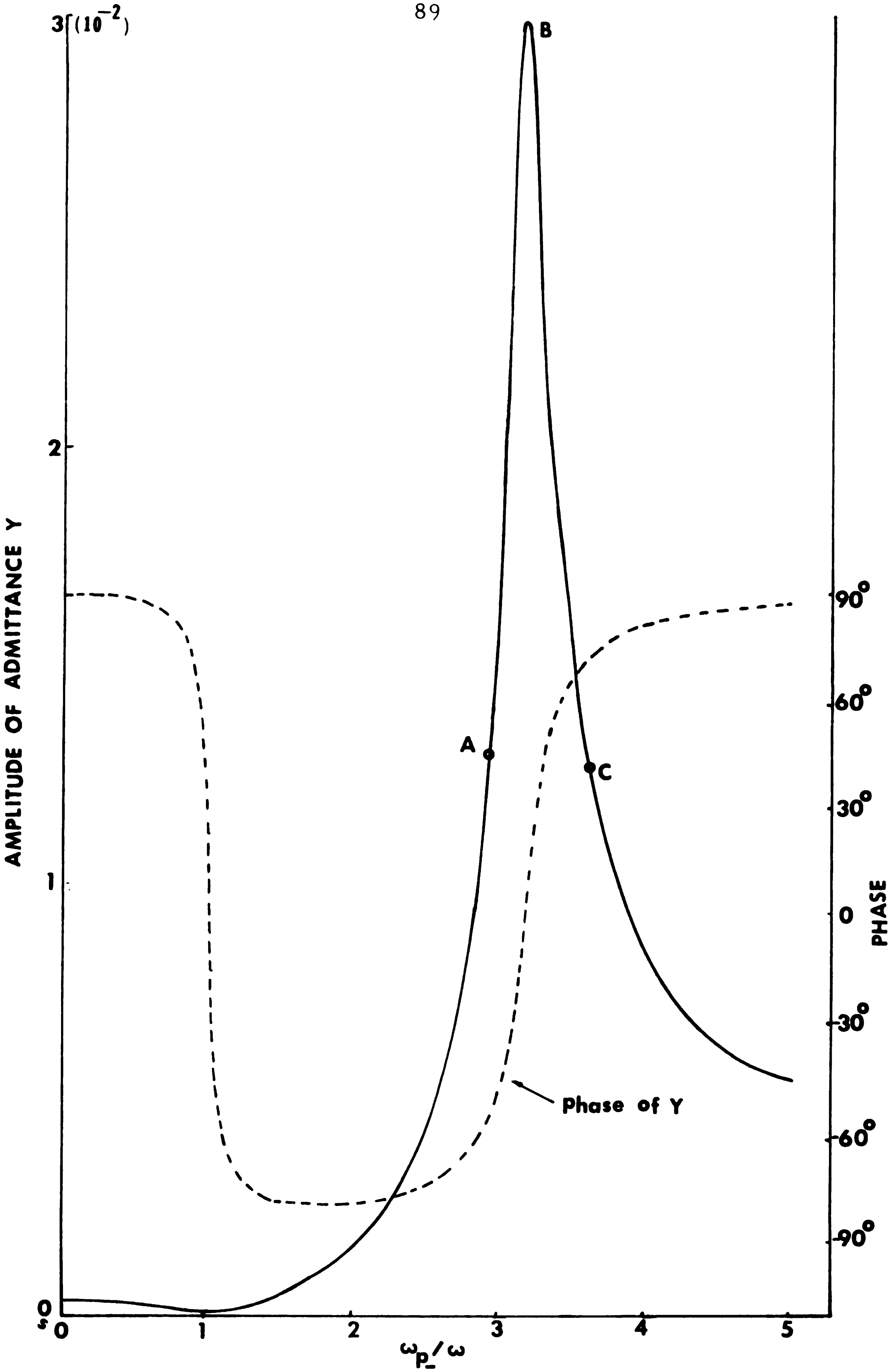

Figure 5.2 Admittance of a cold plasma capacitor model ($s/L = .1$, $\nu_e/\omega = .1$)

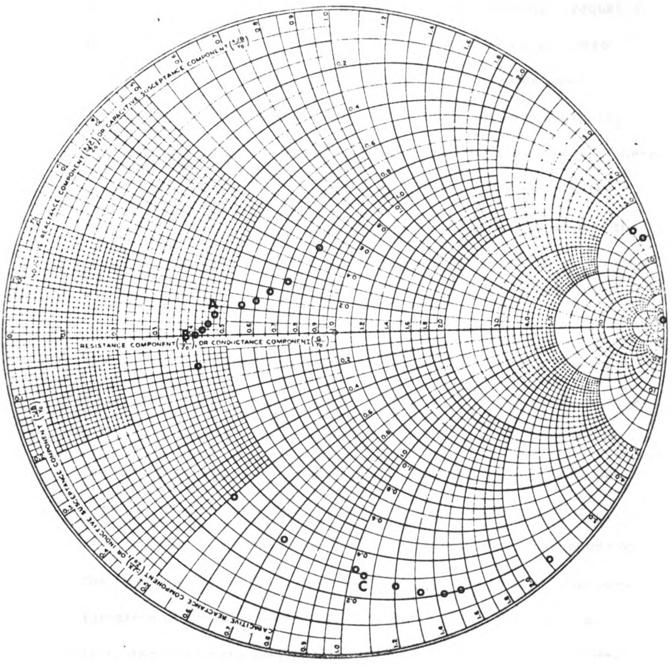

Figure 5. 3 Smith Chart representation of the cold plasma capacitor impedance ($s/L = .1$, $\nu_e/\omega = .1$)

The stability of an rf discharge can be developed from the Smith Chart impedance. A dc plasma is always stable; however, there exist stable and unstable regions when the plasma is partly or totally sustained by rf power. The stable region of a high frequency plasma corresponds to the portion of the resonance curve where increasing the plasma density decreases the microwave power absorbed by the plasma; whereas the unstable region corresponds to where increasing the density increases the absorbed power. These stable and unstable regions can be identified on the Smith Chart. Since the microwave power absorbed by the plasma is related to the incident power and the reflection coefficient $|\Gamma|$, through

$$p_{abs} = p_{in}(1 - |\Gamma|^2)$$

the stable region corresponds to the capacitive portion of the chart where $d|\Gamma|/d\omega_{p-} > 0$; that is, increasing the plasma density increases $|\Gamma|$, and hence decreases p_{abs}. The unstable region corresponds to the inductive portion of the chart where $d|\Gamma|/d\omega_{p-} < 0$. Thus, increasing the plasma density decreases, $|\Gamma|$, and increases p_{abs}.

As shown in the above sketch, the point, r_o, corresponds to the resonance peak where the plasma is pure resistance. Any perturbation in density tends to shift the plasma off resonance. In fact, decreasing the plasma density from r_o to r_1 results in a decrease in the absorbed power (or an increase in $|\Gamma|$). Thus, the plasma becomes unstable, and tends to jump to a lower resonance state. However, increasing the plasma density from r_o to r_2 decreases the power absorbed by the plasma. Such a decrease in absorbed power tends to pull the plasma back into a resonant state. It is to be emphasized that a large collisional damping has a stabilizing effect on the plasma. As shown in Figure 5.3, the plasma is stable in the inductive region near the real axis, because for a small region of inductive impedances decreasing the plasma density results in an increase in the absorbed power.

The absorbed power, p_{abs}, versus the average plasma density $< N >$, is plotted below in the vicinity of the main resonance for three different values of incident microwave power with $p_{in1} < p_{in2} < p_{in3}$. The phase of the impedance is also provided to correlate the stable and unstable regions on the resonance curves.

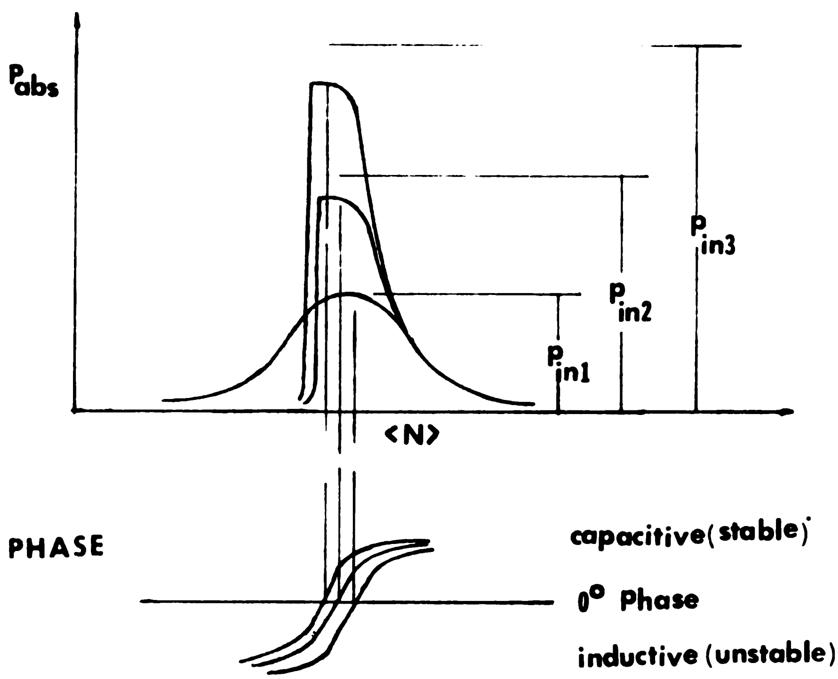

This figure can be thought of as a superposition of oscilloscope traces. As shown by the luminosity curve of Figure 5.1, the density varies only slightly when in a resonance. Thus, there is a slight shift in the resonant frequency as I_{dc} is decreased. Also for low incident power, p_{in1} is approximately equal to the maximum absorbed power, p_{abs}; i.e., critical coupling occurs. However, at higher incident power, p_{abs} is less than p_{in2} and p_{in3} which results from a decrease in the efficiency of coupling microwave power into the plasma system.

Physically, the coupling property of the ridge waveguide system can be directly related to the reflection coefficient, Γ, of its equivalent transmission system. The condition for critical coupling (i.e., $p_{abs} = p_{in}$) is the vanishing of $|\Gamma|$. Thus, the coupling problem can be approached from the impedance point of view. The effects of the sheath thickness, s, and the incident power, p_{in}, on the coupling of microwave power into the plasma are demonstrated in the impedance curves of constant s and constant p_{in} for the main resonance. A family of impedance curves is sketched below for different, constant sheath thickness ($s_1 > s_2 > s_3$). Also, for constant incident microwave power, the impedance of the plasma system is experimentally measured as the dc current, I_{dc}, in the plasma is varied. A family of impedance curve for different, constant incident power ($p_{in1} < p_{in2} < p_{in3}$) is shown in the diagram below.

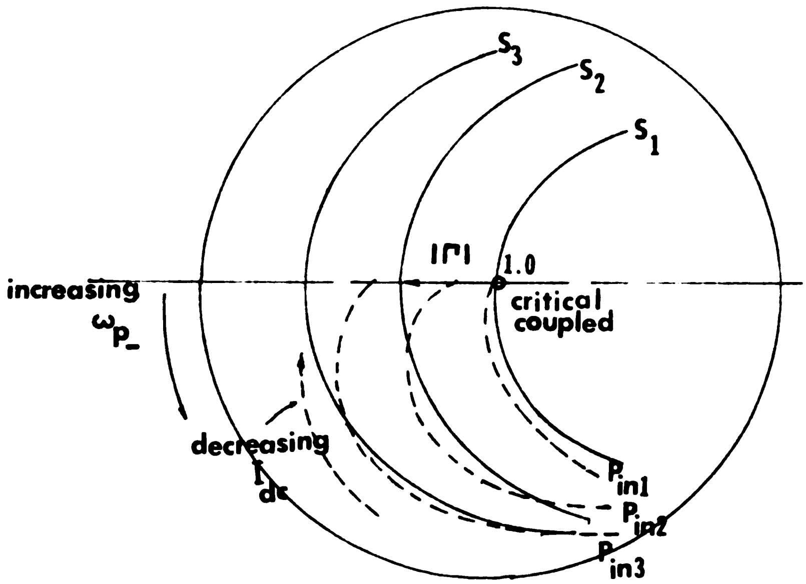

As shown in the sketch above, a criteria for efficient coupling is to reduce the reflection coefficient $|\Gamma|$ which corresponds to the distance between the point of unity and the impedance curve. Note that for the case of critical coupling at low incident power p_{in1}, the impedance curve passes through the real axis at the point of unity which corresponds to a zero reflection coefficient. For higher incident powers p_{in2} and p_{in3}, the decrease in coupling is demonstrated on the Smith Chart as an increase in $|\Gamma|$. Inefficient coupling can also be resulted from a small sheath. It is indicated in the above sketch that increasing s simultaneously decreases $|\Gamma|$. As discussed in Chapter 3, increasing the sheath thickness, s, displaces the resonance position to a lower density. Thus, at resonance, the conductivity of the plasma becomes smaller, or the resistivity becomes larger. As a result, the reflection coefficient, $|\Gamma|$, decreases with an increase in s. This decrease in $|\Gamma|$ increases the efficiency of coupling microwave power into the plasma.

If one follows a curve of constant p_{in}, it is noted that as I_{dc} is decreased, more rf power is absorbed, and thus the sheath is constantly changed. It changes from a small sheath to a large sheath as I_{dc} is decreased. This change in sheath explains the distortion of the experimental resonance curves at high microwave power (see Figure 5.1). This alteration in s (or alteration of the density profile in a more accurate model) has also been proposed by others to explain the change in resonances at moderate incident microwave power[2]. In summary, the coupling of microwave power into the plasma can be improved by either adjusting the plasma parameters or the characteristic impedance of the transmission system.

5.2 Parametric amplification in a resonantly sustained high frequency plasma

In the following, the experimental results of a radiation induced parametric instability in a completely microwave sustained plasma are discussed. It is believed that this phenomenon can be interpreted as a nonlinear coupling of the electron plasma modes, ion-acoustic modes and the pump field. The result is a four frequency (f_o, f_i, $f_o \pm f_i$) parametric interaction. By reducing the pump power just below the power threshold required for the instability, a separately applied cw input signal can be amplified if the signal is approximately equal to the sum frequency ($f_o + f_i$) or the difference frequency ($f_o - f_i$). The experimental results indicate that the parametric instability depends not only on the incident power threshold, but also depends on the geometry of the system, the density gradient (or sheath in the plasma capacitor model) and dc bias across the discharge.

The coaxial system discussed in Chapter 4 and shown in Figure 4. 2 was used in this investigation. The discharge was created and resonantly sustained inside the center conductor gap by a frequency stabilized high power microwave source which is the 'pump' for the parametric instability. In all the experiments, the gap spacing is much smaller than the center conductor diameter; thus, the plasma geometry can be approximated by a plasma filled capacitor. The theoretical results of Chapter 3 can be applied here also. As indicated in Chapter 3, high frequency (electron plasma) resonances at, f_1, (center frequency of temperature or cold plasma resonances), and low frequency (ion-acoustic) resonances at, f_i, exist in such a model. As a result of plasma nonlinearities, harmonic resonances also exist. This resonantly sustained high frequency plasma capacitor has demonstrated a resonance nature at both the fundamental (3. 03 GHz) and harmonic frequencies. These resonances are the nonlinear high power temperature and cold plasma resonances of the capacitor. They are similar to the high poer resonances in the plasma column which was just studied in the previous section.

Experimentally, a parametric instability was observed when the pump frequency, f_o, approximately equal to f_1, was 3.03 GHz and f_i varies from several hundred KHz to 4 MHz. The relative positions of the high and low frequency resonances with respect to the pump frequency are sketched below.

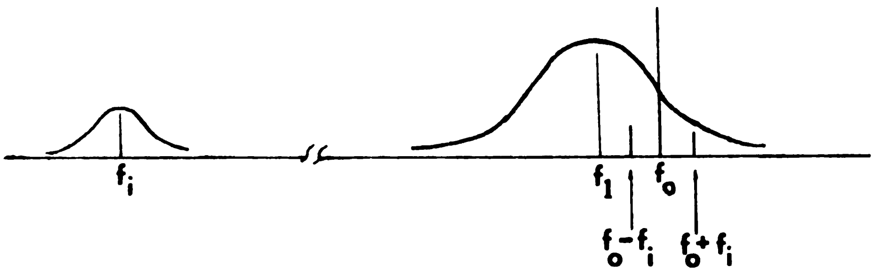

The experimental plasma ($f_1 >> f_i$) is completely resonantly sustained and hence in accordinance with the discussion of the previous section, is operating in a stable region on the resonance curve. Such a position is indicated in the figure. From the theory of Chapter 3, one can observe that when the plasma is in resonance, the E field strengths are very large (many times larger than that of an empty capacitor). These large E fields cause nonlinear phenomena to occur. In particular, the high frequency resonance couples nonlinearly to the low frequency resonance f_i. Since the system is also resonant at $f_o \pm f_i$, a four frequency parametric interaction results.

As noted in Chapter 3, the plasma geometry has a number of resonances, and the instability can occur in many similar resonant states. However, the power required for the instability is quite different for each resonance. For example, the incident power threshold can vary from approximately 12 watts up to 25 watts (5 watts - 15 watts absorbed power) depending on the resonance and collisional damping of the plasma. Here, the discussion is restricted to the behavior of the instability while the capacitor remains in a single resonance state.

When the incident power is above a certain threshold, and the pressure is reduced to a value where collisional damping can be neglected (approximately 400 microns in dry air) coherent sidebands at $f_o \pm f_i$ always appear in the reflected power. A typical reflected spectrum and an oscilloscope trace of a reflected spectrum are shown in Figures 5.6 and 5.4 respectively. Just above the instability power threshold, only $f_o \pm f_i$ components are present. However, as the input power is slightly increased, other discrete frequency components, $f_o \pm 2f_i$, $f_o \pm 3f_i$, etc., gradually appear. If the incident power is increased continuously, the side frequency components shift in position and then disappear. The shifts in frequency will be discussed in the next section.

At the very onset of the sidebands, low frequency oscillations were detected with a low frequency probe. As shown in Figure 4.3, a coaxial probe, which was connected to a low frequency spectrum analyzer, was inserted into the plasma through the hollow inner conductor. This probe detected the existence of strong low

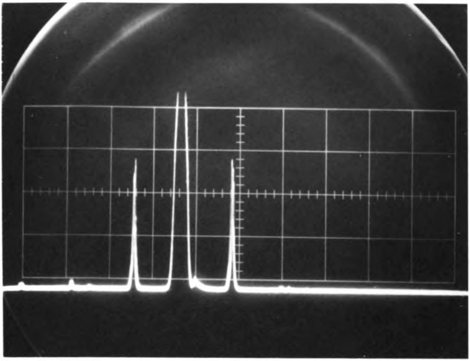

Figure 5.4 Reflected power spectrum at fundamental frequency (3.03 GHz) (dispersion = 1 MHz/cm, pressure $\simeq$ 400 micron)

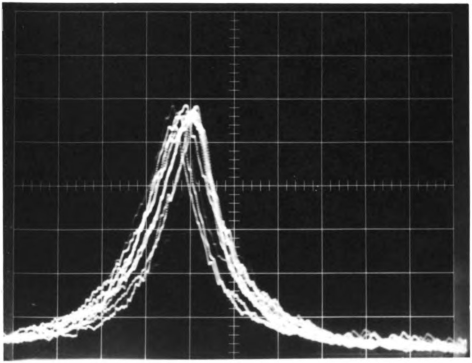

Figure 5.5 Low frequency oscillations detected by low frequency probe (f_i = 2.4MHz, pressure $\simeq$ 400 micron)

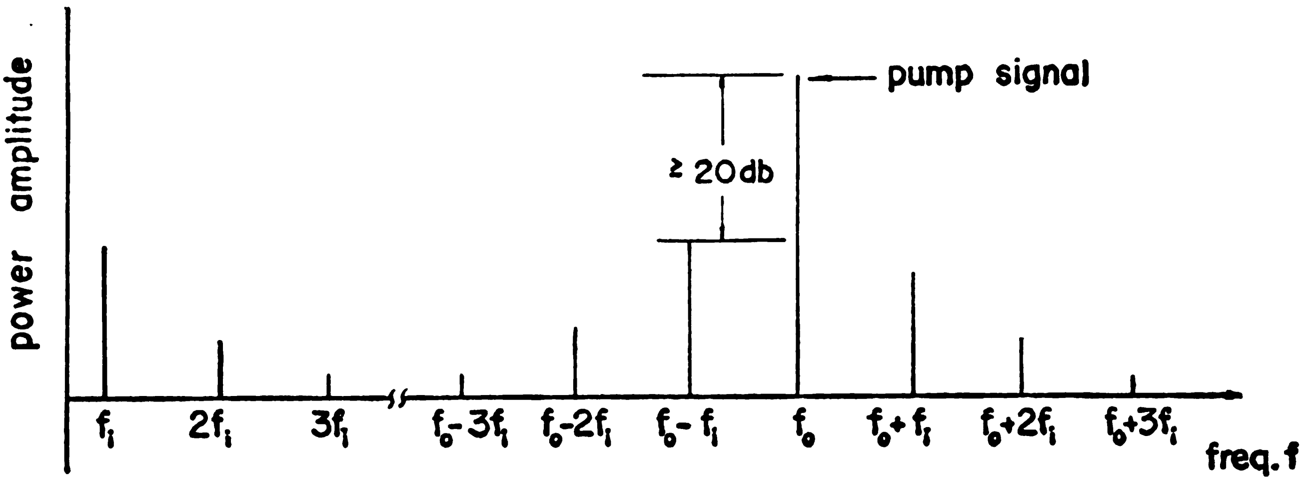

Figure 5.6 Diagram of the reflected power spectrum

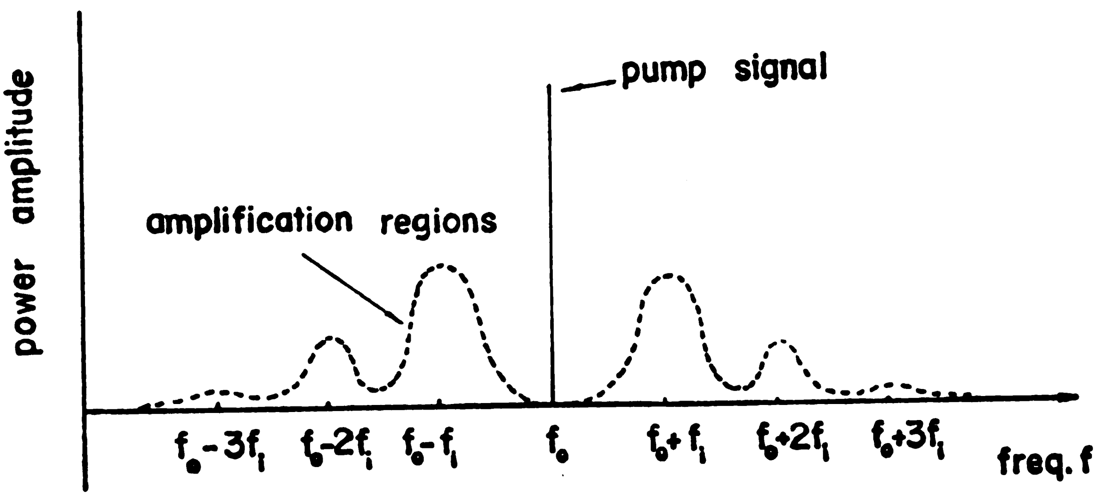

Figure 5.7 Diagram of parametric amplification region.

frequency oscillations at f_i and $2f_i$ whenever the high frequency sidebands appear in the reflected power spectrum. Thus, the existence of a low frequency oscillations in the plasma was experimentally proved. Figure 5.5 shows a picture of such a low frequency oscillation.

In the experiment, a dc biased voltage was externally applied across the conductor gap through the quarter-wave stub as shown in Figure 4.3. The variation of the dc bias, and hence the plasma sheath, was seen to have an influence on the instability power threshold. In fact, by holding the incident power and the pressure constant, the parametric instability could be excited by slowly increasing the dc bias. However, too large a dc bias caused the side frequency components to shift in position, and then totally disappear. Physically, the disappearance of the sidebands is caused by shifting the sheath voltage. Such a shift causes the plasma to be in or out of a resonance (i.e., ion-acoustic resonance for the plasma capacitor model).

If the incident pump power was reduced to a level just below that required for the instability (i.e., to a value where there are no sidebands present), the plasma capacitor was able to amplify a separately applied input signal. With the pump power adjusted to a value slightly below the threshold, a separate, variable frequency signal of approximately .06 mw was incident on the plasma capacitor. This signal was introduced into the coaxial system through the directional coupler as shown in Figure 4.2. The reflected power was sensed through another directional coupler with a spectrum analyzer. As the signal frequency, f_s, was varied manually, the magnitude of the reflected power was observed to vary significantly from frequency to frequency. For frequencies where $f_s > f_o + 3f_i$ and $f_s < f_o - 3f_i$, the reflected power at f_s was approximately equal to the input power indicating complete reflection from the plasma capacitor. However, when the signal was in the vicinity of $f_o \pm f_i$ and $f_o \pm 2f_i$, a large increase in reflected power was observed indicating that amplification was occurring. The region of parametric amplification is shown in Figure 5.7.

In particular, the frequency f_s was amplified by 13-24 db (depending on the pressure and resonance) when it was in the vicinity of $f_o - f_i$. The gain at $f_o + f_i$ is only a few db less. When the signal of $f_s \simeq f_o - f_i$ (or $f_o + f_i$) was being amplified, a signal at $f_s \simeq f_o + f_i$ (or $f_o - f_i$) also appeared indicating the presence of a four frequency cw parametric interaction. A similar four frequency effect was observed when the input signal was in the vicinity of $f_o \pm 2f_i$, but the gain of the interaction was less than 8 db. A picture of the amplified signal is shown in Figure 5.8. This picture was taken when the signal frequency, f_s, was slowly swept through the amplification region in the vicinity of $f_o \pm f_i$. Note that the signal is too small to be observed outside the amplification region (the short, bright lines near the base line are caused by the spectrum analyzer).

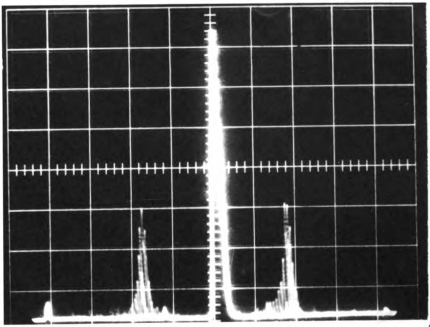

frequency

Figure 5.8 Parametric amplification of a separately applied microwave signal ($p_{in} \simeq 35$ watts, pressure $\simeq 400$ microns, dispersion= 2 MHz/cm, L = 1.25 mm).

(a)

(b)

(c)

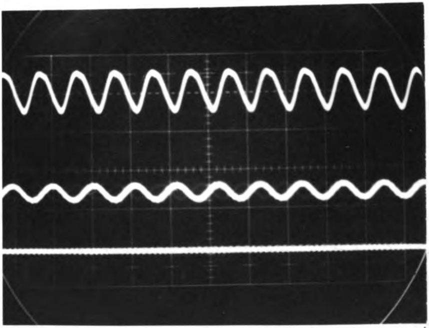

time

Figure 5.9 Low frequency oscillations detected by sensing rectified voltage across the inner conductor gap ($p_{in} \simeq 35$ watts, pressure $\simeq 400$ micron, sweep time = .5 μsec/cm, L = 1.25 mm).

Another way of detecting the low frequency oscillations was to sense the voltage across the quarter-wave stub with an oscilloscope (see Figure 4.2). The oscillations were displayed on the oscilloscope with a time sweep. A typical oscilloscope trace of the low frequency oscillation is shown in Figure 5.9(a). In this figure, the system is in self-oscillation; i.e., sidebands appear in the reflected power spectrum. The frequency f_i is shown to be approximately equal to 2 MHz. As a result of low frequency harmonics at $2f_i$, etc., the wave form is distorted from being a pure sine wave. If one reduces the microwave pump input to just below the instability threshold, Figure 5.9(c) shows that the low frequency oscillations disappear (the small ripple is caused by noise). Now, if a small microwave signal of f_s is applied to the system, low frequency amplification, as mentioned above, occurs and the entire system breaks into oscillation. These amplified low frequency oscillations are shown in Figure 5.9(b).

In summary, the experimental results indicate that the instability observed is a four frequency parametric amplification since amplification exists above and below the pump frequency. During this investigation, a similar parametric amplification was reported by others[51, 52]. The power threshold for parametric interaction is found to be of the same order of magnitude as that of Stern and Tzoar[40]. Thus, the theory of DuBois and Goldman[37, 41] does not account for the experimental results here. Also it is believed that the low frequency oscillations observed in the parametric amplification and in the related phenomena to be discussed in the next section correspond to the ion-acoustic oscillations. The high frequency oscillations correspond to the electron temperature and cold plasma resonances. Further development of the plasma capacitor model including nonlinear effects might help to explain the experimental results presented here.

5.3 Frequency shifts of the low frequency f_i

It was noted in the last section that when the resonantly sustained plasma was in a parametric resonance, the low frequency, f_i, varied as the incident power varied; as the plasma size changed; or as a small, separately applied dc voltage was increased or decreased. In an attempt to better understand the parametric instability, this change of f_i was studied. It was found that if the low frequency oscillation is assumed to correspond to an ion-acoustic resonance, then the plasma sheath has an important influence on f_i.

Experimentally, the plasma size is changed by varying the conductor gap spacing, L. As the gap spacing, L, is varied, the light-intensity measurements indicate that the average plasma density remains constant. Thus, the system remains in the same resonance[4]. The frequency f_i is measured by observing the shift of the side frequency component in the reflected power spectrum. Figure 5.10 shows the variation of f_i versus L for a constant incident

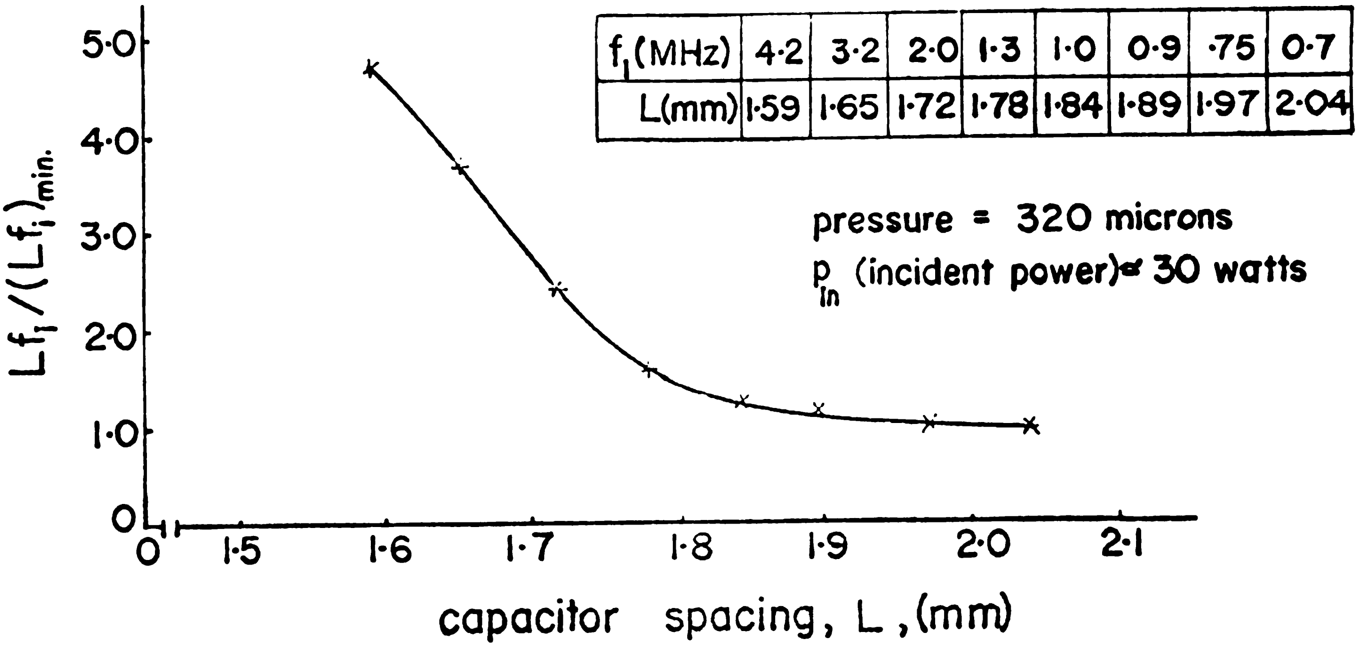

f_1(MHz)	4·2	3·2	2·0	1·3	1·0	0·9	·75	0·7
L(mm)	1·59	1·65	1·72	1·78	1·84	1·89	1·97	2·04

Figure 5.10 Shift of low frequency, f_i, vs. capacitor spacing, L. ($p_{in} \simeq 30$ watts, pressure = 32.0 microns)

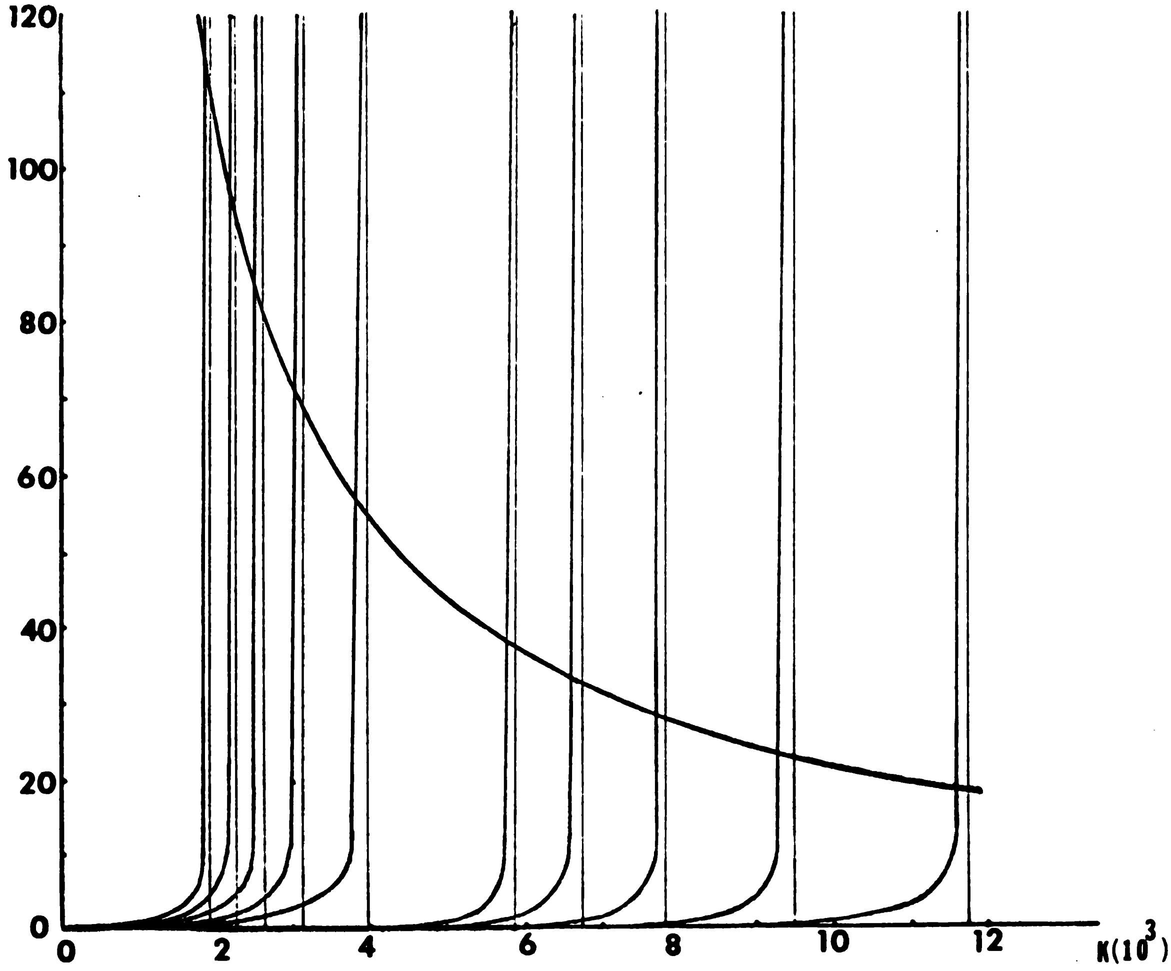

Figure 5.11 **Graphical solution of low frequency capacitor impedance for different capacitor spacing, L.** ($\omega_{p-} = 6\pi \times 10^9$, $s = .6$ mm, $U_e = 7 \times 10$, $L_1 = 1.4$ mm, $L_2 = 1.6$ mm,

power. Clearly, the frequency f_i is not related to the gap spacing, L, in a simple manner.

In previous experiments with a mercury-vapor discharge, the frequency f_i was identified as a standing ion-acoustic wave with a wavelength given by the inside diameter of the tube[40]. It is believed that standing ion-acoustic waves also exist in the present experiment (a "perturbed plasma" as described elsewhere[47] is assumed here). As discussed earlier in Chapter 3, the wavelength λ_i and frequency f_i of the ion-acoustic wave are related by

$$f_i \lambda_i = \left(\frac{\gamma K T_e}{m_i} \right)^{1/2} \tag{5.1}$$

when $2\pi f_i << \omega_{p+}$; $T_e >> T_i$. These approximations hold for the high frequency discharge discussed here.

In general the electron temperature, T_e, can be assumed to be approximately constant in this investigation. Thus, the frequency of the standing ion-acoustic wave is necessarily non-dispersive; that is, $f_i \lambda_i$ = constant. If one assumes that the standing acoustic wave occupies the complete length L between the plates, then, as the distance between the plate is varied, the frequency f_i should change in accordance with the equation above; i.e., Lf_i = constant. However, as shown in Figure 5.10, the normalized (with respect to the minimum Lf_i product) Lf_i product is far from constant. The curve indicates that as L decreased, the standing acoustic wave occupied a decreasing percentage of the total L. That is, the region of allowed ion-acoustic propagation decreased faster than L. Thus, it appears that the sheath appears to play an important role in reflecting the ion-acoustic wave.

A more accurate interpretation of the behavior of f_i vs. L requires a theoretical analysis of the plasma capacitor model discussed in Chapter 3. Since the average plasma density and the electron temperature remain essentially constant when L is varied, the Debye length, and hence the sheath thickness s, can be approximated by a constant. The low-frequency, capacitor impedance given by equation (3.65) is solved graphically for the following plasma parameters: $s = .6$ mm, $\omega_{p-} = 6\pi \times 10^9$, $T_e = 3 \times 10^5 K^o$. The graphical solution corresponding to the lowest ion-acoustic mode frequency is shown in Figure 5.11 for different values of L (1.4 mm $\leq$ L $\leq$ 2.2 mm). Note that s is fixed in these calculations. As L is increased, the sheath region makes up a greater amount of the capacitor spacing for small L than for large L. As shown in Figure 5.12, the theoretical curve is generally consistent with the experimental curve of Figure 5.10. Better agreement could be achieved with a choice of T_e or s which are closer to the experimental condition.

When the incident power is increased, the effect of the sheath again exhibits itself as a decrease in f_i. A typical change in f_i vs. incident power for a constant L is shown in Figure 5.13. As the incident power is increased, the plasma attempted to remain in the

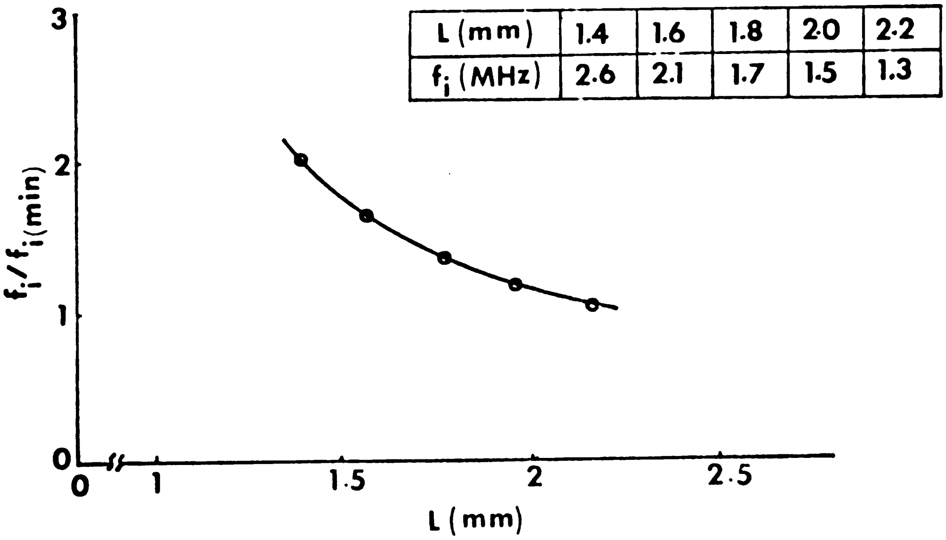

L (mm)	1.4	1.6	1.8	2.0	2.2
f_i (MHz)	2.6	2.1	1.7	1.5	1.3

Figure 5.12 Shift of low frequency, f_i, vs capacitor spacing, L. (theorectical) ($\omega_{p-} = 6\pi x10^9$, $5 \simeq .6$ mm, $U_e = 7x10^5$)

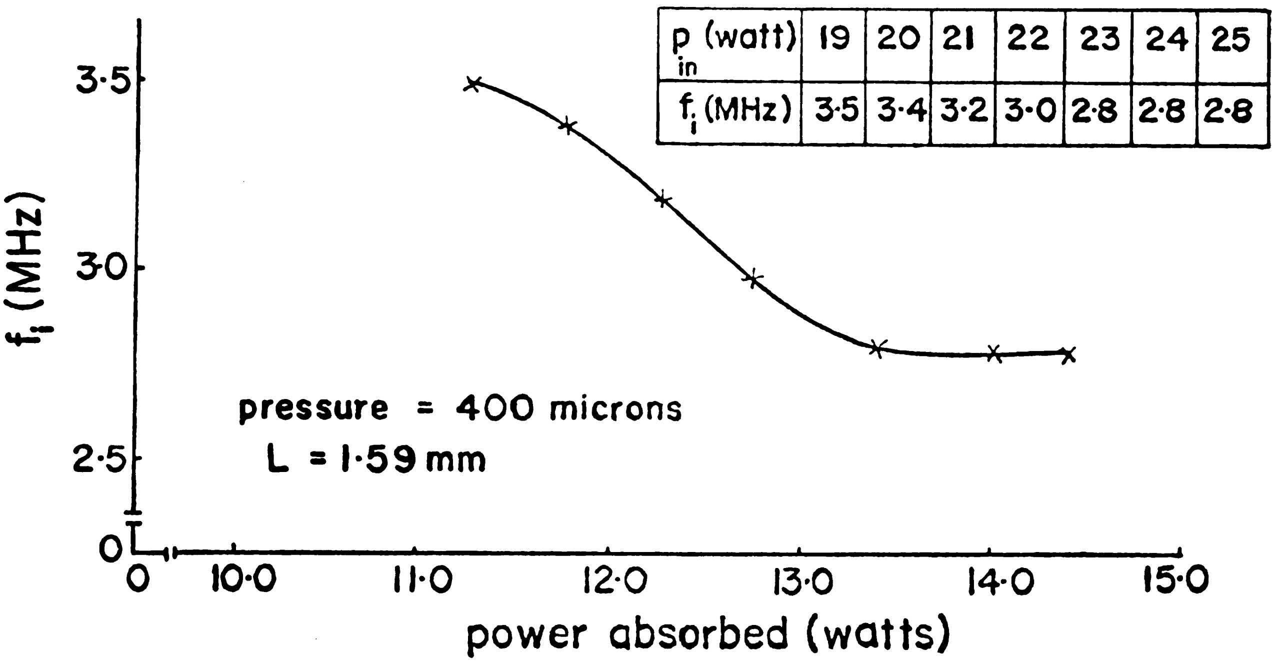

p_{in} (watt)	19	20	21	22	23	24	25
f_i (MHz)	3·5	3·4	3·2	3·0	2·8	2·8	2·8

Figure 5.13 Shift of low frequency, f_i, vs. the absorbed power (L , 1.59 mm, Pressure = 400 micron)

resonance state by modifying the zero-order density profile[2]. This modification decreased the sheath and allowed the standing ion-acoustic wave to occupy a larger space between the capacitor plates. The experimental results could be compared with that of the plasma capacitor model if the variation of s with p_{in} was available.

The frequency shift of the standing ion-acoustic wave was also observed when a dc biased voltage was applied across the capacitor plates. As the dc bias is increased, the low frequency f_i increases. The increased dc voltage increases the size of the sheath resulting a smaller plasma slab. Thus the frequency of resonance, f_i, increases in accordance with the plasma capacitor model of Chapter 3. Figure 5.14 shows the variation of the frequency f_i as a function of the dc voltage V_{dc}. Note that the curve of f_i vs. V_{dc} is asymmetrical. This lack of symmetry is caused by the asymmetrical density profile of the plasma which induces a dc voltage to appear across the center conductor gap. The profile is asymmetrical, because one probe is held at ground and the other floats.

In conclusion the frequency f_i usually can not be directly related to the external dimension L. However, if one assumes that $\lambda_i = 2L$ when the plasma is operating in the horizontal region of the curve in Figure 5.13, then the value of T_e obtained from the equation (5.1) is close to experimentally measured values. For example, $T_e = 3.7 \times 10^4$ K^o in Figure 5.10. This agreement between the

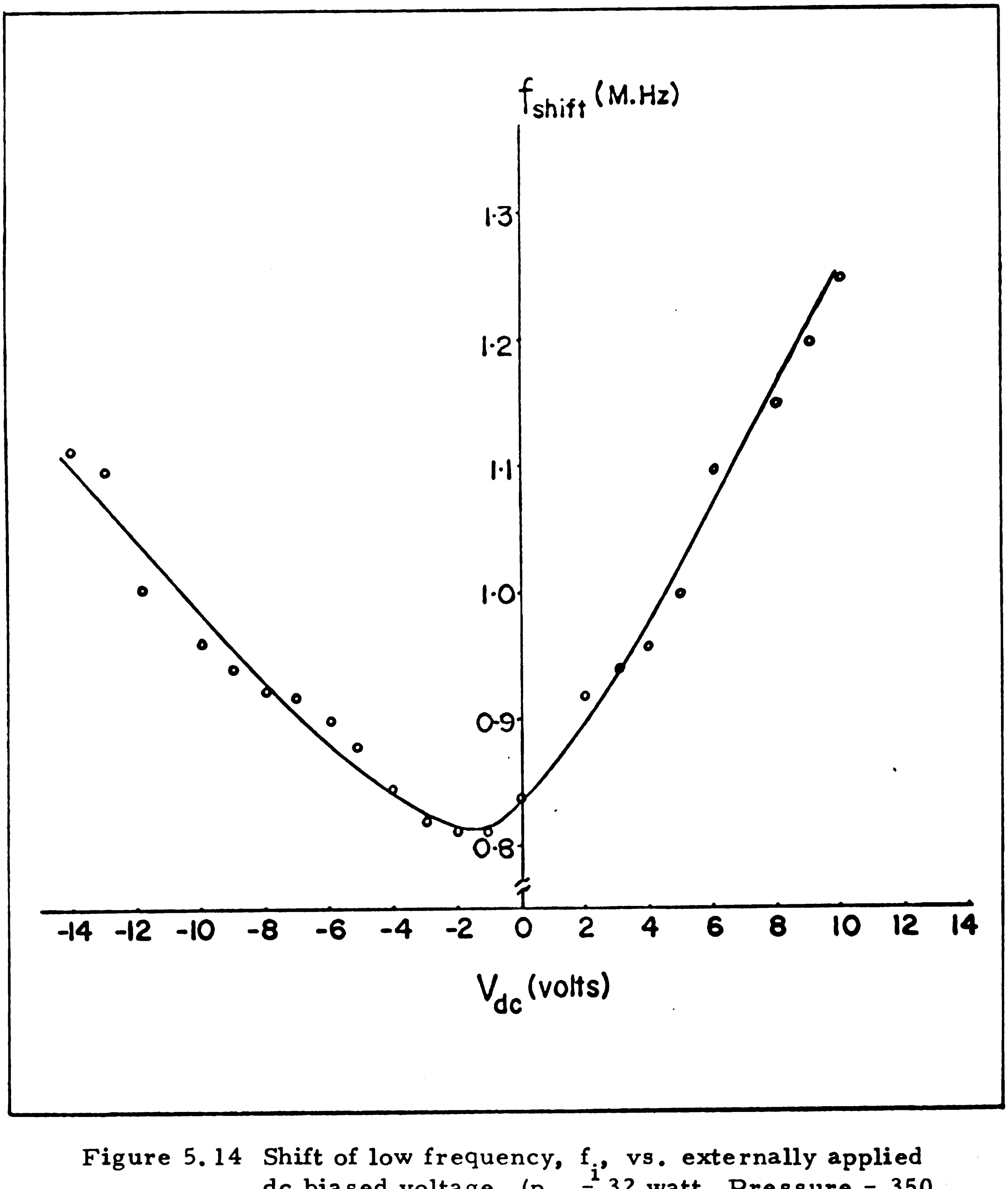

Figure 5.14 Shift of low frequency, f_i, vs. externally applied dc biased voltage. (p_{in} = 32 watt, Pressure = 350 micron, L = 1.5 mm)

"sheathed" plasma capacitor model and experimental results supports the conclusion that the low frequency resonances are caused by standing ion-acoustic waves.

5.4 Frequency modulation of the third harmonic output

Here a study of the coupling between a high frequency resonance and a low frequency resonance is discussed. The experimental plasma is again the resonantly sustained coaxial plasma capacitor discussed in the previous two sections and is shown in Figure 4.2. This capacitor can be resonant simultaneously at the incident frequency f_1, third harmonic frequency $3f_1$ and the low frequency f_i. In particular, emphasis is placed on the nonlinear coupling between the low frequency oscillation discussed in Section 3.3 and the third harmonic resonance. Investigating the coupling between f_i and $3f_i$ has an experimental advantage over studying the coupling between f_i and f_1 (as has been done by others[40, 53]) since there is no external driving electromagnetic radiation present to mask the observation of $3f_i$.

The resonantly sustained high-frequency plasma is formed in the center conductor gap ($L \gtrsim 1.6$ mm) of the coaxial system. The gas is dry air. The third harmonic ($\simeq 9.09$ GHz) is created within the plasma, and is coupled through an x-band waveguide system into a high frequency spectrum analyzer as shown in Figure 4.2.

It is found experimentally that when the plasma capacitor is simultaneously resonant at f_i, f_1 and $3f_1$, the driving fundamental power at f_1 is coupled to f_i and $3f_1$. At high pressure, only a single output third harmonic frequency is observed. However, as the pressure in the system is gradually reduced, the third harmonic output drops suddenly to a low value ($\lesssim$ 2 mw) and is modulated as shown in Figure 5.15. In this low pressure regime, the electron-neutral collisional frequency is much smaller than the applied driving frequency. At the onset of the modulated harmonic output, low frequency oscillations at f_i and $2f_i$ can be detected with the low frequency probe. The sidebands that appears in Figure 5.15 are related to the ion-acoustic oscillations; that is, they occur at $3f_1 \pm f_i$, $3f_1 \pm 2f_i$, $3f_1 \pm 3f_i$, etc.

The sidebands are essentially equal in amplitude when they first appear. As the pressure in the system is further reduced, the sidebands may become very unequal in amplitude, while the carrier at $3f_1$ may be strongly suppressed. In addition, the amplitude of the upper or lower sidebands may interchange. Such changes can be also achieved by variations of the incident power level or gap spacing.

The frequency modulation of the third harmonic output can be qualitatively interpreted on the basis of low-frequency perturbation of the non-uniofrm zeroth-order density profile. When the plasma capacitor is resonant at the fundamental frequency f_1 and the low frequency f_i, the fundamental energy is coupled by a poorly understood process[41, 53] to the low frequency oscillation. These low frequency oscillations are superimposed on the zeroth-order density

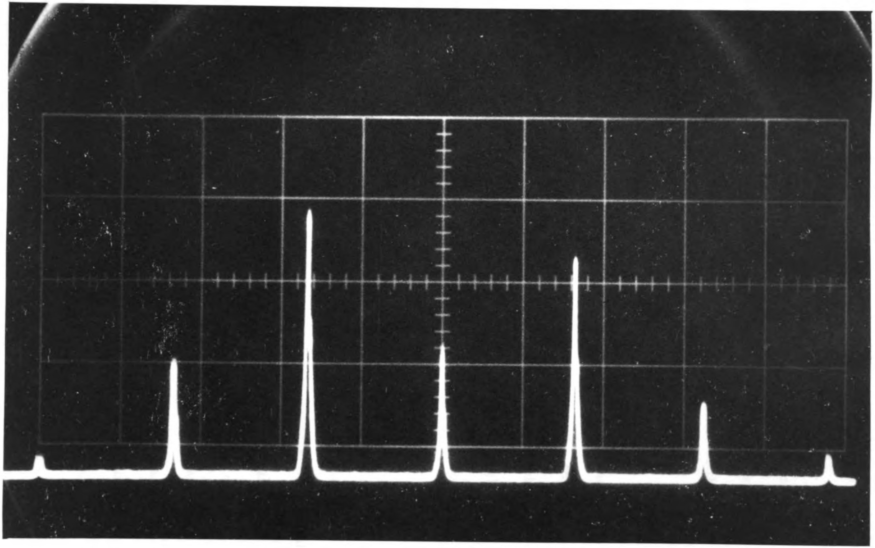

Figure 5.15 Reflected power spectrum of the frequency modulated third harmonic output (f_1 = 3.03 GHz, $3f_1$ = 9.09 GHz, f_1 = 1.65 NHz, dispersion = 1MHz/cm L = 1.6 mm, Pressure = 250 micron)

profile resulting in a time varying density profile. That is, the low frequency density profile becomes $n = n_o(x) + n_{o1} \cos\omega_i t + \ldots$ (x is the position between the capacitor plates). Also the capacitor is resonant at $3f_1$ causing an easily detectable amount of power at $3f_1$ to be present[33]. However, the temperature resonance of the third harmonic varies at ω_i, and the third-harmonic spectrum is modulated as shown in Figure 5.12.

The above physical description can be formulated theoretically by writing the equations which describe the behavior of a third harmonic signal while in a temperature resonance. By assuming the above mentioned time varying profile and neglecting the high frequency motion of the ions, the electron density has the following form.

$$n_e(x,t) = n_{eo}(x) + n_{e1}(\omega_1 t) + n_{01}(\omega_i t) + n_{02}(2\omega_i t) \qquad (5.2)$$

where the unperturbed and perturbed quantities are designated by the subscripts (0 and 1) respectively. It is assumed that the spatial average plasma density $< n_{eo} >$ is much greater than the high frequency perturbation, n_{e1}, and the low frequency perturbations, n_{01} and n_{02}; i.e., $< n_{eo} > \gg n_{e1}$; $< n_{eo} > \gg n_{01}\ n_{02}$. By experimental observation of the low frequency oscillation, n_{02} was noted to be less than $n_{01}/2$. Note that instead of assuming a uniform plasma slab and vacuum sheath as in the previous discussion, this model includes a spatially varying density profile, i.e., $n_{eo}(x)$, $\omega_{p-}(x)$.

From the first two hydrodynamic equations for the electron fluid and the Poisson's equation,

$$\frac{dn_e}{dt} + \nabla \cdot n_e \vec{v}_e = 0 \qquad (5.3)$$

$$\frac{\partial \vec{v}_e}{\partial t} + (\vec{v}_e \cdot \nabla)\vec{v}_e + \frac{e}{m_e}\vec{E} + \frac{1}{n_e m_e}\nabla p = \nu_e \vec{v}_e \qquad (5.4)$$

$$\nabla \cdot \vec{E} = \frac{\rho}{\epsilon_o}$$

By assuming that n_{01} and n_{02} are independent of x and $\nabla = \frac{\partial}{\partial x}$, the following equation for the third harmonic electric field in the one-dimensional plasma can be derived from equations (5.2) to (5.5)[2].

$$\left[\frac{\partial^2}{\partial t^2} + \nu_e \frac{\partial}{\partial t} + \frac{e^2}{m_e \epsilon_o}(n_{01} + n_{02}) + \omega_o^2\right] E_1 = \left(\frac{\partial^2}{\partial t^2} + \nu_e \frac{\partial}{\partial t}\right) E_{ext} + \text{(nonlinear terms)} \qquad (5.6)$$

where ν_e = phenomenological collisional frequency

ω_o^2 = third harmonic eigenfrequency for the TDR[54]

$$= \omega_{p-}^2(x) - U_e^2 \frac{\partial^2}{\partial x^2} + U_e^2 \frac{\partial}{\partial x}(\ell n\, n_{eo})\frac{\partial}{\partial x}$$

The external electric field, E_{ext}, is related to the total current J and the perturbed electric field, E_1, through equations (5.3) and (5.5)

$$\frac{\partial E_1}{\partial t} + \frac{J}{\epsilon_o} = \frac{\partial E_{ext}}{\partial t}$$

Since no external microwave source at third harmonic frequency is applied, E_{ext} can be set to zero. If one assumes that $\cos 3\omega_1 t$ is the normalized phenomenological forcing term at $3f_1$ due to the nonlinear terms in equation (5.6), and

$$n_{01}(\omega_i t) = N_{01}\cos\omega_i t$$

$$n_{02}(2\omega_i t) = N_{02}\cos 2\omega_i t ,$$

equation (5.6) can be simplified to

$$\left[\frac{\partial^2}{\partial t^2} + \nu_e \frac{\partial}{\partial t} + \frac{N_{01}e^2}{m_e\epsilon_o}(\cos\omega_i t + \theta) + \frac{N_{02}e^2}{m_e\epsilon_o}\cos(2\omega_i t + \alpha) + \omega_o^2\right] E_1 = \cos 3\omega_i t \tag{5.7}$$

where θ and α are the phase angles of the ion oscillations with respect to the forcing term.

Equation (5.7) can be simplified further with the following transformation

$$E_1 = y\, e^{-\nu_e t/2} \tag{5.8}$$

For $\omega_o >> \nu_e/2$, the transformed equation has the form

$$\frac{\partial^2 y}{\partial t^2} + G^2(t)\, y = e^{at}\cos 3\omega_1 t \tag{5.9}$$

where

$$G^2(t) = \omega_o^2\left[1 + \frac{<\omega_{p-}>^2}{\omega_o^2}\frac{N_{01}}{<n_{eo}>}\cos(\omega_i t + \theta) + \frac{<\omega_{p-}>^2}{\omega_o^2}\frac{N_{02}}{<n_{eo}>}\cos(2\omega_i t + \alpha)\right.$$

$$\langle \omega_{p-} \rangle^2 = \frac{\langle n_{eo} \rangle e^2}{m_e \epsilon_o}$$

$$a = \nu_e / 2$$

Equation (5.9) is a linear second order differential equation with time varying coefficients. Experimentally, for cold plasma and temperature resonances, $1/2 \leq \langle \omega_{p-} \rangle^2 / \omega_o^2 \leq 4$, but as assumed earlier $N_{01} / \langle n_{eo} \rangle \ll 1$. Thus,

$$\frac{\langle \omega_{p-}^2 \rangle N_{01}}{\omega_o^2 \langle n_{eo} \rangle} \ll 1 \; ; \quad \frac{\langle \omega_{p-}^2 \rangle N_{02}}{\omega_o^2 \langle n_{eo} \rangle} \ll 1 \; .$$

Under these assumptions, the low frequency perturbation causes only a small variation of the zeroth-order density profile. As a result, the WKBJ approximation[55] can be applied to find the complementary and particular solution of equation (5.9).

(A) Complementary solution

From WKBJ approximation, the complementary solution to the homogeneous differential equation of (5.9) is of the form

$$y_c = G(t)^{-1/2} \left[A_5 \cos \phi(t) + A_6 \sin \phi(t) \right] \tag{5.10}$$

where A_5 and A_6 are arbitrary constant. From the binomial series expansion

$$G(t) \simeq \omega_o \Big[1 + \frac{1}{2} \frac{\langle \omega_{p-} \rangle^2}{\omega_o^2} \frac{N_{01}}{\langle n_{eo} \rangle} \cos(\omega_i t + \theta) + \frac{1}{2} \frac{\langle \omega_{p-} \rangle^2}{\omega_o^2} \frac{N_{02}}{\langle n_{eo} \rangle}$$

$$\cos(2\omega_i t + \alpha) \Big]$$

$$G(t)^{-1/2} \simeq \omega_o^{-1/2}\left[1 - \frac{1}{4}\frac{\langle\omega_{p-}\rangle^2}{\omega_o^2}\frac{N_{01}}{\langle n_{eo}\rangle}\cos(\omega_i t + \theta) - \frac{1}{4}\frac{\langle\omega_{p-}\rangle^2}{\omega_o^2}\frac{N_{02}}{\langle n_{eo}\rangle}\cos(2\omega_i t + \alpha)\right] \quad (5.11)$$

$$\phi(t) = \int G(t)dt$$

$$= \omega_o t + \frac{1}{2\omega_i}\frac{\langle\omega_{p-}\rangle^2}{\omega_o^2}\left[\frac{N_{01}}{\langle n_{eo}\rangle}\cos(\omega_i t + \theta) + \frac{N_{02}}{\langle n_{eo}\rangle}\cos(2\omega_i t + \alpha)\right] \quad (5.12)$$

Substituting equations (5.8), (5.11) and (5.12) into equation (5.10) yields

$$E_c = e^{-at}\omega_o^{-1/2}[1 - m_1\cos(\omega_i t + \theta) - m_2\cos(2\omega_i t + \alpha)] \quad (5.13)$$

$$\cdot\{A_5\cos[\omega_o t + k_1\sin(\omega_i t + \theta) + k_2\sin(2\omega_i t + \alpha)] + A_6\sin[\omega_o t + k_1\sin(\omega_i t + \theta) + k_2\sin(2\omega_i t + \alpha)]\}$$

where

$$m_1 = \frac{1}{4}\frac{\langle\omega_{p-}\rangle^2}{\omega_o^2}\frac{N_{01}}{\langle n_{eo}\rangle}\ ; \quad m_2 = \frac{1}{4}\frac{\langle\omega_{p-}\rangle^2}{\omega_o^2}\frac{N_{01}}{\langle n_{eo}\rangle}$$

$$k_1 = \frac{1}{2\omega_i}\frac{\langle\omega_{p-}\rangle^2}{\omega_o^2}\frac{N_{01}}{\langle n_{eo}\rangle}\ ; \quad k_2 = \frac{1}{2\omega_i}\frac{\langle\omega_{p-}\rangle^2}{\omega_o^2}\frac{N_{02}}{\langle n_{eo}\rangle}$$

Both amplitude and frequency modulation are exhibited in the complementary solution. Since m_1 and m_2 are much less than unity, the amplitude modulation produces only a negligible effect. The process of frequency modulation induces a series of side frequencies

which can be found by expanding the sine and cosine terms of equation (5.13) in a series of Bessel functions of the first kind through the following identities:

$$\cos(k \sin\theta) = J_o(k) + 2J_2(k)\cos 2\theta + 2J_4(k)\cos 4\theta + \dots \quad (5.14)$$

$$\sin(k \sin\theta) = 2J_1(k)\sin\theta + 2J_3(k)\sin 3\theta + \dots \quad (5.15)$$

The amplitude of the side frequency components depend on the product of the Bessel functions of the first kind with arguments k_1 and k_2. In the steady state ($t \to \infty$), the complementary solution vanishes as a result of collisional damping in the plasma.

(B) Particular solution

From WKBJ approximation and the method of variation of parameters the particular solution of the nonhomogenous differential equation (5.9) is of the form

$$y_p = A(t)x_1 + B(t)x_2$$

where

$$x_1 = G(t)^{-1/2}\cos\phi(t)$$

$$x_2 = G(t)^{-1/2}\sin\phi(t)$$

$$A(t) = -\int \frac{x_2 e^{-at}\cos 3\omega_1 t}{x_1\dot{x}_2 - \dot{x}_1 x_2} \quad (5.16)$$

$$B(t) = \int \frac{x_1 e^{-at}\cos 3\omega_1 t}{x_1\dot{x}_2 - \dot{x}_1 x_2}$$

$\phi(t)$ and $G(t)^{-1/2}$ are given by equations (5.11) and (5.12). Since the amplitude modulation factors m_1 and m_2 are much less than unity, the amplitude modulation effects are neglected. As a result,

$$x_1 \simeq \omega_o^{-1/2} \cos \phi(t) \tag{5.17}$$

$$x_2 \simeq \omega_o^{-1/2} \sin \phi(t) \tag{5.18}$$

$$x_1\dot{x}_2 - \dot{x}_1 x_2 \simeq 1 + \frac{2m_1}{\omega_o} \cos(\omega_i t + \theta) + \frac{4m_2}{\omega_o} \cos(2\omega_i t + \alpha)$$

Again noting that m_1, $m_2 << 1$; thus $x_1\dot{x}_2 - \dot{x}_1 x_2 \simeq 1$. Then, A(t) and B(t) can be written as

$$A(t) \simeq -\omega_o^{-1/2} \int^t e^{-at} \cos \phi(t) \cos 3\omega_1 t \, dt \tag{5.19}$$

$$B(t) \simeq \omega_o^{-1/2} \int^t e^{-at} \sin \phi(t) \cos 3\omega_1 t \, dt \tag{5.20}$$

To simplify the calculations, the frequency modulation factor k_1 is restricted to be less than 1.8 (i.e., $k_1 \leq 1.8$). Thus, terms of order $J_4(k_1)$, $J_3(k_2)$, $J_3(k_1)\, J_2(k_2)$ or higher will be neglected since they are small for $k_1 \leq 1.8$. Furthermore, only the particular cases in which the ion oscillations are in phase (i.e., $\theta = \alpha = 0$ or $2n\pi$), and 180^o out of phase (i.e., $\theta = \alpha = \pi$) with the driving term will be discussed.

Experimentally, the sidebands appear only in the relatively low pressure regime where the collisional frequency, ν_e, are small. Here the limiting cases of $\nu_e << \omega_i$ and $\nu_e >> \omega_i$ are discussed. It appears that the collisional frequency plays an important role in the process of frequency modulation.

In finding the particular solution, the quantities A(t), B(t), x_1 and x_2 are calculated from equations (5.17) to (5.19). Through the use of identities given by equations (5.12) to (5.15), these quantities can be expressed in terms of the product of two infinite series of Bessel functions of the first kind and sine or cosine functions. Consequently, the general form of the particular solution involves the product of four infinite series of Bessel functions and the sine or cosine functions. The complexity involved in the calculation of the side frequency components for the particular solution is obvious. In the following, the lengthy calculation is omitted. The side frequency components for the particular solutions in their final forms are given. To ease the writing, it is convenient to denote $J_N(k_1)$ by J_N and $J_N(k_2)$ by J_N^*. Since the system is assumed to be resonant at the third harmonic, ω_o is set equal to $3\omega_1$.

Case (a): $\theta = \alpha = 0$; $\omega_o = 3\omega_1$

For $\nu_e \gg \omega_i$

$$\begin{aligned} E_p \simeq \frac{\sin 3\omega_1 t}{6a\omega_1} \Big[& (J_o^*)^2(J_o^2 + 2J_1^2 + 2J_2^2 + 2J_3^2 + \ldots) \\ & + (J_1^*)^2(2J_o^2 + 4J_1^2 + 2J_2^2 + 4J_3^2 + 4J_1J_3 + \ldots) \\ & + (J_2^*)^2(2J_o^2 + 4J_1^2 + 4J_3^2 + \ldots) \\ & + (J_o^* J_2^*)(4J_2^2 - 8J_1J_3 + \ldots) + \ldots \Big] \end{aligned} \qquad (5.20)$$

For $\nu_e << \omega_i$

$$E_p \simeq \frac{J_o J_o^*}{6 a \omega_1} \Big[(J_o J_o^*) \sin 3\omega_1 t \tag{5.21}$$
$$+ (J_3 J_2 - J_1 J_o^* - J_1 J_1^* - J_3 J_1^* + \ldots) \sin(3\omega_1 - \omega_i)t$$
$$+ (J_1 J_o^* - J_1 J_1^* - J_3 J_1^* - J_3 J_2^* + \ldots) \sin(3\omega_1 + \omega_i)t$$
$$+ (J_2 J_o^* + J_2 J_2^* - J_o J_1^* + \ldots) \sin(3\omega_1 - 2\omega_i)t$$
$$+ (J_2 J_o^* + J_2 J_2^* + J_o J_1^* + \ldots) \sin(3\omega_1 + 2\omega_i)t$$
$$+ J_1 J_1^* + J_1 J_2^* - J_3 J_o^* + \ldots) \sin(3\omega_1 - 3\omega_i)t$$
$$+ (J_1 J_1^* - J_1 J_2^* + J_3 J_o^* + \ldots) \sin(3\omega_1 + 3\omega_i)t + \ldots \Big]$$

The above results are plotted in Figure 5.16(1)-(2) for $N_{02} = .4 N_{01}$, $k_{02} = .4 k_{01}$. In the high pressure regime ($\nu_e >> \omega_i$), the amplitudes of the sidebands are essentially zero possibly doe to collisional damping. However, in the low pressure regime ($\nu_e << \omega_i$), the third harmonic electric field is frequency modulated with sidebands unequal in amplitude.

Case (b) : $\theta = \alpha = \pi$; $\omega_o = 3\omega_1$

For $\nu_e >> \omega_i$

$$E_p \simeq \frac{\sin 3\omega_1 t}{6 a \omega_1} \Big[(J_o^*)^2 (J_o^2 + 2J_1^2 + 2J_2^2 + 2J_3^2 + \ldots)$$
$$+ (J_1^*)^2 (2J_o^2 + 4J_1^2 + 2J_2^2 + 4J_3^2 + 4J_1 J_3 + \ldots)$$
$$+ (J_2^*)^2 (2J_o^2 + 4J_1^2 + 4J_2^2 + 4J_3^2 + \ldots)$$
$$+ (J_o^* J_2^*)(4J_2^2 - 8J_1 J_3 + \ldots) + \ldots \Big]$$

$\nu_- << \omega_i$

$$
\begin{aligned}
E_p \simeq \frac{J_o J_o^*}{6\,a\omega_i} \Big[& (J_o J_o^*)\sin 3\omega_1 t \qquad\qquad (5.23)\\
& + (J_1 J_o^* - J_1 J_1^* - J_3 J_1^* - J_3 J_2^* + \ldots)\sin(3\omega_1 - \omega_i)t \\
& + (J_3 J_2^* - J_1 J_o^* - J_1 J_1^* - J_3 J_1^* + \ldots)\sin(3\omega_1 + \omega_i)t \\
& + (J_2 J_o^* + J_2 J_2^* + J_o J_1^* + \ldots)\sin(3\omega_1 - 2\omega_i)t \\
& + (J_2 J_o^* + J_2 J_2^* - J_o J_1^* + \ldots)\sin(3\omega_1 + 2\omega_i)t \\
& + (J_3 J_o^* - J_1 J_2^* + J_1 J_1^* + \ldots)\sin(3\omega_1 - 3\omega_i)t \\
& + (J_1 J_1^* + J_1 J_2^* - J_3 J_o^* + \ldots)\sin(3\omega_1 + 3\omega_i)t + \ldots \Big]
\end{aligned}
$$

The results for this case are also plotted in Figure 5.16(3)-(4). In comparison with the previous case, the difference in phase causes an interchange in amplitude between the lower frequency sideband and its corresponding upper frequency sideband.

As shown in Figure 5.16, in the low pressure regime, the sidebands are essentially equal in amplitude for small k_1. However, for $k_1 = 1.8$, the sidebands can become very unequal and the center frequency can be strongly suppressed.

The physical process of the modulation phenomenon can be understood from the diagram below.

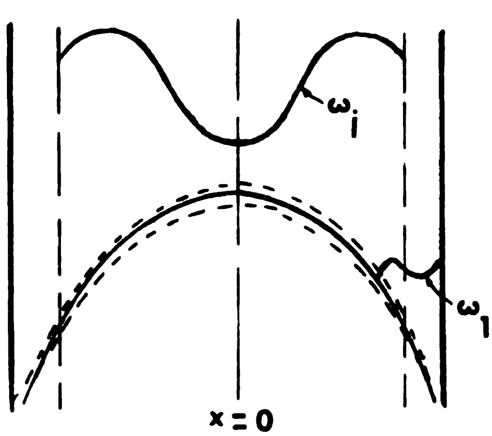

The low frequency ion-acoustic oscillations at ω_i are superimposed on the zeroth-order density profile. This perturbation causes the density profile to vary with time at ω_i and $2\omega_i$. The elctroacoustic resonances at ω_1 as well as at $3\omega_1$ depend on the plasma density profile, and thus any change in the profile causes the resonant frequency at $3\omega_1$ to change. The variation of the density profile results in a frequency modulated third harmonic output. This phenomenon is similar to a perturbation to the inductance or capacitance in a LC resonant circuit.

The theoretical results agree with experimental observations. At high pressure ($\nu_e >> \omega_i$), there is no detected modulation. As the pressure is lowered ($\nu_e \quad \omega_i$), modulation appears, and at still lower pressures ($\nu_e << \omega_i$), the center frequency can be suppressed as shown in Figure 5.16.

These results explain why this modulation does not play an important role in plasma harmonic generations at high harmonic output power[56]. Note that the modulation index, k_1, is inversely proportional to ω_i; that is, as ω_i increase, k, decreases. Thus, when ω_i increases, the number and amplitude of the sidebands decreases. However, for high harmonic power outputs at 9.09 GHz, the length L is approximately 1.0 - 1.2 mm which corresponds to a low frequency oscillation greater than 15 MHz. Thus to observe a modulation, the density variation N_{01} must be 10 times greater than

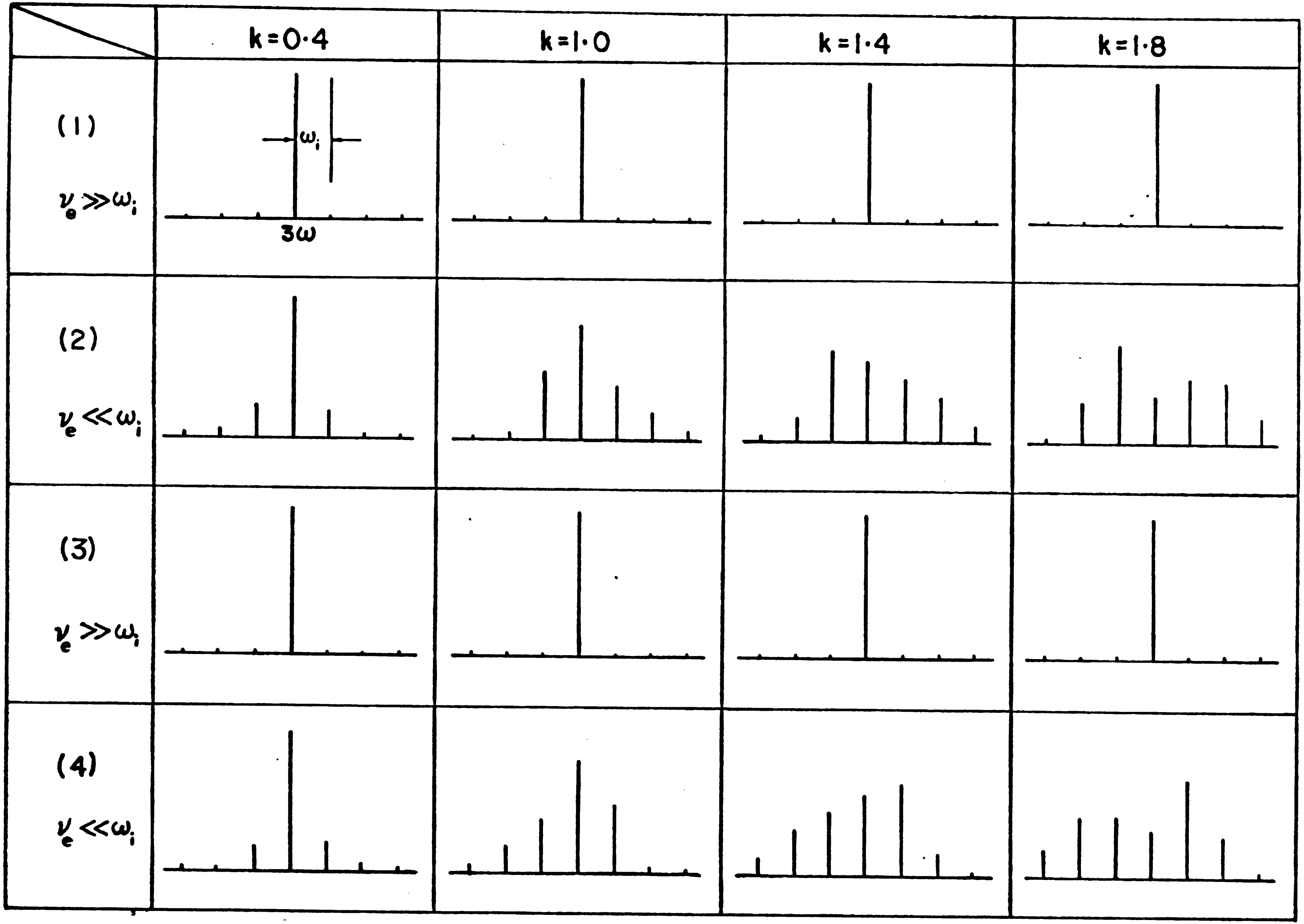

Figure 5.16 Steady-state solution for various k, ω_i and ν_e ($k_2 = .4 k_1$)

that at $L \gtrsim 1.5$ mm ($f_i \lesssim 4$ MHz). Apparently any low frequency variation present are not large enough to produce detectable modulation.

CHAPTER 6

SUMMARY AND CONCLUSIONS

A review of pertinent literature is present in Chapter 2. The history and mathematical formulation of electroacoustic resonances in bounded plasmas is presented. Relevant literature discussing resonantly sustained plasma is also discussed.

In Chapter 3, a model of a typical discharge structure is formulated. This model called a "plasma capacitor" is made up of a uniform, warm plasma region, sheath region and two parallel, infinite metallic plates. Equivalent circuits for the high frequency (GHz) and low frequency (MHz) regions are developed.

At high frequency, this "circuit" predicts a cold plasma and a series of temperature (or electroacoustic resonances). The effects of plasma sheath, collisional damping. etc., on these resonances is studied. At low frequencies, more resonances appear due to the standing ion-acoustic waves. The theoretical data presented here are used in Chapter 5 to interpret some of the experimental results.

Two experimental discharge structures were constructed and put into operation. The description and some of the practical problems associated with the operation of these discharge structures and the associated microwave equipment are discussed in Chapter 4.

A series of experiments were performed. The results and interpretation of these experiments are given in Chapter 5. The transition between the well known linear resonances of a bounded plasma and a completely resonantly sustained plasma was examined experimentally. It was found that the linear resonances become distorted, and stable and unstable rf operating regions appear. By plotting the equivalent impedance vs. ω_p on a Smith Chart, the distortion of resonances is qualitatively explained. In fact, stable and unstable regimes of rf power operation are clearly indicated by the Smith Chart formulation. In particular, it was found that an rf plasma could be maintained in a stable state on only one side of the resonance curve. Also the experimental results and theoretical interpretation indicate that the size of the plasma varies with a variation in absorbed power. That is, the sheath size changes in order to maintain the plasma in a resonant state.

When the plasma is completely resonantly sustained at a frequency f_o, it was observed that for incident power above a certain "threshold" level, oscillations at f_i and $f_o \pm f_i$ ($f_i << f_o$) would appear. When the incident power was adjusted to just below the threshold level, a separately applied signal was able to be amplified. Thus it was experimentally proved that this instability results from a four frequency parametric interaction.

When the instability is observed, the plasma is resonantly sustained in either temperature or cold plasma resonance. The low frequency oscillation at f_i appear to be caused by a standing ion-acoustic wave. That is a correctly "sheathed" plasma capacitor from Chapter 3 is able to predict the proper order of magnitude of this frequency and to explain the frequency shifts associated with the instability. Thus, the physical origin of the instabilities appears to be a mixing of four longitudinal resonances of f_o, f_i, $f_o \pm f_i$. Such four frequency mixing of longitudinal waves in a plasma has been studied theoretically by a number of investigators. However, the lowest predicted power threshold levels from these theories is several orders of magnitude higher than the threshold levels observed in the experiments. This discrepancy between theory and experiment has not yet been resolved.

When the plasma capacitor is resonant simultaneously at f_o, $3f_o$ and f_i the coupling between the low frequency oscillation f_i and the third harmonic resonance is studied. The results of this study indicate that the low frequency resonance causes the zeroth-order density profile to vary at f_i. This variation of the density profile causes the third-harminic output of the capacitor to be frequency modulated.

Future research is needed in a number of areas. A nonlinear capacitor model, which accounts for the coupling between the four resonances of the rf induced unstability should be developed. It may be possible to extend the present linear capacitor model by adding proper nonlinear phenomena. A goal of this study would be to predict the proper incident power threshold for this instability.

Precise impedance measurements of a resonantly sustained plasma should be made. By plotting these measurements on a Smith Chart, one should be able to describe the behavior of the plasma. Also since the sheath (or the density profile in a more accurate model) seems to vary considerably when the plasma is in resonance, an experimental study, which measures this variation of density should be made.

REFERENCES

1. R. W. Wood, Phys. Rev. 35, 673(1930); Phil. Mag. 8, 207 (1929).

2. H. C.S. Hsuan, R. C. Ajmera and K. E. Lonngren, App. Phy. Letter 11. 277 (1967).

3. H. C.S. Hsuan, Phy. Rev. 172, 137(1968).

4. A. M. Messiaen and P. E. Vandenplas, Phys. Letter, 25A, 339(1967).

5. J. Asmussen and Q. H. Lee, Appl. Phys. Letters, 15, 183(1969).

6. G. B. Field, Astrophys. J. 124, 555(1951).

7. J. R. Wait, "Electromagnetics and Plasma," Holt, Rinehart and Winston, Inc. 1968.

8. R. E. Collin, "Field Theory of Guided Waves," McGraw-Hill, 1960.

9. L. Tonks, Phys. Rev. 37, 1458(1931); Phys. Rev., 38, 1219(1931).

10. D. Romell, Nature, 167, 243(1951).

11. A. Dattner, Ericsson Technics, 2, 309(1957).

12. N. Herlofson, Arkiv Fysik, 3, 247(1951).

13. T R. Kaiser and R. L. Closs, Phil. Mag. 43, 1(1952).

14. R. W. Gould, Proc. Linde Conf., Plasma Oscillations. Indianapolis (1959); Bull. Am. Phys. Soc., 5, 322 (1960).

15. D. Bohm and E. P. Gross, Phys. Rev., 75, 1851(1949).

16. P. E. Vandenplas and R. W. Gould, "Study of Electromagnetic Interaction in Plasma," contract U.S. Army Signal Res. Develp. Lab. Quart. Progr. Report No. 3, Calif. Inst. Tech., 1960.

17. J. V. Parker, J. C. Nickel and R. W. Gould, Phys. Fluid, 7, 1489(1964); Phys. Rev. Letters, 11, 183(1963).

18. L. Tonks and I. Langmuir, Phys. Rev. 34, 876(1929).

19. D. A. Hart and N. L. Oleson, J. Appl. Phys., 40, 4541(1969).

20. W. M. Leavens, Radio Science, 69D, 10, (1965) 1321; Phys. Fluid, 10, 2708(1967).

21. D. E. Baldwin, Phys. Fluid, 12, 279(1969).

22. P. E. Vandenplas and R. W. Gould, Proc. Vth Intern. Conf. on Ionization Phenomena in Gases, Munich, 1961, II, 1470, North-Holland, Amsterdam, 1962; Physica, 28, 357(1962).

23. A. M. Messiaen and P. E. Vandenplas, Physica, 30, 303(1964).

24. L. Tonks and I. Langmuir, Phys. Rev., 33, 195(1929).

25. W. O. Schumann, Z. Physik, 7, 121(1942).

26. W. P. Allis, S. C. Brown and E. Everhart, Phys. Rev., 84, 519(1951).

27. E. R. Harrison, J. Electron, Control, 5, 819(1958).

28. A. J. Hatch, Proc. of the Fourth Intern. Conf. on Ionization Phenomena in Gases, Uppsala, 1959(North-Holladn Publ. Amsterdam, 1960), Vol. 1, p. 314.

29. A. J. Hatch, Proc. Vth Int. Conf. on Ionization Phenomena in Gases, Munich, 1961 (North-Holland Publ. Amsterdam, 1962), Vol. I, p. 747.

30. J. Taillet, Am. J. Phys., 37, 423(1969).

31. J. H. Krenz and G. S. Kino, J. Appl. Phys., 36, 2387(1965); Appl. Phys. Letters, 3, 53(1963).

32. J. R. Baird and R. D. Coleman, Proc. IRE, 49, 1890(1961).

33. J. Asmussen and J. B. Beyer, IEEE Trans., ED-16 18(1969); Appl. Phys. Letters, 11, 324(1967); J. Appl. Phys., 39, 2963 (1968).

34. J. Asmussen, Ph.D. Thesis, U. of Wisconsin.

35. O. Demokan, H.C.S. Hsuan and K. E. Lonngren, Phys. Letters, 29A, 99(1969).

36. V. P. Silin, JETP, 21, 1127(1965).

37. D. F. DuBois and M. V. Goldman, Phys. Rev. Letters 14, 544(1965); Phys. Rev., 1964, 207(1967).

38. E. A. Jackson, Phys. Rev., 153, 235(1967).

39. Y. C. Lee and C. H. Su, Phys. Rev. 152 129(1966).

40. R. A. Stern and N. Tzoar, Phys.Rev. Letters, 17, 903(1966).

41. D. F. Dubois and M. V. Goldman, Phys. Rev. Letters, 19, 1103(1967).

42. T. Amano and M. Okamoto, J. Phys. Soc. Japan, 26, 529(1969).

43. R. Goldman, Phys. Fluids, 12, 662(1969).

44. B.S. Tanenbaum, " McGraw-Hill, 1967.

45. P. Diament, V. L. Granaststein and S. P. Schlesinger, J. Appl. Phys. 37, 1771(1966).

46. P. E. Vandenplas, "Electron waves and resonances in bounded plasma, " Wiley-Interscience, Publ., 1968.

47. S. Aksornkitti, H. C. S. Hsuan and K. E. Lonngren, Phys. Fluid, 11, 1838(1963).

48. B. Bertotti, M. Brambilla and A. Sestero, Phys. Fluid, 9, 1428(1966).

49. S. C. Brown, Hanb. der Physik, 22, 1955.
S. C. Brown and A. D. MacDonald, Phys. Rev., 76, 1629(1949).

50. R. F. Harrington, "Time Harmonic Electromagnetic Fields," McGraw-Hill (1961).

51. A. M. Pointu, Y. Pomeau et A. Constantin, Phys. Letters, 26A, 567(1968).

52. P. Leprince, Phys. Letters, 26A, 431(1968); "Les Plasma Haute Frequence Autoresonnants," Rep. LP 91(1969), U. De Paris.

53. M. M. Widner, H. C. S. Hsuan and K. E. Lonngren, Phys. Letters, 26A, 533(1968).

54. P. Weissglas, Phys. Rev. Letters 10, 206(1963).

55. W. J. Cunningham, "Introduction to Nonlinear Analysis," McGraw-Hill (1958) pp. 250-280.

56. J. Asmussen, J. B. Beyer and R. E. McIntosh, Proc. IEEE, 57, 837(1969).